

University of Windsor

Scholarship at UWindor

Electronic Theses and Dissertations

Theses, Dissertations, and Major Papers

2012

Ultrasonic Imaging of Static Objects Through a Scattering Layer Using the Harmonic Phase Conjugation Approach

Raheleh Mirzania
University of Windsor

Follow this and additional works at: <https://scholar.uwindsor.ca/etd>

Recommended Citation

Mirzania, Raheleh, "Ultrasonic Imaging of Static Objects Through a Scattering Layer Using the Harmonic Phase Conjugation Approach" (2012). *Electronic Theses and Dissertations*. 5593.
<https://scholar.uwindsor.ca/etd/5593>

This online database contains the full-text of PhD dissertations and Masters' theses of University of Windsor students from 1954 forward. These documents are made available for personal study and research purposes only, in accordance with the Canadian Copyright Act and the Creative Commons license—CC BY-NC-ND (Attribution, Non-Commercial, No Derivative Works). Under this license, works must always be attributed to the copyright holder (original author), cannot be used for any commercial purposes, and may not be altered. Any other use would require the permission of the copyright holder. Students may inquire about withdrawing their dissertation and/or thesis from this database. For additional inquiries, please contact the repository administrator via email (scholarship@uwindsor.ca) or by telephone at 519-253-3000ext. 3208.

Ultrasonic Imaging of Static Objects Through a Scattering Layer Using the
Harmonic Phase Conjugation Approach

By

Raheleh Mirzania

A Thesis
Submitted to the Faculty of Graduate Studies
Through Physics
In Partial Fulfillment of the Requirements for
The Degree of Master of Science at the
University of Windsor

Windsor, Ontario, Canada

2012

© 2012 Raheleh Mirzania

Ultrasonic Imaging of Static Objects Through a Scattering Layer Using the
Harmonic Phase Conjugation Approach

by

Raheleh Mirzania

APPROVED BY:

Dr. Jerry Sokolowski
Department of Mechanical, Automotive and Materials Engineering

Dr. W.E. Baylis
Department of Physics

Dr. R.G. Maev, Advisor
Department of Physics

Dr. W. Kedzierski, Chair of Defense
Department of Physics

January 26, 2012

DECLARATION OF ORIGINALITY

I hereby certify that I am the sole author of this thesis and that no part of this thesis has been published or submitted for publication.

I certify that, to the best of my knowledge, my thesis does not infringe upon anyone's copyright nor violate any proprietary rights and that any ideas, techniques, quotations, or any other material from the work of other people included in my thesis, published or otherwise, are fully acknowledged in accordance with the standard referencing practices. Furthermore, to the extent that I have included copyrighted material that surpasses the bounds of fair dealing within the meaning of the Canada Copyright Act, I certify that I have obtained a written permission from the copyright owner(s) to include such material(s) in my thesis and have included copies of such copyright clearances to my appendix.

I declare that this is a true copy of my thesis, including any final revisions, as approved by my thesis committee and the Graduate Studies office, and that this thesis has not been submitted for a higher degree to any other University or Institution.

ABSTRACT

The main goal of this study is to develop a new image reconstruction approach for the ultrasonic detection of foreign objects inside the human brain through a simplified skull model. The proposed solution is based on the “Harmonic Phase Conjugation” technique. A source of ultrasound (transducer), small reflecting and scattering objects, a simplified skull layer, and a linear array of ultrasonic receivers are the main components of the test setup. The algorithm starts with the forward propagation step, when the phase and amplitude distributions of the ultrasonic field from the source transducer are recorded with an array of receivers. These distributions are also calculated in presence of a skull layer and small reflecting objects. The recorded phase and amplitude information is then used in the back propagation step, when the phase-conjugated scattered field is numerically propagated through the same medium in the reverse direction. As this field naturally focuses at the locations of the reflecting objects, their image can be reconstructed. After testing the algorithm using a numerical model, a set of laboratory experiments was conducted to verify the accuracy of the developed simulation. The results of these tests are presented, and the main advantages and drawbacks of the approach are discussed.

DEDICATION

To my parents and my husband for their love and endless support

ACKNOWLEDGEMENTS

During my study in University of Windsor, I have had the opportunity to work with some very dedicated and intelligent people, and I thank them for their encouragement, help and enthusiasm in my education.

I would like to express my heartfelt appreciation to my advisor, Dr. Roman Maev, for his encouragement and guidance throughout this research. I am so grateful for his patience and support.

I wish to extend my sincere thanks to Mr. Kiyanoosh Shapoori, for all his guidance and assistance. He, provided direction around various stumbling blocks, and was invaluable to the completion of this work.

I also wish to thank Mr. Eugene Malyarenko, for his time in providing reviews and assistance during the writing of this thesis. I also owe thanks to Dr. William Baylis for his encouragement at the beginning of my study.

Furthermore, I offer my thanks to my defense committee members, Dr. William Baylis, Dr. Wladyslaw Kedzierski and Dr. Jerry Sokolowski, for their time spent reviewing this thesis and their valuable comments and suggestions.

In addition, I would like to thank Mrs. Sarah Beneteau and Mrs. Kimberely Lefebvre for providing assistance during my study.

I would like to thank the U.S. Office of Naval Research and Tessonics Corp for their support of this research through the project #N0001410C0294, "Ultrasonic Imaging of Brain Structures, Blood Vessels, and Foreign Objects through Thick Skull Bones."

Most especially, I wish to thank my mom and dad. All my success has been achieved with their support and encouragement, which means the world to me.

I can't end without expressing my deepest gratitude and love to my dear husband, Mohammad, for his unconditional love and inspiration to me.

TABLE OF CONTENTS

DECLARATION OF ORIGINALITY	iii
ABSTRACT.....	iv
DEDICATION.....	v
ACKNOWLEDGMENTS.....	vi
LIST OF TABLES.....	x
LIST OF FIGURES.....	xi
Chapter1: INTRODUCTION.....	1
1.1. History of phase conjugation.....	1
1.1.1.Optical Phase conjugation.....	2
1.1.2. Acoustic Phase conjugation.....	6
1.1.3.Time Reversal Mirror (TRM).....	10
1.2. Transcranial imaging.....	20
1.3. Acoustical properties of human skull bone.....	22
1.4. Conclusion.....	24
Chapter2: THEORETICAL REVIEW.....	25
Introduction.....	25
2.1. Acoustic Waves.....	25
2.2. Wave propagation in linear viscous media.....	26
2.2.1. Huygens' Principle.....	27
2.2.2. Diffraction.....	27
2.2.3. The Rayleigh-Sommerfeld equation of diffraction.....	29
2.3. Boundary conditions.....	32
2.3.1. Acoustic Impedance.....	32

2.3.2. Reflection and transmission coefficients.....	33
2.3.2.1. Reflection on liquid-solid interface.....	34
2.3.3. Snell’s Law.....	36
2.4. Attenuation in an acoustical field.....	37
Chapter3: SIMULATION.....	39
3.1. Description of the numerical experiment.....	39
3.2. Forward propagation step: calculating phase and amplitude distributions.....	43
3.2.1. Case (a): Unobstructed acoustic field from various sources.....	43
3.2.2. Case (b): Acoustic field in presence of scattering objects.....	47
3.2.3. Case(c): Acoustic field in presence of scattering objects and a scattering layer.....	49
3.3. Back-propagation step: image reconstruction via Harmonic Phase Conjugation method.....	51
3.3.1: Case (a) in back propagation mode.....	53
3.3.2: Case (b) in back propagation mode.....	57
3.3.3: Case (c) in back propagation mode.....	65
3.4. Conclusion.....	67
Chapter 4: EXPERIMENT.....	68
4.1 Scattering layer phantom development.....	68
4.2 Experimental arrangement.....	70
4.3 Results and discussion.....	74
Chapter 5: CONCLUSION AND POSSIBLE FUTURE WORK.....	83
Appendix A.....	86
References.....	93
Vita Auctoris.....	99

LIST OF TABLES

Table.3. 1. The acoustic properties of the scattering layer and water-----	42
Table.3. 2. The dimensions of the main components of the simulated system-----	43
Table.4. 1. The acoustical properties of the prepared skull phantoms-----	69
Table.4. 2. Experimental distances from the array-----	72

LIST OF FIGURES

Fig.1.1. Schematic view of time-reversal technique that caused by PCM-----	3
Fig.1.2. Comparison of a phase conjugate mirror with a conventional mirror-----	4
Fig.1.3. Experimental setup for phase conjugation by stimulated Brillouin scattering----	5
Fig.1.4. Comparison of the conventional image and phase conjugated image-----	8
Fig.1. 5. Ultrasound imaging method with presenting of heterogeneous medium-----	9
Fig.1. 6. Time reversal cavity-----	12
Fig.1. 7. The iterative time reversal process-----	13
Fig.1. 8. Schematic of the TRM focusing through abberating media-----	14
Fig.1. 9. Translation of the array along the y axis-----	16
Fig.1. 10. B-Scan measured with the TRM-----	16
Fig.1. 11. Lithotripsy application-----	18
Fig.1. 12. Aberration time reversal focusing in presence of the skull-----	19
Fig.1. 13. The application of Time-Reversal Acoustic for drug delivery in the brain----	20
Fig.1. 14. Three different layers of adult human skull-----	23
Fig.2. 1. Frequency ranges corresponding to ultrasound process-----	26
Fig.2. 2. Huygens’s principle-----	27
Fig.2. 3. An illustration of Huygens ‘Principle of diffraction-----	28
Fig.2. 4. Comparison of slit size and beam width-----	29
Fig.2. 5. Method to find the velocity potential-----	31

Fig.2.6. Oblique incident at liquid- solid interface-----	34
Fig.2.7. Refraction of sound at the interface of two different media-----	36
Fig.3.1.Description of the model used in the numerical experiment (in absence of layer)-	40
Fig.3. 2. Schematic scattering layer with random phase shifting technique-----	42
Fig.3.3. Simulated amplitude of received ultrasound field from source-----	46
Fig.3.4. Simulated intensity and phase distribution of the ultrasound field on a 2D receiving array-----	47
Fig.3. 5. Simulated amplitude of received acoustic field of the scatterer on the array-----	48
Fig.3. 6. Transmitting of ultrasound beam through scattering layer with random phase shifting technique-----	49
Fig.3.7. Simulated amplitude of the acoustic field in the presence of scattering object and a scattering layer-----	51
Fig.3. 8. Schematic figure of the back propagation mode with presence of skull layer-----	52
Fig.3. 9. Reconstruction of the phase conjugated field of the source and extended source with using the same saved amplitude (small picture in each part)-----	55
Fig.3. 10. Reconstructed image of the extended source combined 50 point sources in different distances from the array-----	56
Fig.3.11. Reconstructed image of the scatterers with different position-----	60
Fig.3.12. Reconstruction images of three scatterers with regards to different distances of the source form the array-----	61
Fig.3.13.Reconstruction images of three scatterers with the same coordinates as Fig.3.12	62

Fig.3. 14. Reconstruction images of three scatterers which they were located in different positions-----	63
Fig.3.15. Reconstruction images of three scatterers when source was tilted in different positions-----	64
Fig.3.16. Image reconstruction of extended source and scatterers in absence of scattering layer (a) and (b) respectively. (c) and (d) represents the results of image reconstruction of source and scatterers, respectively in presence of the scattering layer-----	66
Fig.4. 1. Bone phantoms with the various densities-----	69
Fig.4. 2. A picture of the skull phantom and its dimensions-----	70
Fig.4. 3. Block-diagram of the experimental setup-----	71
Fig.4. 4. General experimental setup-----	72
Fig.4. 5. Close-up view of the source and the positions of the scatterers and the skull phantom-----	73
Fig.4. 6. Picture of water tank-----	73
Fig.4. 7. Distribution of the incident field on the array of receivers. The plot is normalized by the maximum value of the main peak-----	75
Fig.4. 8. Normalized recorded amplitude of the scatterers in absence of the scattering layer-----	76
Fig.4. 9. Normalized recorded amplitude of the scatterers in Presence of the scattering layer-----	77
Fig.4.10. Schematic drawing of the source, scatteres, the layer, and the scanning plane with all dimensions-----	78

Fig.4. 11. Image reconstruction of the source in absence of the scattering layer-----	79
Fig.4. 12. Image reconstruction of the scatterers in absence of the scattering layer-----	80
Fig.4. 13. Image reconstruction of the scatterers in presence of the scattering layer-----	81

Chapter1: INTRODUCTION

Phase Conjugation (PC) is a general method of reversing the direction of propagation of the wave field while keeping the original spatial distribution of amplitudes and phase [1]. The subject of this work is the application of Phase Conjugation in the area of adaptive ultrasound image reconstruction when imaging through distortive media (e.g. inhomogeneous, scattering, nonlinear, etc.).

1.1. History of phase conjugation

Phase conjugation has been studied both in acoustics [2] and optics [3], but initially, its definition was proposed in optics, and the related research was focused on the non-linear interaction of waves in the medium [4].

Acoustical phase conjugation (APC) can be realized by using transducers capable of reversing the temporal order of the received signal upon retransmission. This is possible because the technology has progressed to the point where the sampling rates¹ of modern recording systems greatly exceed the frequencies of interest. In contrast, optical phase conjugation (OPC) uses electromagnetic waves whose frequencies greatly exceed sampling rates possible with optical detectors.

A similar method being pursued is time reversal (TR) mirror, which is the extension of a phase conjugating mirror. If the temporal Fourier transform of $p(r, t)$ is given by $P(r, \omega)$, then the temporal Fourier transform of $p(r, -t)$ is equal to $P^*(r, \omega)$. Thus, from mathematical point of view, a phase conjugating mirror and a time reversal mirror are the same concepts. However, there is a difference between phase conjugation and time reversal process. The nonlinear interaction of a monochromatic wave in the PC process is opposed to the reversible ability of the transducer array in TR procedure. In other words, due to the time responses of detectors, which are long compared with the period of optical

¹ Sampling rates defines the number of samples per unit of time (usually seconds) taken from a continuous signal to make a discrete signal.

waves, PC needs the nonlinear effects in the medium to conjugate the phase information on monochromatic wave fields [5].

1.1.1. Optical Phase conjugation

Optical phase conjugation (OPC) is a nonlinear optical interaction that creates a precise reversion of the overall phase and sometimes the direction or polarization, of an arbitrary beam of light. In fact, the spatial phase generated in this interaction is the complex conjugate of the spatial phase of the incident wave.

The nonlinear medium in optical phase conjugation acts as a mirror because the mirror can also reverse the direction of propagation of the incident wave, but the difference between ordinary mirrors and optical phase conjugating mirror will be explained later in this section.

The ideal phase conjugating mirror (PCM) can produce the time-reversal effect; so that the time-reversal technique results from the phase conjugation, caused by the PCM (Fig.1.1) [6].

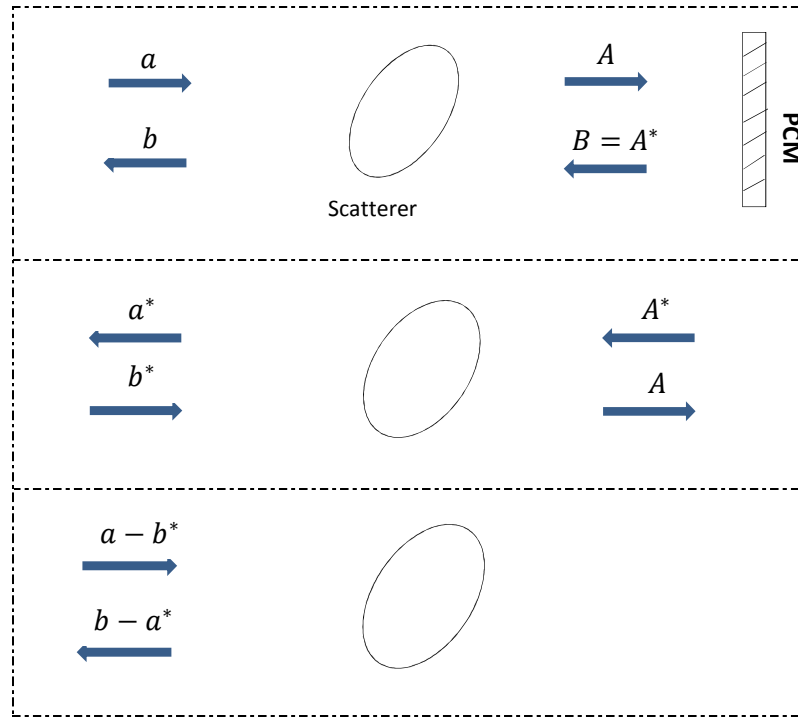


Fig.1. 1. (a) - Schematic view of the PCM experiment; (b) - The time reversal picture; (c) - The difference of (a) and (b), which yields zero incident field everywhere [6]

Phase conjugate mirrors, which have received attention in the literature, [3, 6, 7] may be understood as devices that reflect an incident light ray in a time-reversed sense back along the incident ray path [8].

A difference between reflection from an Optical Phase Conjugating mirror and ordinary mirrors can be shown in (Fig.1.2). As opposed to ordinary optical mirrors, a phase conjugating mirror corrects the effects of a dispersive medium. If an ordinary mirror is replaced by a phase conjugating mirror, the rays are reflected in a time reversed manner. The reflected rays always retrace their paths back through the dispersive medium to reproduce a perfectly reconstructed image of the original object, no matter what the angle of incidence was.

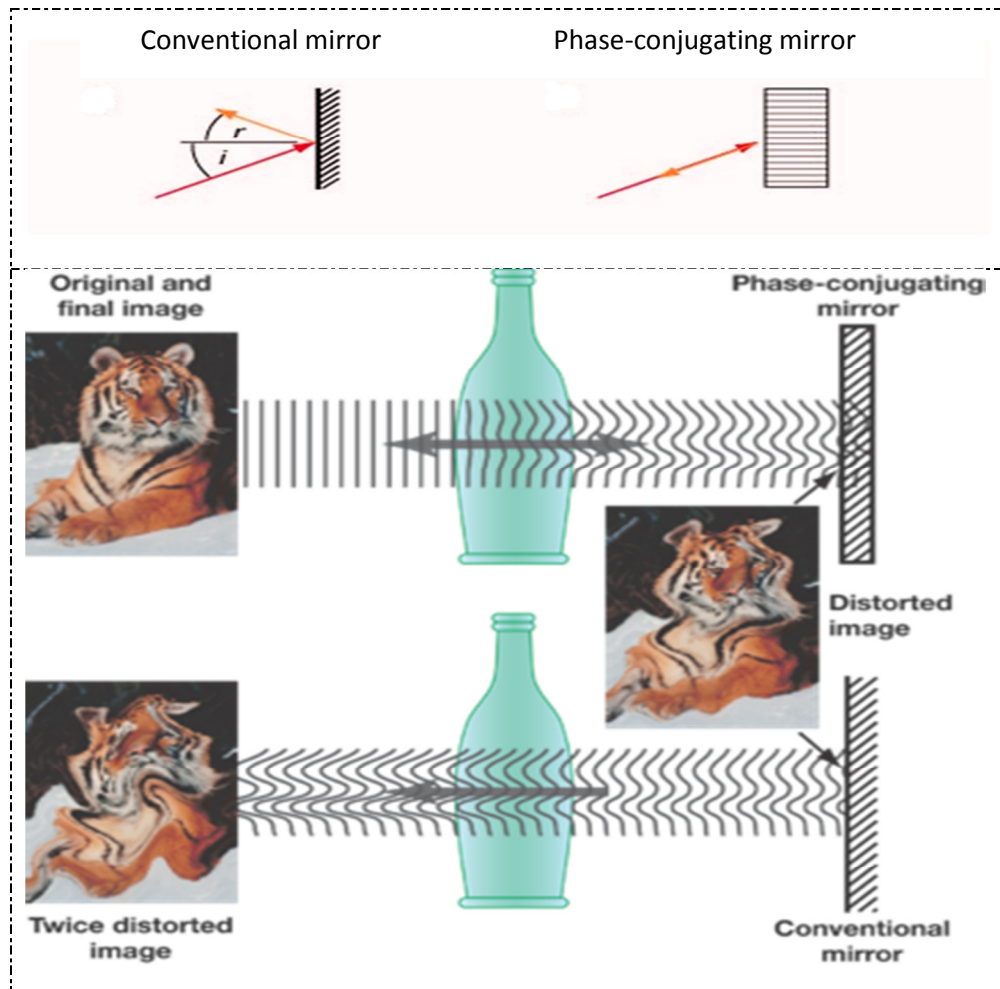


Fig.1. 2. Comparison of a phase conjugate mirror with a conventional mirror[\[http://en.wikipedia.org/wiki/Nonlinear_optics\]](http://en.wikipedia.org/wiki/Nonlinear_optics)

Optical phase conjugation was first discovered in Russia by Zeldovich and colleagues in the early 1970's using Stimulated Brillouin Scattering (SBS), which is a nonlinear optical process [9]. Actually the phase conjugating property was an inherent feature of SBS. The setup used in this experiment is shown in Fig.1.3. The output of a single mode ruby laser was focused into a cell of cylindrical shape to confine the radiation in the transverse dimension. A SBS signal was produced from within this cell. A glass plate that had been carved out in hydrofluoric acid was put in front of the incident beam as an aberrator. Two cameras were used to monitor the phase conjugated intensity distribution of the laser beam [10]. The phase-conjugate beams generated by a (SBS) medium acting as a phase

conjugating mirror (PCM) can compensate wavefront distortion caused by a phase aberrator, such as a laser gain medium [11].

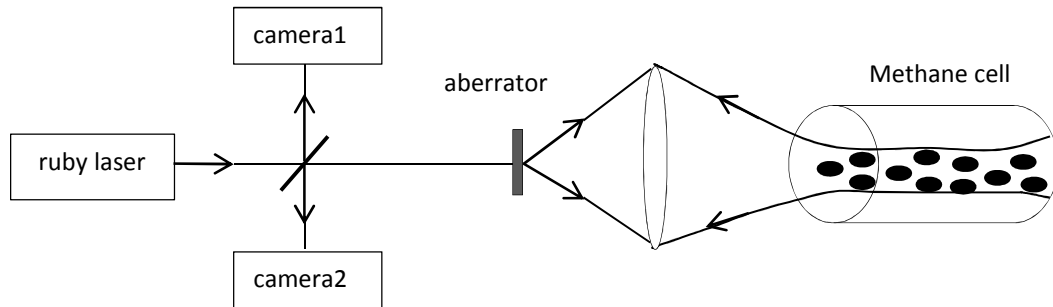


Fig.1. 3. Experimental setup for phase conjugation by stimulated Brillouin scattering [10]

Since then, a great deal of research on optical phase conjugation has been conducted [12], [13], [14].

Due to their unique ‘time reversal’ behavior, optical phase conjugation techniques are useful for many applications and have been applied to many optical processing problems. As an example, phase conjugating mirrors have been used to correct for the dispersion of laser beams due to atmospheric turbulence [15]. In a solid-state laser amplifier, phase distortions increase due to thermal refractive index changes in the laser crystal. If a PCM is used to make the incoming beam pass the laser crystal twice, these distortions become extinct. Hence, PCMs are widely used in the high energy laser systems.

Optical phase conjugation waves can be generated based on various nonlinear optical processes, such as four-wave mixing, special three-wave mixing, backward stimulated scattering, and others [8].

Notably, a unique feature of the optical phase conjugation is that the aberration effect imposed on the forward beam passed through an inhomogeneous or aberrating medium can be automatically removed for the backward beam passed through the same disturbing medium [16].

The enormous growth of applications for non-linear optics techniques during the 1980's and 1990's has been driving research efforts to design many innovative devices and systems using optical phase conjugation techniques, such as amplifiers for non-linear laser spectroscopy, generation of squeezed states in quantum optics, and optical storage and processing systems[17].

The OPC generation process can be visualized as the creation of laser light-induced dynamic grating followed by wavefront reconstruction, and this is also called dynamic holography. The holographic process is another exercise of optical phase conjugation. In the early 1960's, the process of wave front compensation by holographic phase conjugation was demonstrated with confidence. Holographic processes based on temporal and spatial coherence properties of the light source were studied by Amon Yariv[7]. These experiments on dynamic holography allowed recording of basic grating by interfering two beams at the same wavelength. The gratings were due to a change of the absorption or of the index of refraction of the media.

1.1.2. Acoustic Phase conjugation

Starting from the 1980's, similar optical phase conjugation techniques have been proposed in acoustics. Since then, a considerable number of studies on this subject have been reported, ranging from basic research to practical ultrasonic applications. During the last decade, a significant progress in experiments on acoustic PC has been achieved. Both non-linear and linear approaches can be used to produce phase conjugated or time-reversed waves in acoustics.

The concept of phase conjugation is very general and can be applied to waves of different nature. In acoustics, phase conjugation is described in terms of the elastic properties of the medium and the wave interactions involved in the PC process, the space-time structure of the acoustic beams being conjugated, and eventually, the nature of the problem that can be solved using the PC phenomenon. The ability of phase conjugate waves to compensate for phase distortions due to propagation medium could prove very

useful in ultrasonic imaging applications. Some examples of these applications are reviewed further in this section.

Also referencing in brief, creating phase conjugated waves using PZT ceramics as a nonlinear piezoelectric medium has been studied by M. Ohno *et al* [18]. In the experimental part, the variation of sound velocity in PZT ceramics was measured in presence of electric fields. Then the phase conjugate reflectivity was evaluated knowing the dependency on sound velocity and electric field. This experimental result suggests that the interaction between the incident acoustic wave at ω and applied external pumping electric field at 2ω could lead to the excitation of acoustic phase conjugated waves in a nonlinear piezoelectric medium at frequency ω [18].

Industrial applications, such as nondestructive evaluation, benefit from the ability of high frequency ultrasound to penetrate into metallic and ceramic samples in order to obtain information such as grain size and the existence of flaws or other defects [19]. In the method of Fink *et al.*, a short ultrasound pulse is transmitted towards the sample and the reflected signal from the boundaries is recorded. Then, using the phase conjugation or time reversal techniques, the method improves the focusing of the ultrasound, particularly for samples of complex shapes, and the detection of small defects becomes possible with greater certainty [17].

Ken Yamamoto *et al.* [19] also applied phase conjugation based on nonlinear piezoelectricity to ultrasonic imaging systems. It was demonstrated that the phase conjugation method can compensate for distortion and improve image quality for samples with uneven surface.

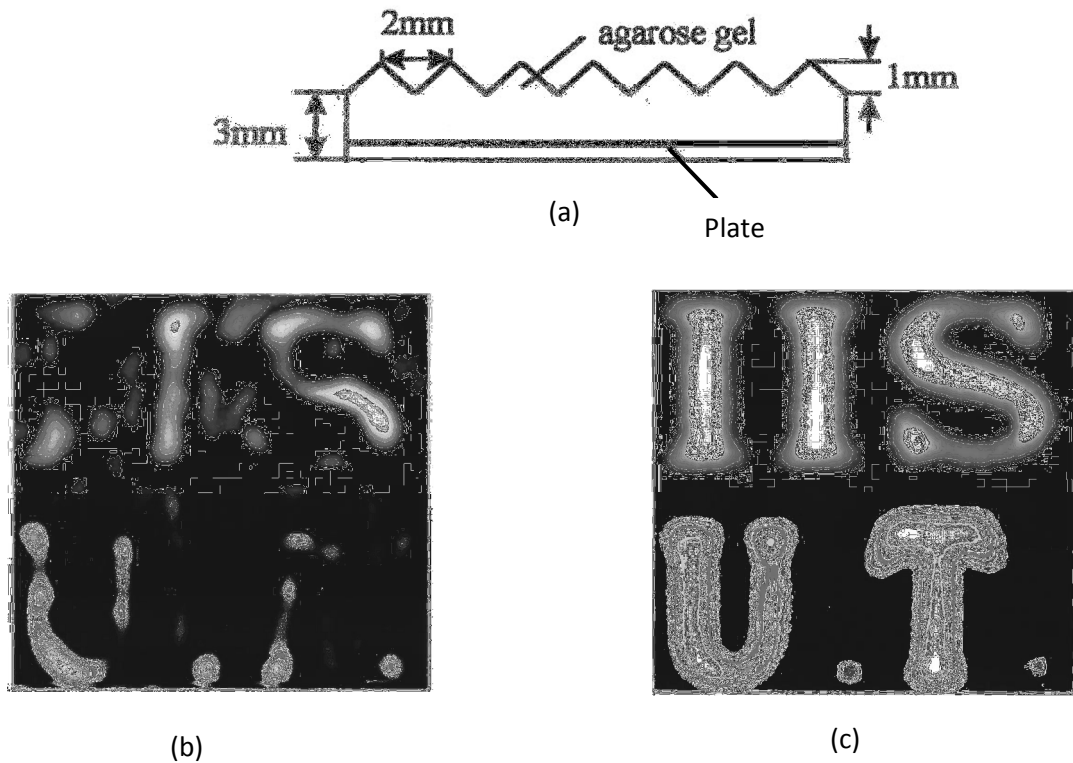


Fig.1. 4. (a) Cross section of the sample (b) Strongly destroyed conventional image, because of the rough surface (c) letters are easily recognizable in conjugate image[19].

The samples in this experiment were made of agarose gel with acoustic velocity of 1700 m/s. A pyramid array pattern was created on the sample surface, each pyramid having 2 mm length and 1 mm height. The target was a 10-mm-thick stainless steel plate with engraved letters “I I S U. T.”. The ultrasonic image processing was applied in two different ways: the first one was a conventional method which detected the reflected ultrasonic waves, and the other one was detecting the phase conjugate waves in a reciprocal manner. The results presented in Fig.1.4 show that because of the rough surface, the conventional image is completely destroyed. On the other hand, in the phase conjugate image the letters are clearly recognizable [19]. As another example of using phase conjugation in an inhomogeneous medium O.Ikeda [20] proposed a diffraction limited imaging method which was based on the phase conjugation procedure as a way to improve the quality of images of ultrasonic objects in a heterogeneous medium. As shown in Fig.1.5, some frequency-dependent reflectors were placed in the area of

interest. After receiving the ultrasonic signal with all elements of the transmit-receive array it was phase conjugated in n th step and retransmitted to the medium to reflect again in $(n+1)$ th step. This iteration continued until convergence, and the process was repeated for each of several frequencies. The signal processing was performed in a computer, and the converged phase conjugated wave was scanned to get an image.

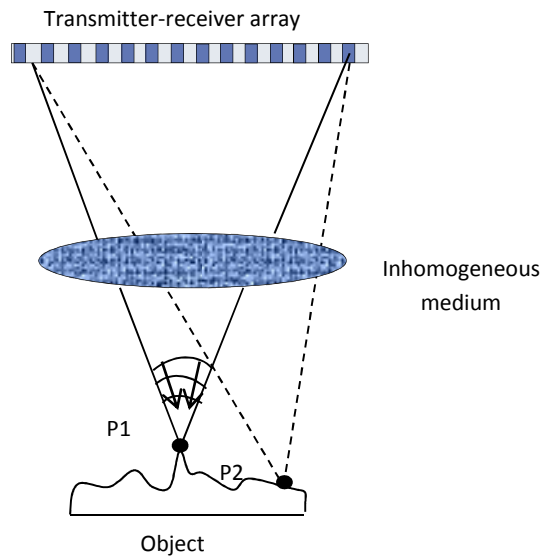


Fig.1. 5. Figure of ultrasound imaging method with presenting of heterogeneous medium, where P_n represents the frequency dependent reflectors in viewing area [20]

Also worth mentioning are the development of a supercritical parametric technique for acoustic wave phase conjugation and the interest in the implementation of nonlinear wave phenomena in acoustic imaging systems for medical purposes.

The method of Yu. Pyl'nov [21] is an example of harmonic imaging by means of nonlinear propagation of a phase conjugate wave. Harmonic imaging in acoustic C-scan microscopy using phase conjugated magnetoelastic waves is investigated in this study. Based on this demonstration, using the nonlinearity of biological tissues brings fundamental improvement of resolution of the imaging systems that can be used in the medical application field.

Phase conjugation may offer solutions to several problems in underwater acoustics communication. Refraction caused by oceanic structure could vary from centimeters to tens of kilometers and have strong effects on propagation [22]. A great amount of literature exists on the underwater acoustics applications [23,24]. In particular, in 1998, Kuperman *et al.* implemented a time reversal mirror (or phase conjugating array) for monitoring the Mediterranean Sea surface and achieved spatial focusing between a source and array separated by over 6 kilometers a distance [23]. In the next set of experiments, they achieved spatial focusing by extending the distance over 30 km and showed that successful refocusing of probe-source pulses up to 1 week old to their original location [25]. Since these groundbreaking experiments, further developments have been made, especially in the field of underwater acoustic communication.

1.1.3. Time Reversal Mirror (TRM)

The method of acoustic time reversal has drawn considerable interest over the last twenty years since the initial demonstration of its capability to form convergent fields on a localized target. Time reversal of ultrasonic field describes a way to focus an acoustic field through an inhomogeneous medium on a reflective target, which acts as an acoustic source after being exposed to sound waves. A Time-Reversal-Mirror (TRM) is the device used to show an original solution to this problem. Initially, time reversal was introduced as a technique that consisted of transmitting a signal into a medium that contains scatterers, recording the scattered acoustic field by the array, time reversing it and then retransmitting back to the medium. Due to time reversal invariance, the retransmitted signal refocuses on the scatterers. If there were several reflectors in the medium the signal would usually focus on the transcendent scatterer and the other reflectors would receive minimal energy [26].

The time reversal method uses properties of the linear piezoelectric transducers that can transmit and receive acoustic signals and are able to measure the sound wave parameters immediately [27]. Each transducer has its own electronic channel board, composed of:

receiving amplifier, analog-digital converter, digital memories, and a programmable generator that is able to compound the temporal reversed signal saved in the memory. In this method, each transducer element of the array positioned at r_i , receives the acoustic pressure field $p(r_i, t)$. The collected data are digitized and saved during a time interval T . Then the acoustic pressure field is reemitted by the same transducer elements in a reverse time order (i.e. the slowest signals which had arrived last are sent back first). This is equal to the emission of $p(r_i, T - t)$ [27].

The waves are assumed to propagate in a homogeneous and isotropic medium. The wave equation for this type of medium is given by:

$$\nabla \cdot \left(\frac{\vec{\nabla}(p(\vec{r}, t))}{\rho(\vec{r})} \right) - \frac{1}{\rho(\vec{r})c^2(\vec{r})} \frac{\partial^2 p(\vec{r}, t)}{\partial t^2} = 0 \quad 1.1$$

where $p(\vec{r}, t)$ describes the pressure field, and $\rho(\vec{r})$ and $c(\vec{r})$ are the density and the sound velocity in the medium, respectively. Any solution $p(\vec{r}, t)$ also implies a time reversed solution $p(\vec{r}, -t)$. In fact, the time reversal property is true for any differential equation containing only even order derivatives in terms of t .

Time reversal (TR) is the process of recording, time-reversing, and re-propagating the signal. A time reversal mirror can be created using an array of receivers and playing back the signals they absorb, but in a time reversed sequence. More specifically, the TRM procedure generates the real acoustic image of the primary source, which is contrary to an ordinary mirror that makes a virtual image of the acoustic object.

In the real situation, reversing the time implies producing tentatively a back-propagated duplicate from a forward propagation pressure field. Based on Huygens's principle, time-reversal can replace the mirror of the time variable in a closed surface, which encloses the initial source position [28]. In one of the first experiments, a closed cavity contained a source which was placed in inhomogeneous medium surrounded by transducers. The

transmitted sound by the source was scattered by an inhomogeneity in the cavity and the surrounding transducers recorded this scattered ultrasound field. As shown in (Fig.1.6), upon emitting the time-reversed version of the recording, the time reversed field back propagated inside the surface and focused on the initial source location [26]. Another experiment showed that if the medium is weakly homogeneous, then a time-reversal mirror can generate a focal spot comparable to that of a closed-cavity, which is a difficult achievement in practice [29].

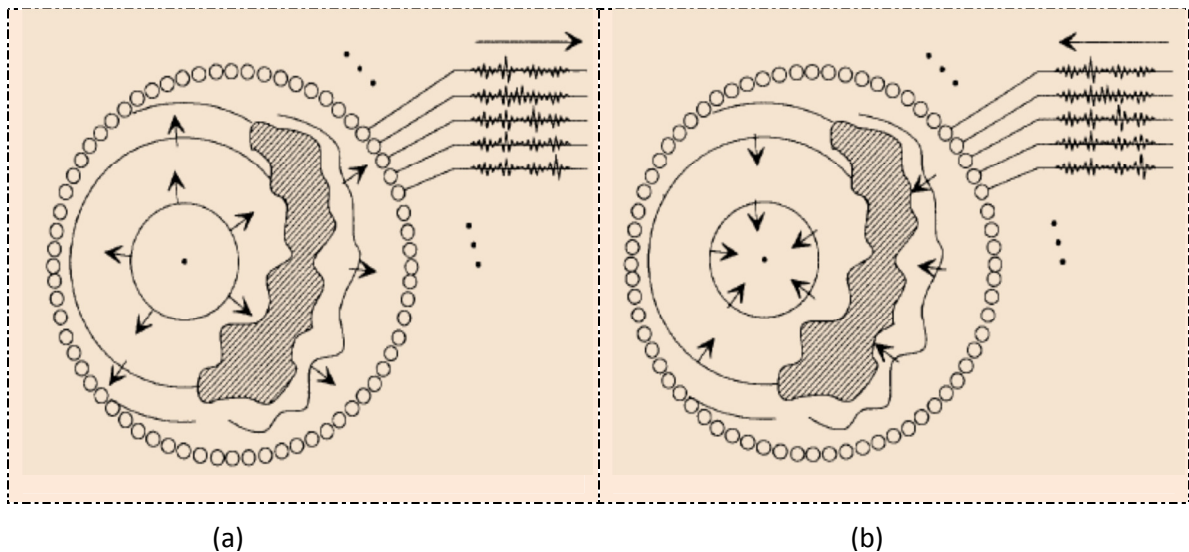


Fig.1. 6. Time reversal cavity.(a) Recording step: the distorted pressure field by an aberrating mirror is recorded on surrounding transducers .(b)Back propagation step: the time reversed signal reradiates into cavity surface and focuses on the source [26].

In 1991, Prada, Wu, and Fink [30] discussed theoretical work on time reversal mirrors along with experimental results. The time reversal mirror used consisted of 64 transducer elements in concave alignment. It was illustrated that time reversing and reemitting signals transmitted by a hydrophone placed away from the array resulted in focusing at the initial location of the hydrophone; this effect is equivalent to that described in (Fig.1.8).

The same group also conducted another experiment regarding an iteratively time reversed signal backscattered by two different thin wire targets placed $z = 90$ mm away from the array, resulting in spatial focusing on the larger and more reflective of the two (Fig.1.7).

In this experiment, the echoes from the two targets were recorded after first insonation, and then the recorded signals were time-reversed and retransmitted. These waves were propagated, and the new pattern was measured by scanning the plane $z = 110$ mm with a hydrophone [31]. The process was iterated: the new echoes from the wires were recorded, time-reversed and retransmitted, etc. By repetition of this process, the wire which reflects less energy receives a weaker time-reversed wave. As shown in Fig.1.7-(d) the small wire is no longer visible after the last emission [31].

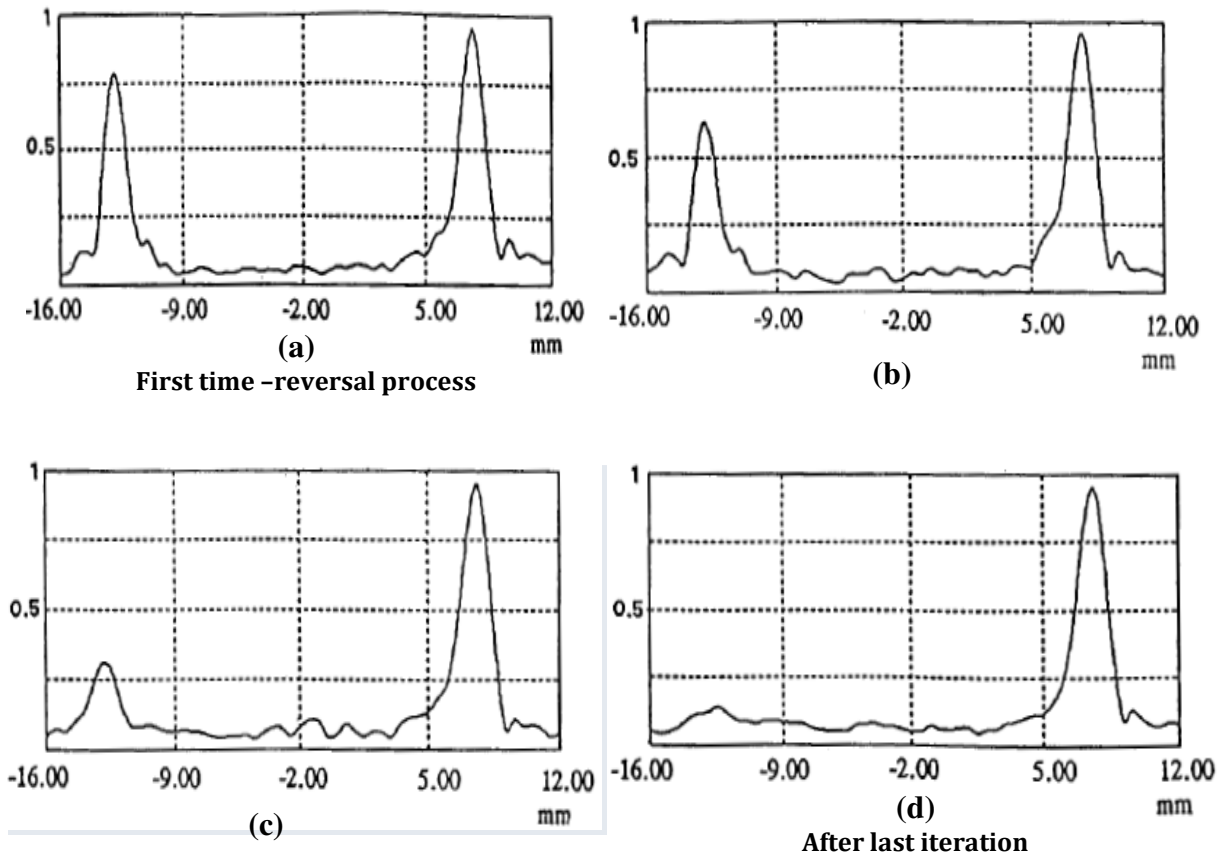


Fig.1. 7. The iterative time reversal process in the case of two wires.(a), (b),(c) and (d)represent the pressure result in the observation plane after time reversal iterative process[31]

A further discussion of general principles of time reversal is presented by Fink *et al.* in a set of papers [25, 31, 36] and a review letter [5] and improved over last twenty years. As mentioned before, analysis of time reversal focusing at a fundamental level, through an

inhomogeneous medium was also investigated by Fink *et al.* As illustrated in Fig.1.8, the main steps involved in time reversal focusing are as follows: [32]

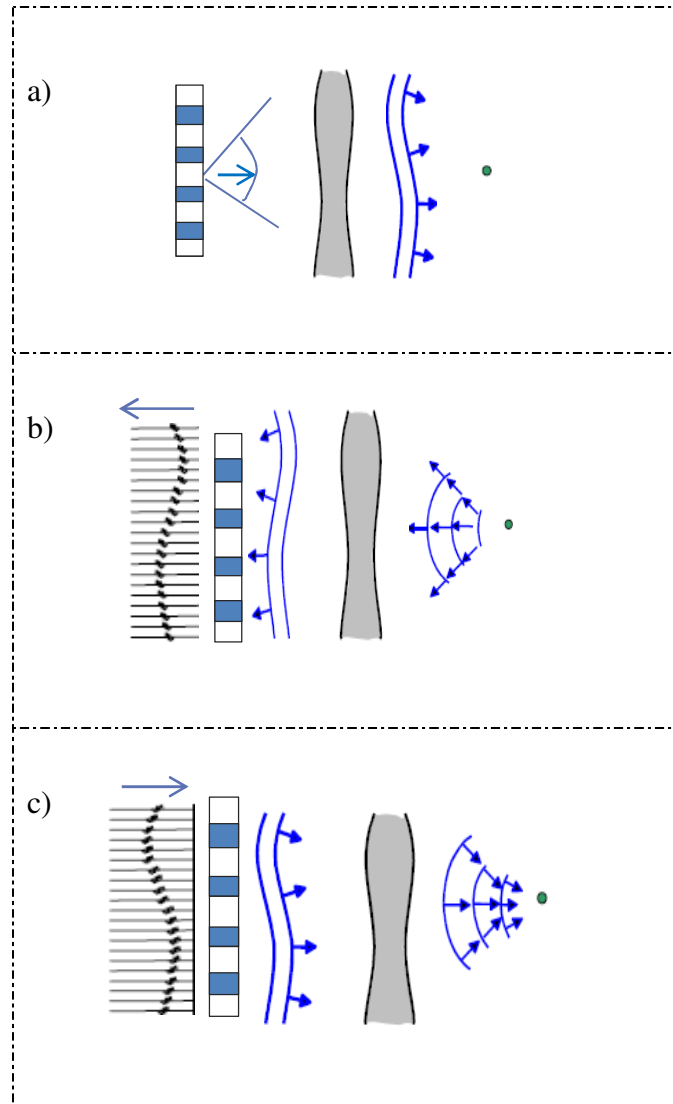


Fig.1. 8 . Schematic of the TRM focusing through aberrating media. (a) Illumination step that shows transmission of the wave front from the array through the inhomogeneous medium toward the target. The target emits a backscattered pressure field that propagates through the medium and is distorted; (b) represents the step of recording the backscattered pressure field by the transducer array; (c) At the last step, the transducer array transmits time reversed acoustic field back to inhomogeneous medium to focus on the target [26].

1. The first step is the illumination part that includes emitting the wave from the transducer array through the heterogeneous medium towards the target. The target produces a scattered and distorted acoustic field that propagates in the medium.

2. At the recording step, the backscattered acoustic field is recorded by each transducer element of the array.

3. At the final step, the array of transducers reradiates the time reversed pressure field back into the inhomogeneous medium to focus on the target.

Regarding the application of time reversal for the detection and identification of targets, Gruber *et al.* [33] accomplished TR imaging using a multiple signal arrangement method that can be used in more general nonlinear medium scattering problems with multiple scattering between the targets. In that study, the array of time-harmonic transceivers was considered assuming that each transceiver can emit into the reciprocal propagation medium and also that the point targets have unknown positions and scattering amplitudes.

E.Kerbrat *et al.* [34] used a time reversal operator to detect flaws in inhomogeneous media. In that experiment, the target was a cylindrical titanium sample with defects, and a set of signals was applied to the transducer array. The defects of different size are located at a depth of 140 mm and spaced 15 mm apart as shown in Fig.1.9. The sample was immersed in water. After applying three time reversal steps, the wave field was focused separately on the defects whose positions were unknown (Fig.1.10).

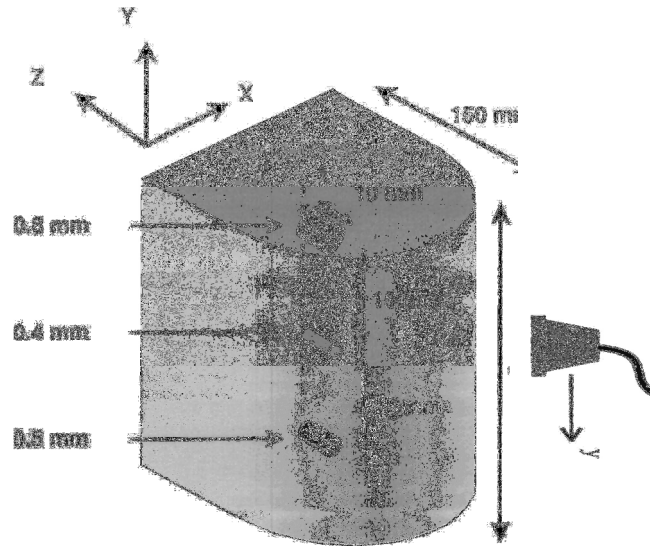


Fig.1. 9. Translation of the array along the y axis for titanium sample [34].

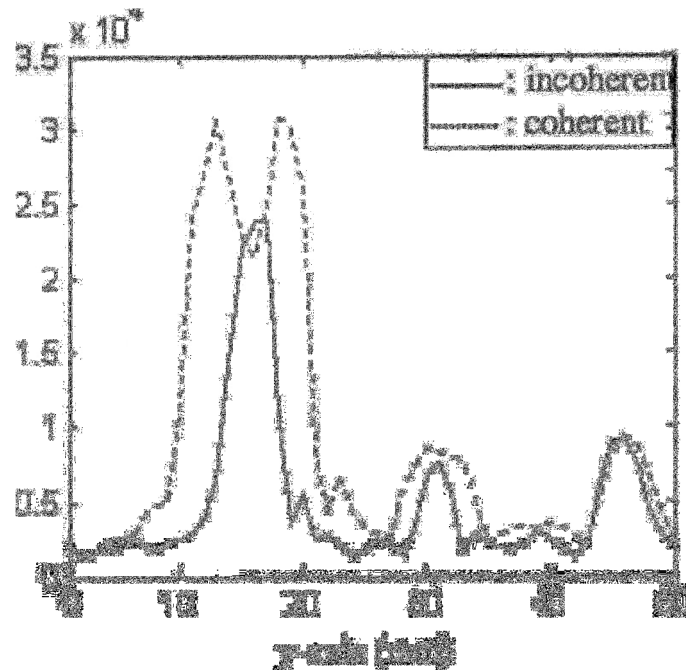


Fig.1. 10. B-Scan (incoherent and the coherent linear summations) measured with the TRM at the second iteration along the y axis to detect the three defects [34].

Investigation of limitations of the TR technique in solid media, when the transducer is attached to the surface, was conducted by M Griffa *et al* [35]. Based on this study, the transducer size and the presence of both longitudinal and shear waves in the solid significantly affect the time reversal process. Even with this limitation, it was demonstrated that TR methods are robust enough to still work successfully and be able of reconstruct the main features of the source signal.

Medical ultrasound uses high frequency sound waves in the megahertz range, whose echoes from the tissues are used to generate images. While it may give less accurate results compared to other technique such as MRI or CT, it has many benefits making it an ideal technique in specific situations, in particular, in the real-time imaging of moving structures, for tissue characterization, and as a substitute to ionizing radiation. Imaging ultrasound is safe to use and does not appear to cause any biological side effects. It is also inexpensive and quick to perform.

The ability of precise focusing of ultrasonic waves is an essential aspect of most medical applications of ultrasound. Refraction, reflection and scattering of ultrasound in inhomogeneous media can distort a focused ultrasound field and restrict the ability of focusing in biological tissue. There are numerous methods of developing ultrasonic focusing in inhomogeneous media based on phase and amplitude corrections in the focusing method, but most of them are too difficult to accomplish [41]. However, Time-Reversal Acoustics (TRA) is a simple and appropriate technique of focusing acoustic energy in inhomogeneous media.

Below is a review of some of the main medical applications involving the time reversal acoustic technique. As an example, time reversal procedure could use the high amplitude pressure fields (lithotripsy) to solve the problem of real time tracking and destruction of kidney stones. An iterative mode of TRM process yields tracking kidney stones during lithotripsy procedure [36].

In lithotripsy, the aim is to find the location of the most reflective target among others and destroy it. In this procedure one part of the array emits a pulse to illuminate the desired area through any aberrating medium. The most reflective stone could be chosen among other stones and organ tissue. Hence, the reflected wave from the stone is recorded by the same array and then time-reversed and re-emitted. The highest amplitude wavefront that comes up by the reradiated time reversed wave illuminates the most reflective stone (Fig.1.11). In this case, the time-reversal technique can be iterated. After some iteration the most reflective stone is detected and a high amplitude signal is used to demolish it [32].

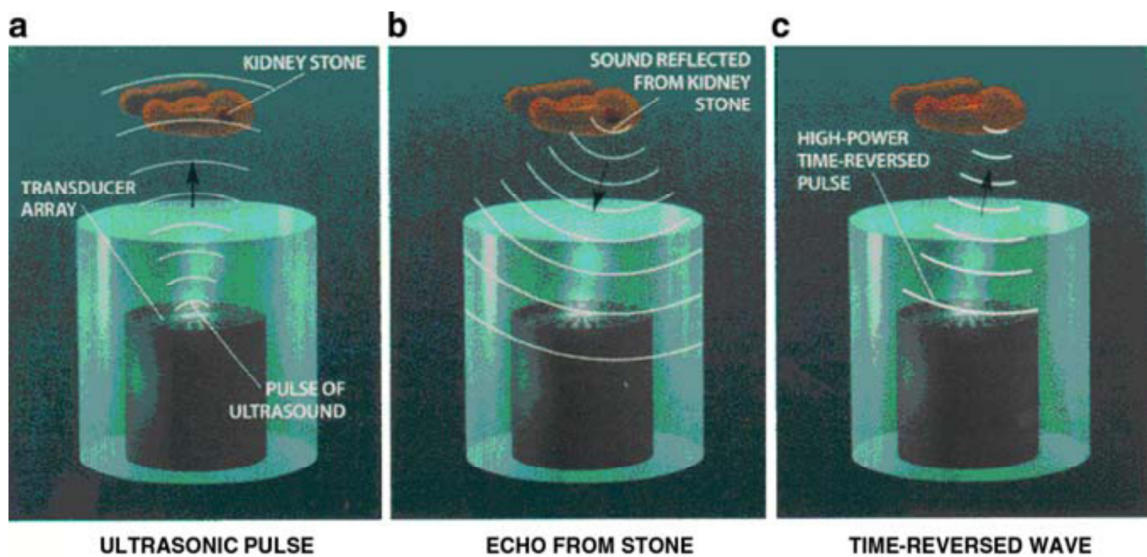


Fig.1. 11. Lithotripsy Application: Using time reversal in real time tracking and auto-focusing on a kidney stone [37].

In breast ultrasound imaging, as in many medical ultrasound applications, the heterogeneity of the breast degrades the quality of focusing. As recently reported by Robert *et al* [38], detection of a tiny calcification in heterogeneous human breast tissue using time reversal process allows one to achieve better accuracy than conventional echographic imaging.

The TRM technique was used by Mickael Tanter *et al.* [39] to focus pulsed ultrasonic waves through the human skull bone in order to cure brain tumors. However, because of the high ultrasonic attenuation in the skull, the capability of the time reversal procedure decreases. In this experiment a 1-D cylindrical array of 128 piezoelectric elements of transducers operating at 1.5 MHz was used. The array pitch was 1.2 mm and the elements were arranged on a cylindrical surface of 100 mm radius. In this process, as shown in Fig.1.12, the single element starts to emit the signal and the pressure field of this source is stored on the 128 elements of the array. Then these signals are time reversed and the all elements of the array reemitted at the same time. The single element was used as a receiver to scan the wave field along the x axis [39, 40].

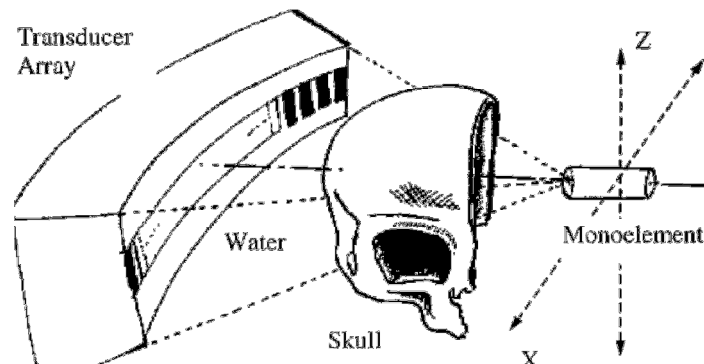


Fig.1. 12 . Aberration time reversal focusing in presence of the skull [39].

Recently, George K.Lewis *et al.* [41] suggested a method to deliver a medicine into the brain by combining time reversal acoustic (TRA) with convection enhanced delivery (CED). Convection Enhanced Delivery (CED) is a way to transfer a chemical factor directly to the brain. TRA method requires a pointer in the target domain. The hydrophone plays the role of a “smart needle” in the CED infusion. Placing the transducer at the tip of the needle allows transferring signals and forms the TRA process between the TRA reverberators/transmitters and part of the brain where the drug is infused. This study developed the precise focusing of ultrasound in tissue with minimum damage to healthy tissues (Fig.1.13).

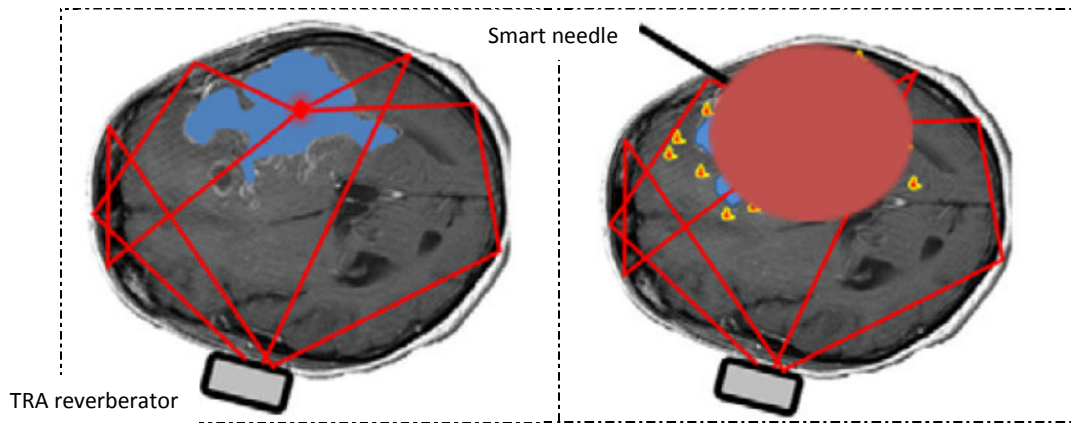


Fig.1. 13 . The application of the Time-Reversal Acoustic (TRA) method for drug delivery in the brain. (a) A simple reverberator put on the outside of the skull and the TRA method used to focus ultrasound intensity, (b) improving distribution and infusion control by TRA_UCED [41].

1.2. Transcranial imaging

Transcranial ultrasound is the application of ultrasound techniques through the intact skull, where imaging methods are involved. In general the skull bone is too thick to penetrate with ultrasound, but there exist so called acoustic windows where there is a natural opening, or the bone is adequately thin to pass a considerable percentage of the incident ultrasound energy. However, recent work demonstrates the possibility of transmitting lower ultrasonic frequencies through a larger region of skull bone than just the temporal bone window [42, 43, 44]. These recent papers prove that the transmitted ultrasound intensity depends on the skull thickness and mass density [45].

Although ultrasound is real-time, portable, non-invasive, and low cost, from the neurologist's point of view, the accuracy of image quality of transcranial ultrasound is not good enough compared to CT, MRI, and angiographic imaging. If transcranial ultrasound image quality could be improved, the potential public health impact would be immense. Several noninvasive techniques have been proposed to reduce the aberration caused by the skull. Some of them use an alternative model (magnetic resonance imaging (MRI) or x-ray computed tomography (CT)) to get information about the skull and use the

information to estimate the expected distortions. However, simpler approaches are also studied by scientists for potential enhancement of image quality through the skull.

Hynynen *et al.* initially proposed that adequate aberration correction could be achieved using the skull thickness, as measured by MRI, and a constant sound speed value based on an average of the speed of sound in each of 3 layers of the skull [43,46]. This approach improved transcranial focusing however, significant sidelobes were still present. It was also recommended that by using different speeds of sound for different bone densities within the skull a considerable improvement in correcting aberrations could be obtained. This requires using CT rather MRI due to its ability to evaluate both skull thickness and density.

An investigation of the defocusing effect of the skull and the resulting degradation of the quality of ultrasound brain images was first conducted by White *et al.* The presence of the skull causes phase shifting of the wavefront and distortion of the pressure field inside the skull. This distortion prevents the ability to produce a coherent focused pressure field inside the brain [47].

Additionally, Clement *et al* [48], suggested useful methods for reconstructing spectral ultrasound images using pulsed and multi-burst signals with a curved broadband 1.1 MHz transducer. This work proved how the strong scattering sources could be localizing within a brain phantom through formaldehyde-fixed human skull bone. Although lower frequencies result in lower axial resolution, the feasibility of propagating ultrasound through the skull at greater depths than previously attempted offer opportunities for monitoring structural changes. These results suggest that further studies investigating weakly scattered ultrasound wave sources within the brain should be undertaken. An example of a diagnostic application would be distinguishing a fluid-filled ventricle from the brain tissue and the skull bone.

In a preliminary study, Hynynen *et al* [43] expanded on the idea of propagating energy across a larger area of the skull. A large-aperture model was designed to surround the entire skull surface and maximize the ratio between the focal intensity and the energy per

unit area at the skull interfaces. Using this design allowed therapeutic levels of ultrasound energy to be transferred into the brain non-invasively. This approach improved transcranial focusing, however, significant sidelobes were still present.

Vignon *et al* [49] proposed another technique that approximated transcranial aberration by applying two identical linear arrays of 128 elements on both sides of the skull. The attenuation and phase shift locally generated by each bone window were estimated at each frequency and used to correct the wave fronts, achieving precise focus within the skull. However, this technique has a restriction because of the requirement of using two identical arrays on either side of the skull.

Another noninvasive transcranial focusing approach is point-target based aberration correction. Different point-target methods have been proposed [50,51,25]. All point-target techniques rely on the distributed point scatterers/point sources in the region of interest. Point-target techniques are available for different biomedical application. (e.g. kidney or gallbladder stones).

1.3. Acoustical properties of human skull bone

The composite structure of skull bone causes significant signal loss due to reflection, refraction, and phase shift and frequency dependent attenuation. In ultrasonic imaging techniques, familiarity with ultrasonic beam aberration caused by the skull is important for improving the image resolution. The human skull consists of three different layers, (outer table, diploe, inner table). The outer table is thick and tough compact bone, which is gently curved. This layer causes the main specular reflection of the ultrasound energy [52]. The middle layer, referred to as the diploe, consists of bone marrow (the flexible tissue found in the interior of bones and in humans, which produces new blood cells) and cancellous bone and only exists in the adult skull. This layer is a very heterogeneous scattering medium penetrated with blood vessels to keep the tissue alive [52]. The inner table is also compact bone, but it is thinner, denser, and more brittle than

the outer layer. In general, the inner curved surface of the inner table is not parallel to the external area of the outer table.

The inner and outer tables have attenuation coefficients of 2.8 dB/(cm MHz), compared to 25-70 dB/(cm MHz) in the diploe [52]. Assuming average thicknesses of 1.49, 2.29, and 1.46 mm for the three layers, respectively, this amounts to attenuation of 23.5 dB/MHz for pulse-echo imaging surface of the outer table.

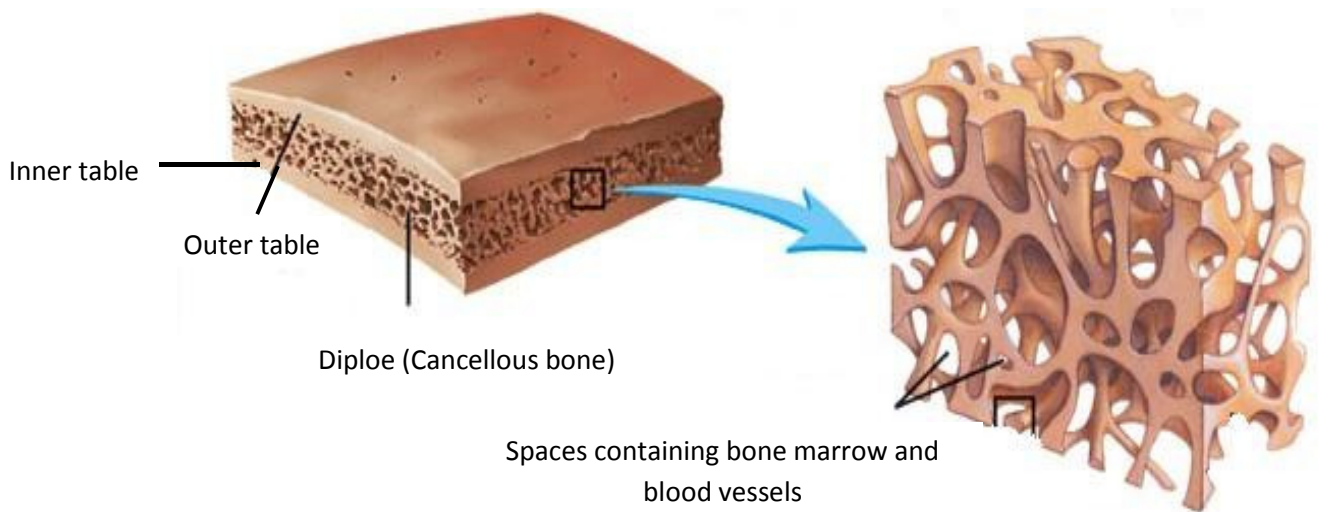


Fig.1. 14 . Three different layers of adult human skull
[<http://www.rci.rutgers.edu/~uzwiak/AnatPhys/APFallLect8.html>]

1.4. Conclusion

This chapter provides a review of the applications of ultrasound in various areas. This review was based on over 55 publications cited as references. The first half of the chapter focuses on the aspects of phase conjugation in optics. Then, a transition to acoustics is made with a practical explanation of the technique. Also presented are important medical, industrial, and underwater communication applications of time reversal that could be also called ultrasonic phase conjugation techniques.

The remaining part of the chapter focuses on using acoustic phase conjugation (time reversal) in biomedical imaging systems in inhomogeneous media, especially in transcranial imaging. The number of articles discussing the problem of image reconstruction through the skull was smaller compared to other topics.

The objective of this study is to develop a new imaging approach for reconstruction of foreign objects inside the brain through a simulated skull model, using a harmonic phase conjugation technique.

Chapter2: THEORETICAL REVIEW

Introduction

In this chapter the theoretical concepts and principles that were used in developing and analysing the algorithm, such as wave propagation characteristics, diffraction, reflection and transmission concepts, will be explained.

Furthermore, the information presented here is based on some simplifications such as linearity and homogeneity of brain, which is assumed to be homogenous media within good approximation, due to similar acoustical properties of brain tissues and water.

Some concepts such as non-linearity, shear waves and non-isotropic media are outside the scope of this thesis. In terms of linearity of acoustics the sound wave velocity does not change and the amplitude is damped due to diffraction and attenuation of the media. In contrast, if the amplitude increases, the amplitude dependence cannot be neglected any longer. As well, the shear wave was not considered in this study as it is highly attenuative in skull and brain tissue. So this study presents work on an image reconstruction that utilizes only longitudinal wave propagation through the medium [53].

2.1. Acoustic Waves

Acoustical waves transfer energy and pressure through a medium (solid, liquid or gas) by vibrating the particles in the medium. When an acoustic wave travels through a medium only the energy propagates. The rate at which the acoustical wave vibrates the particles is its frequency. Ultrasound consists of acoustical waves which have frequencies greater than 20 kHz; the upper limit of human hearing. It continues up into the MHz range and finally reaches its maximum at around 1 GHz, which is defined as the hypersonic regime. The approximate distribution of these frequency ranges are shown in Fig 2.1. [54].

In general, waves are defined by the following main characteristics:

Amplitude: Amplitude addresses the amount of energy that a mechanical wave carries.

Phase: Phase denotes the particular point in the cycle of a waveform, measured as an angle in degrees. The phase shift describes fraction of a cycle to the left or right the wave slides.

Wavelength (λ): The wavelength is the distance from the top of one crest of the wave to the next.

Frequency (f): The frequency of a sound wave is the number of cycles which pass a point each second.

Wave speed (v): the speed is the distance traveled by a given point on the wave (such as a crest) in a given interval of time.



Fig.2. 1. Frequency ranges corresponding to ultrasound process

2.2. Wave propagation in linear viscous media

Acoustics is usually concerned with small amplitude phenomena, so a linear description is usually applicable. The linear propagation of an acoustic wave results from the isotropic elastic properties of the liquid and from the thermodynamic principle point of view, the viscosity enter into the versions of the relative equations that apply to fluid. Details of some important wave propagation principles follow.

2.2.1. Huygens' Principle

This principle, which is based on the wave theory of light and proposed by the physicist Christiaan Huygens (1629-1695), initially expressed that:

Each point of a wave front is in fact the center of a new disturbance and the source of a secondary wavelet of the spherical wave that distributes the energy back in to the shadow zone with a speed equal to the speed of propagation of the waves, as shown in Fig.2.2. Additionally, the sound energy can be attained at any point source in the shadow zone by summing the contribution of all of the point sources on the wavefronts. This view of wave propagation helps us better understand a variety of wave phenomena, such as diffraction [55, 56].

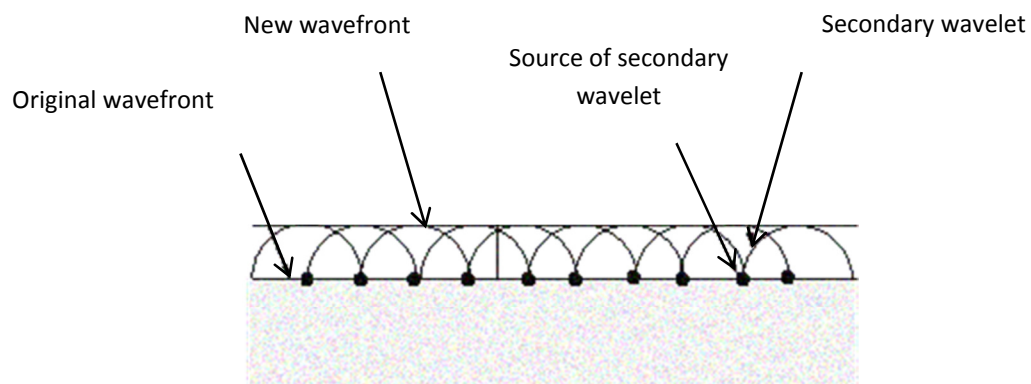


Fig.2. 2. Huygens's principle

2.2.2. Diffraction

The Huygens-Fresnel Principle is used to describe the acoustical diffraction method. Based on this technique, the acoustical intensity reaching a receiver from an acoustic source after being diffracted by a boundary, is estimated as the superposition of the wavelets at further points [57, 58].

As shown in Fig.2.3, when a wavefront goes through an aperture every point of the wave within the aperture can be counted as a point source, creating its own spherical field outward from the aperture. At the aperture, the interference pattern of such spherical fields makes the center of the wave front have greater intensity, with declining behavior as the edges are approached.

This explains why the light through an aperture does not create a good image of the aperture on a screen. The edges "spread out" based upon this principle.

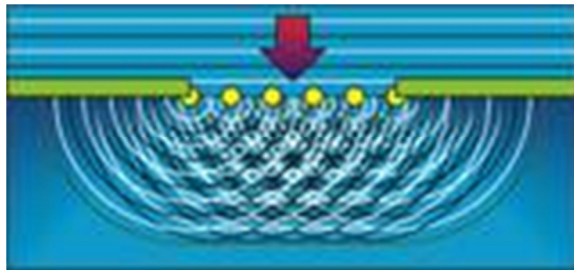


Fig.2. 3. An illustration of Huygens 'Principle of diffraction
[<http://www.absoluteastronomy.com/topics>]

Diffraction is the slight bending of sound as it passes around the edge of an object. The amount of bending depends on the size of the wavelength of sound to the size of the opening. An obstacle very much smaller than the wavelength of sound allows the wave front to pass mainly unperturbed and an obstacle larger than the wavelength forms a shadow that tries to be irradiated from sources on the wavefronts of sound that pass by the obstacle [58].

Using the single slit could be the simplest example in diffraction. When plane waves of sound encounter a solid obstacle with a slit, diffraction depends on the size of the opening. A narrower slit would produce more diffraction and a greater width of the beam. Fig.2.4 shows that using the narrower slit yields a greater broadening of the beam [58].

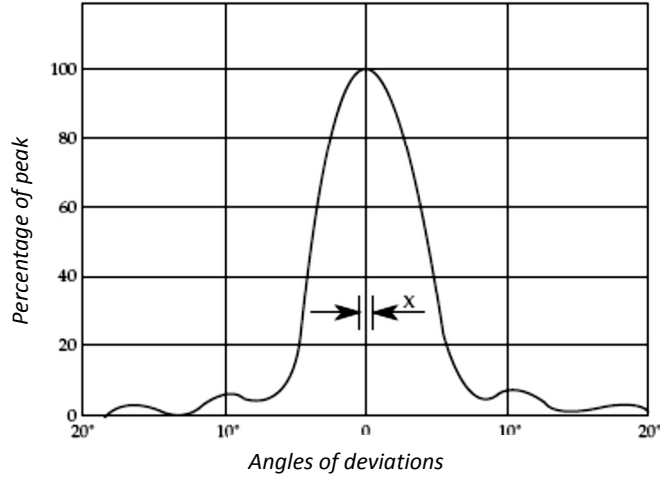


Fig.2. 4. Narrower slit make wider beam [58]

2.2.3. The Rayleigh-Sommerfeld equation of diffraction

The Rayleigh-Sommerfeld diffraction equations are formulas that describe the field distribution which use the surface integrals over the specified boundary. In an ideal approach for linear distribution, a homogeneous and isotropic liquid is presumed and some assumptions are made based on the boundary conditions. These conditions yield Rayleigh-Sommerfeld equations that represent the field distribution in regard to surface integral over the specific boundary [59].

The basic structure of wave equations in a homogeneous viscous medium is:

$$\nabla^2 \Phi - \kappa \rho_0 \frac{\partial^2 \Phi}{\partial t^2} + \kappa \left(\frac{4}{3} \mu + \mu_B \right) \frac{\partial}{\partial t} (\nabla^2 \Phi) = -f(x, t) \quad 2.2$$

Where κ is adiabatic compressibility, ρ_0 is the density of the medium, $f(x,t)$ is a source distribution, ∇^2 is Laplace operator and the propagation speed is equal to : $c = \frac{1}{\sqrt{\kappa \rho_0}}$

Consequently, equation 2.1 can be written as:

$$\nabla^2 \Phi - \frac{1}{c^2} \frac{\partial^2 \Phi}{\partial t^2} + \kappa \left(\frac{4}{3} \mu + \mu_B \right) \frac{\partial}{\partial t} (\nabla^2 \Phi) = -f(x, t) \quad 2.2$$

To solve this equation it is easier to transform equation 2.2 to the frequency domain and this transformation can be completed by using the Fourier transform, which is defined by: [59]

$$\begin{aligned}\Phi(x, \omega) &= \int_{-\infty}^{+\infty} \Phi(x, t)e^{-i\omega t} dt \\ f(x, \omega) &= \int_{-\infty}^{+\infty} f(x, t)e^{-i\omega t} dt\end{aligned}\tag{2.3}$$

Inserting the equation 2.3 into equation 2.2 yields the *inhomogeneous Helmholtz wave equation*

$$(\nabla^2 + \underline{k}^2)\Phi(x, \omega) = -f(x, \omega)\tag{2.4}$$

Here $k = \frac{\omega}{c}$ is the wave number affiliated with frequency ω .

Calculating the field distribution based on a source distribution $f(x,t)$, which is surrounded by surface S_0 , simplifies to computing the Helmholtz equation by applying the boundary conditions on S_0 (Fig.2.5). We use the Green function $G(x, x')^2$ which satisfies the inhomogeneous equation for a point source located at x' .

$$(\nabla^2 + \underline{k}^2)G(x, x') = -\delta(x - x')\tag{2.5}$$

$$\underline{k} = \frac{k}{\sqrt{1 + j\omega\kappa\left(\frac{4}{3}\mu + \mu_B\right)}}\tag{2.6}$$

Where \underline{k} is a complex wave number, $k = \omega c$ and the viscous properties of the fluid are represented by μ_B and μ , where μ_B is the bulk viscosity and μ is the shear viscosity and μ is equal to zero in this study.

² $G(x, x')$ represents the value of the function G at x for a source x' ,

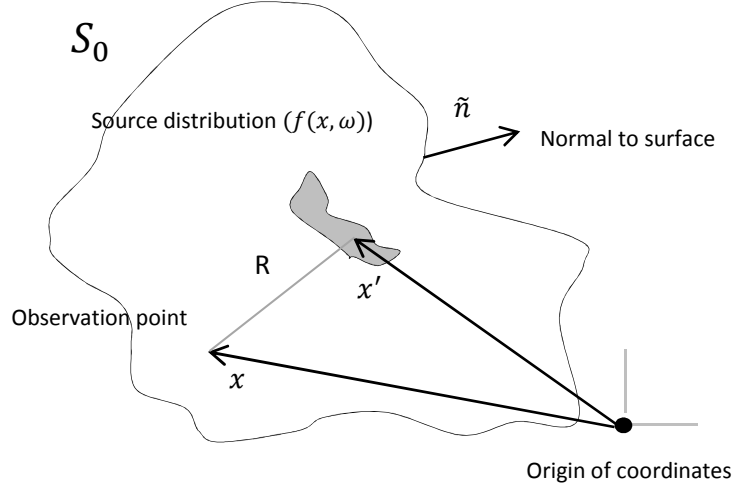


Fig.2. 5. Finding the velocity potential at x by applying the distributed source with angular frequency ω that is surrounded by a surface S_0 [59]

The $\delta(x - x')$ is the Dirac delta function, which is equal to zero for all x values except $x = x'$. The velocity potential of the whole source can be found by adding the velocity potential of each point source.

To get an integral for the velocity potential at point x which is located within S_0 , the equation 2.4 is multiplied by $G(x, x')$ and equation 2.5 is multiplied by $\Phi(x, \omega)$. Then by subtracting these two, we obtain: [59]

$$G(x, x')\nabla^2\Phi - \Phi\nabla^2G(x, x') = \Phi\delta(x - x') - G(x, x')f(x, \omega) \quad 2.7$$

First of all, the integration of equation 2.7 over the entire volume V_0 surrounded by S_0 should be calculated. The next step is applying Green's theorem in equation 2.7, which is the prime foundation of the scalar diffraction theory. If Φ and ψ defines arbitrary scalar fields, and the $\frac{\partial}{\partial n}$ is the derivative in outward normal direction on the S and V , then Green's Theorem is:

$$\int_V (\psi\nabla^2\Phi - \Phi\nabla^2\psi)dV = \oint_S (\psi\frac{\partial\Phi}{\partial n} - \Phi\frac{\partial\psi}{\partial n})dS \quad 2.8$$

Finally, noting that the volume integral of $\Phi \delta(x - x')$ is equal to $\Phi(x)$, we find:

$$\iint_{S_0} \left[G(x, x') \frac{\partial \Phi}{\partial n} - \Phi \frac{\partial G(x, x')}{\partial n} \right] dS_0 = \Phi(x) - \iiint_{V_0} G(x, x') f(x', \omega) dV_0 \quad 2.9$$

So the velocity potential is found by having the source distribution [7], and could be written as:

$$\Phi(x, \omega) = \iint_{S_0} \left[G(x, x') \frac{\partial \Phi}{\partial n} - \Phi \frac{\partial G(x, x')}{\partial n} \right] dS_0 + \iiint_{V_0} G(x, x') f(x', \omega) dV_0 \quad 2.10$$

2.3. Boundary conditions

Before explaining the specific aspects in these studies, which simplify the mathematical representation of boundary conditions, it is better to have a general rule, which is based in the scope of linear physics.

The boundary conditions in acoustics involve surfaces that reduce the propagation medium, such as free surfaces, or interfaces between two media with different physical properties. The boundary conditions are dependent upon the physical quantities associated to the acoustic field: displacements or particle velocity, fluctuations of pressure or stress and intensity [60].

2.3.1. Acoustic Impedance

When an ultrasonic wave encounters the interface between two media, the reflection and transmission rates are dependent on the ratio of the acoustic impedance of the two media. The acoustic impedance at a particular frequency indicates how much sound pressure is generated by a given air vibration at that frequency. The acoustic impedance (\mathbf{Z}) of a material is defined as the product of its density (ρ) and acoustic velocity (longitudinal wave velocity) (\mathbf{V}).

$$Z = \rho V$$

Applying the boundary conditions on the interfaces of two materials with different acoustic impedance allows us to determine the characteristics of the transmitted and reflected waves.

2.3.2. Reflection and transmission coefficients

Ultrasonic waves are reflected at boundaries where there is a difference in acoustic impedances (Z) of the materials on each side of the boundary. Distribution of energy between reflected and transmitted waves also depends on the amount of initial energy that the original waves possessed. The acoustic wave splits into two waves: a portion of the wave transmitting into the second medium and a portion of the wave reflecting back into the first medium. When the acoustic impedances of the materials on both sides of the boundary are known, the fraction of the incident wave intensity that is reflected and transmitted can be calculated.

The incidence of ultrasound waves modifies the direction of the waves and also the amplitudes when it meets the interfaces. By finding the reflection and transmission coefficients we can find the change of the amplitudes, and applying Snell's Law is a way to find the direction.

In the main part of my work, the transmission is assumed to occur at a liquid-solid interface. In this case, the longitudinal modes are the only ones that can be used.

2.3.2.1. Reflection at a liquid-solid interface

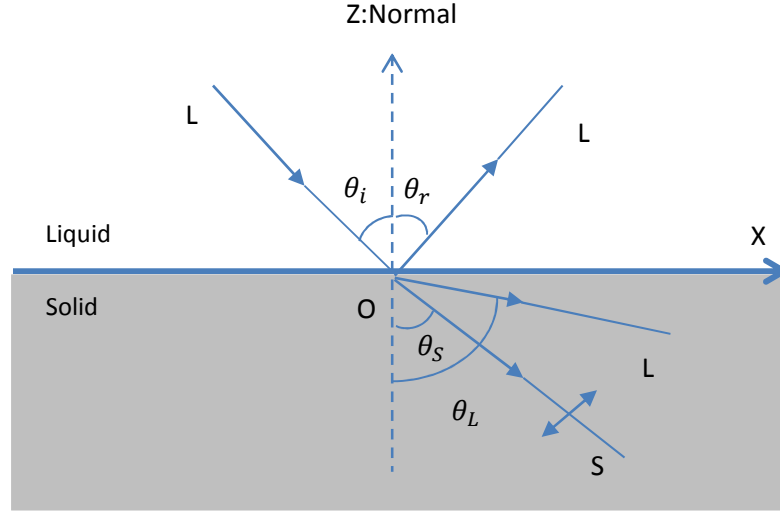


Fig.2. 6. Interaction of a oblique plane wave with a plane interface separating two different media

As we know the velocity potentials in liquid and solid could be shown, respectively as

$$\begin{aligned} \vec{v} &= \nabla\phi && \text{Liquid} \\ \vec{v} &= \nabla\phi + \vec{\nabla} \times \vec{\psi} && \text{Solid} \end{aligned} \quad 2.11$$

Since ϕ is a scalar potential for longitudinal mode and ψ is a vector potential for shear mode [2].

$$\begin{aligned} \phi_i &= \exp j(\omega t - k \sin\theta_i x + k \cos\theta_i z) \\ \phi_r &= R \exp j(\omega t - k \sin\theta_r x - k \cos\theta_r z) \\ \phi &= T_L \exp j(\omega t - k_L \sin\theta_L x + k_L \cos\theta_L z) \\ \psi &= T_S \exp j(\omega t - k_S \sin\theta_S x + k_S \cos\theta_S z) \end{aligned} \quad 2.12$$

The indices of L and S symbolize the longitudinal and shear waves, respectively.

k and k_L are longitudinal wave numbers in liquid and solid, respectively, and k_S represents the wave number of shear wave in the solid medium. R is a reflection coefficient and T_L and T_S are transmission coefficients.

Then the stress results and velocities should be introduced into the boundary conditions.

There are three boundary conditions for $z = 0$:

$$\begin{aligned}
 1) \ v_{z1} &= v_{z2} && \text{continuity normal velocities} \\
 2) \ P &= \sigma_{zz} && \text{continuity of normal stress} \\
 3) \ \sigma_{xz} &= 0 && \text{Tangential stress}
 \end{aligned}
 \tag{2.13}$$

Accepting the fact that $\theta_i = \theta_r$ leads to the set of equations that come from the boundary conditions:

$$\begin{aligned}
 Rk \cos \theta_i + T_L k_L \cos \theta_L - T_S k_S \sin \theta_S &= k \cos \theta_i \\
 k_L^2 \sin 2\theta_L T_L + k_S^2 \cos 2\theta_S T_S &= 0
 \end{aligned}
 \tag{2.14}$$

$$\rho_1 R + \rho_2 \left(2 \frac{k_L^2}{k_S^2} \sin^2 \theta_L - 1 \right) T_L + \rho_2 \sin 2\theta_S T_S = 0$$

Therefore, the reflection and transmission coefficients are computed to be

$$\begin{aligned}
 R &= \frac{Z_L \cos^2 2\theta_S + Z_S \sin^2 2\theta_S - Z_1}{Z_L \cos^2 2\theta_S + Z_S \sin^2 2\theta_S + Z_1} \\
 T_L &= \left(\frac{\rho_1}{\rho_2} \right) \frac{2Z_L \cos 2\theta_S - Z_1}{Z_L \cos^2 2\theta_S + Z_S \sin^2 2\theta_S + Z_1} \\
 T_S &= - \left(\frac{\rho_1}{\rho_2} \right) \frac{2Z_S \cos 2\theta_S - Z_1}{Z_L \cos^2 2\theta_S + Z_S \sin^2 2\theta_S + Z_1}
 \end{aligned}
 \tag{2.15}$$

Where

$$\boxed{
 \begin{aligned}
 Z_1 &= \frac{\rho_1 V_1}{\cos \theta_i} & Z_L &= \frac{\rho_2 V_L}{\cos \theta_L} & Z_S &= \frac{\rho_2 V_S}{\cos \theta_S}
 \end{aligned}
 }
 \tag{2.16}$$

These equations are considered in the next chapter in order to calculate the scattering field of reflectors [54].

2.3.3. Snell's Law

The most valuable application of Huygens' Principle is for describing the wave fronts created when a wave is incident on a flat interface between two media of different velocity. The *angle of incidence* θ_i , is defined as the angle between the incident ray and the normal to the interface. Following Huygens' Principle we consider that point O is the source of a new wave which begins propagating in the first medium with velocity V_1 and in the second medium with velocity V_2 .

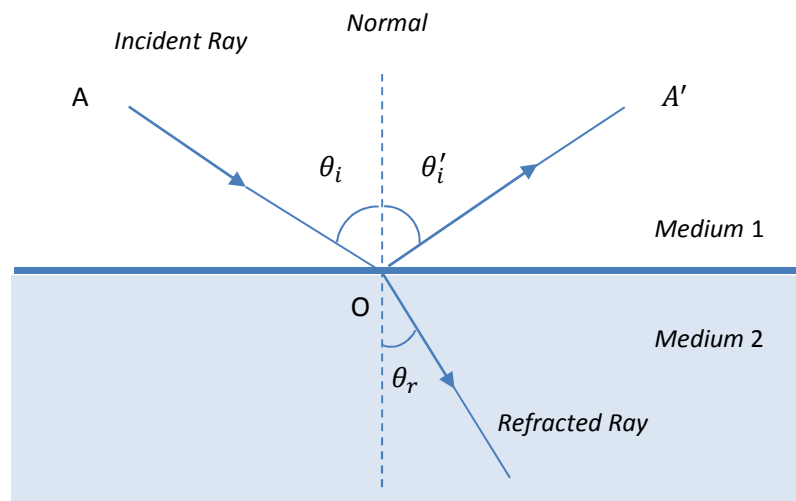


Fig.2. 7. Refraction of sound at the interface of two different media with different acoustical properties

From the above geometry it can be seen that:

$$\theta_i = \theta_i' \quad \mathbf{2.17}$$

For any reflected or refracted waves, Snell's law declares that the ratio of the sine of the angles of incidence and refraction is equal to the ratio of phase velocities in the two medium, or equal to the reverse ratio of the indices of refraction:

$$\frac{\sin\theta_i}{\sin\theta_r} = \frac{V_1}{V_2} = \frac{n_2}{n_1} \quad \mathbf{2.18}$$

Each θ as the angle measured from the normal, V as the velocity of sound in the respective medium and n as the refractive index.

2.4. Attenuation in an acoustical field

It is well known that sound energy diminishes with distance traveled. Attenuation is the decrease of sound intensity with distance. In materials, sound pressure (signal amplitude) is reduced by the wave's propagation; there are other factors which also cause the sound pressure to weaken. This further weakening results from scattering and absorption. The reflection of the sound in directions other than its initial direction of distribution is defined as scattering, and absorption is the transformation of the sound energy to other forms of energy like heat. If a harmonic wave propagates in a medium with low viscosity the complex wave number equation 2.6 can be presented in a new form with good approximation: [61]

$$\underline{k} \approx k \left[1 - \frac{j\omega\kappa}{2} \left(\frac{4}{3}\mu + \mu_B \right) \right] = k - j\alpha \quad 2.19$$

Where $\alpha = \frac{\omega^2}{2\rho_0 c_0^3} \left(\frac{4}{3}\mu + \mu_B \right)$ is the attenuation coefficient.

Thus, for the plane harmonic wave that propagated in the x direction the velocity potential can be described as:

$$\Phi(x, t) = \Phi_0 e^{-\alpha x} \exp[j(\omega t - kx)] \quad 2.20$$

The attenuation coefficient can also be introduced in terms of intensity or pressure and usually described in dB/cm as:

$$\alpha_{dB} = \frac{10}{x} \log\left(\frac{I(0)}{I(x)}\right) \quad 2.21$$

Where the incident intensity at $x=0$ is $I(0)$ and $I(x)$ is the intensity at a location x .

The units of the attenuation value in decibels per centimeter can be converted to Neper per centimeter [61].

$$\begin{aligned}\alpha_{dB} &= 8.686 \alpha_{Np} \\ \alpha_{Np} &= 0.1151 \alpha_{dB}\end{aligned}\tag{2.22}$$

Chapter3: SIMULATION

3.1. Description of the numerical experiment

As previously stated, this project focuses on using ultrasound to reconstruct images of foreign objects (with different acoustical properties compare to the brain tissue), which have entered into brain. The Harmonic Phase Conjugation technique ([5-8], [20-30]) presented in this thesis has several unique advantages over several other proposed solutions to the above problem.

The specific goal of this work is to develop an algorithm for checking the accuracy of reconstruction of reflecting objects using the ultrasonic phase-conjugated harmonic imaging technique, both numerically and experimentally.

This chapter presents the results of computer simulation and their interpretation based on the theory summarized in chapter 2. As with any simulation, certain model approximations were assumed to simplify numerical calculations.

This chapter begins with a brief description of the experimental system and the explanation of the underlying assumptions. The differences between the simulated and experimental setup are also explained.

The computer simulation developed for this project was done in the MATLAB 7.5 programming environment. The two general states of field calculation mode and back propagation mode to reconstruct the images are considered and main portions of the source code have been attached at the end of the thesis (see Appendix A).

Fig.3.1 shows the general setup in the *field calculation mode*. The transducer on the left (from now on referred to as the source) is driven by a continuous harmonic signal (CW) and generates an acoustic wave propagating from left to right in the water. The directivity pattern of the resulting ultrasound beam is determined by the geometry of the source transducer. This pattern may be altered due to interaction with the scattering objects

(shown as red ellipses) distributed along the propagation path. In addition, the acoustic wave experiences regular attenuation by the water. The resulting acoustic field is received by the 128-element transducer array on the right (see Figure 3.1).

In the linear approximation, the total field received by each array element can be calculated as a superposition of the source (direct) and scattered components. Calculation of the intensity and phase distribution of such a final field on the array of receivers is the first essential step of the numerical experiment.

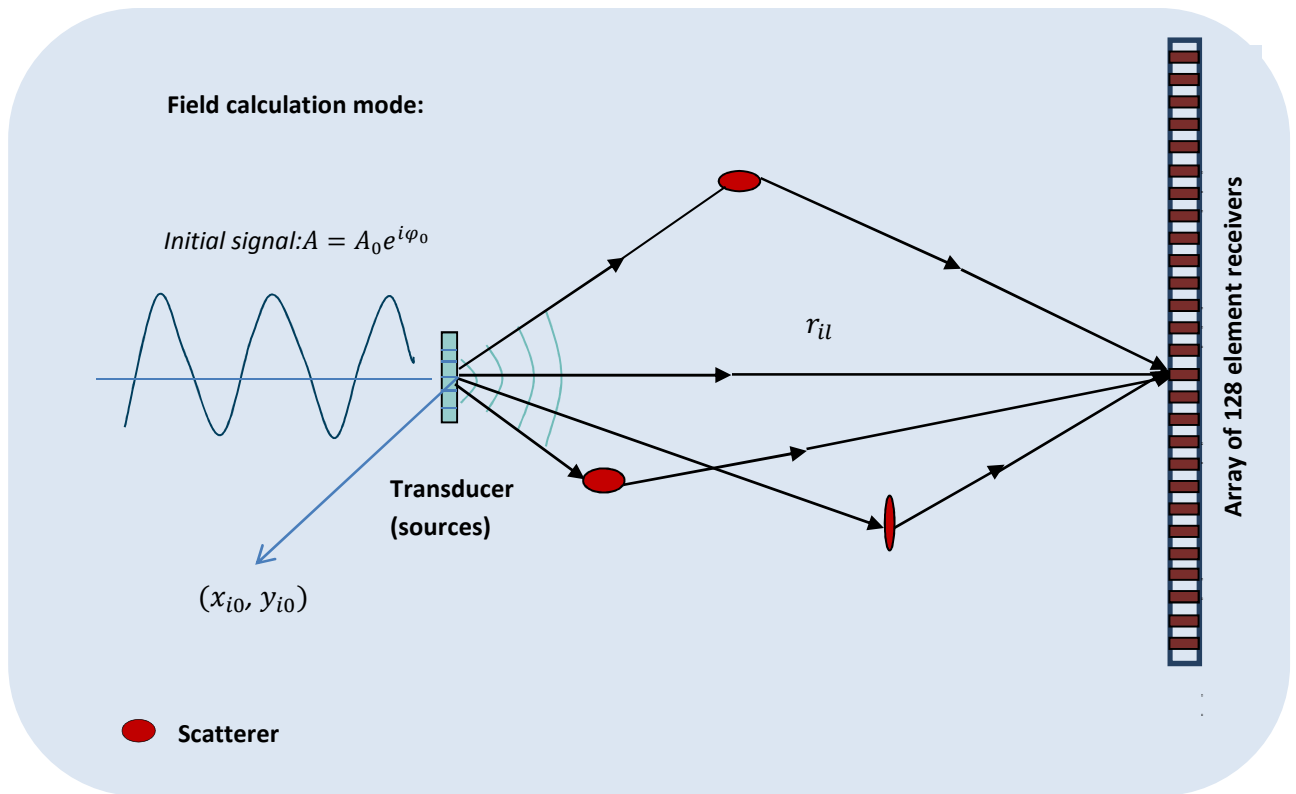


Fig.3. 1. Description of the model used in the numerical experiment (in absence of scattering layer) From Left to right: Extended source, scatterers, and the array of receivers. (x_{i_0}, y_{i_0}) is the coordinate of i^{th} element of the extended source, r_{il} is the distance from the i^{th} point source of the extended source to the l^{th} receiver element

In general, the simulated experimental setup (Figure 3.1) is defined by the following essential components:

Source: The source definition can be different for different numerical experiments. In this study it is simulated either as a point source or as a combination of point sources (called an “extended source”). Each point source is $\lambda/10=0.074$ mm in size (2 MHz frequency is assumed). The source field is defined by specifying the initial phase and amplitude of originating spherical wave.

Scatterers: Acoustic scattering arises from objects with physical dimensions close to or smaller than the acoustic wavelength in water. An object or interface of this size with different acoustic impedance (than water) is often called scatterer. Some scatterers are defined in the simulation as foreign objects that each acts as a new separate sound source and scatters the sound field in all directions independent of the direction of the arriving incident wave. Due to their differing sizes, scattering could be different. Each scatterer was modeled as a combination of point scatterers, and the scatterer can be considered a point only when its size is smaller the wave length. The maximum sizes of the scatterers are compatible with the wavelength and smaller. (i.e. scatterer combined of 9×9 points with size of $[\approx 0.50 \text{ mm}^2]$).

Array of receivers: The array of receivers consists of 128 small elements. The size of each element is $\lambda/2=0.37\text{mm}$, where λ is the acoustic wavelength in water at 2 MHz frequency assumed in the experiment. For all beams originating from the partial point sources, the phases and amplitudes of the direct and scattered field are saved at the locations of each element of the receiving array.

Scattering layer of skull bone: As explained in chapter 1, the real skull consists of three different layers: outer table, diploe and inner table (Figure 1.14). It was also indicated that in this study a simplified skull model was used. In particular, the skull was simulated as a number of single-layer segments of different (random) thickness stacked side by side. In developing this model the random phase shifting element technique was used. Due to its random thickness, each segment introduced a random phase shift between $[0-2\pi]$ to any transmitted beam. This phase shifting was simulated in terms of additional real and imaginary components to any beam transmitted through the specific segment of this

model. It should be noted that during each run of the whole simulation, the phase shifting values are chosen randomly but remain the same till the final image is generated. The amount of phase shift in each segment was proportional to the length of the propagation path of the particular beam in that segment.

Accordingly, due to changing the phase and amplitude, the transmitting field distorted by passing through each segment with constant thickness. The number of segments depends on the desired smoothness of the lower boundary of the skull. Additionally, each random additive value is in correlation with attenuation (α) and thickness (d) of each segment, so besides the phase shifting any transmitted beam was damped due to attenuation of this scattering model. A complex model of skull is going to be used in the future (Fig.3.2).

$$p = p_0 e^{-\alpha d} e^{ik_2 d} \quad k_2 = \text{wavenumber in the layer}$$



Fig.3. 2. Schematic scattering layer with random phase shifting technique. Each section has random phase shift ($0-2\pi$) and the number of section could vary due to shape of the lower boundary

The dimensions and acoustical properties of all system components can be found in Tables 3.1 and 3.2.

Medium	Velocity of Longitudinal Wave (m/s)	Attenuation coefficient(Np/m)
<i>Water</i>	1500	20.72
<i>Simplified skull layer</i>	3000	184.20

Table.3. 1. The acoustic properties of the scattering layer and water

	<i>Size of Element</i>	<i>Total Length</i>
<i>Extended Source</i>	$\lambda/10 = 0.074 \text{ mm}$	$50 \lambda/10 = 3.70 \text{ mm}$
<i>Reflectors object</i>	$\lambda/10 = 0.074 \text{ mm}$	<div style="border: 1px dashed black; padding: 2px;"> Reflector1: $9 \lambda/10 \times 9 \lambda/10$ Reflector2: $7 \lambda/10 \times 7 \lambda/10$ Reflector3: $9 \lambda/10 \times 9 \lambda/10$ </div>
<i>Simplified skull layer</i>	-----	$128 \lambda/2 = 47.36 \text{ mm}$
<i>Array of Receivers</i>	$\lambda/2 = 0.37 \text{ mm}$	$128 \lambda/2 = 47.36 \text{ mm}$

Table.3. 2. The dimensions of the main components of the simulated system

3.2. Forward propagation step: calculating phase and amplitude distributions

The first essential step of the simulated experiment is calculating the distribution of the phase and amplitude of the ultrasound field on the array of receivers. In the beginning, the numerical model started with a simple combination of a source and a receiving array. As the next level of complexity, reflectors were added between the source and the array. Finally, the skull layer was added. This evolution of the model is discussed in detail in the following subsections.

3.2.1. Case (a): Unobstructed acoustic field from various sources

As the simplest case, the field from a single point source placed on the axis of symmetry of the receiving array is calculated. The point source was placed at the point (64,100) relative to the center of the array in the x direction ($x_0 = \frac{64\lambda}{2} = 23.68\text{mm}$) and to the distance ($y_0 = \frac{100\lambda}{2} = 37.00\text{mm}$) from the array. This point source emitted the harmonic signal at frequency $f = 2 \text{ MHz}$. The signal was received by the linear array of

128 single elements and separated by $\lambda/2$. The simulation result shows a strong peak at the location of the source, as expected (Figure 3.3.a).

Next, the field from multiple point sources placed along a straight line and separated by $\lambda/10$ was calculated. Each point of the resulting extended source emitted the signal, and each element of the receiving array recorded the superposition of all these signals. The ultrasound pressure field on the array could be determined from the following equation [61]:

$$P_{array}(x_l) = \sum_{i=1}^S \left(\frac{P_i(x_{i0}, y_{i0})}{r_{il}} e^{j(k_1 r_{il} + \varphi_{i0})} e^{-\alpha_w r_{il}} \right) \quad 3.1$$

Where $k_1 = \frac{2\pi}{\lambda}$ is the wave number and $\lambda = \frac{c_1}{f} = 0.75mm$ is the wavelength, $f = 2 MHz$ is the frequency of the signal and $c_1 = 1500 m/s$ is the velocity of sound in water. S is the number of point sources in the extended source (up to 50 in the simulation), α_w is the attenuation factor of ultrasound in water; (x_{i0}, y_{i0}) is the coordinate of i^{th} element in the extended source (Fig.3.1), r_{il} is the distance from the i^{th} point source of the extended source to l^{th} receiver element on the array and calculated as follows:

$$r_{il} = \sqrt{(x_l - x_{i0})^2 + (y_l - y_{i0})^2} \quad 3.2$$

Where x_l, y_l are the coordinates of the l^{th} element of the array. Since only a linear array was involved, it was assumed that all $y_l = 0$. In order to calculate the amplitude and phase distribution on the array, equation 3.1 was split into real and imaginary parts by applying trigonometric functions as follows:

$$P_{array}(x_l) = \sum_{i=1}^S \left(\frac{P_i(x_{i0}, y_{i0})}{r_{il}} e^{-\alpha_w r_{il}} [\cos(k_1 r_{il} + \varphi_{i0}) + j \sin(k_1 r_{il} + \varphi_{i0})] \right)$$

$$Real_Source(x_l) = \sum_{i=1}^S \frac{e^{-\alpha_w r_{il}}}{r_{il}} (R_0 \cos(k_1 r_{il}) - I_0 \sin(k_1 r_{il})) \quad 3.3$$

$$Imaginary_Source(x_l) = \sum_{i=1}^S \frac{e^{-\alpha_w r_{il}}}{r_{il}} (R_0 \sin(k_1 r_{il}) + I_0 \cos(k_1 r_{il}))$$

Where R_0 and I_0 are defined as:

$$R_0 = P_i(x_{i0}, y_{i0}) \cos(\varphi_{i0})$$

3.4

$$I_0 = P_i(x_{i0}, y_{i0}) \sin(\varphi_{i0})$$

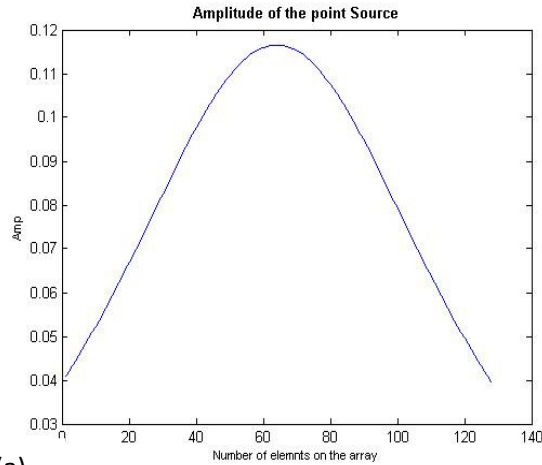
Therefore, by using equation 3.3 the amplitude and phase can be written as

$$amplitude_source = \sqrt{(Real_Source(x_i))^2 + (Imaginary_Source(x_i))^2}$$

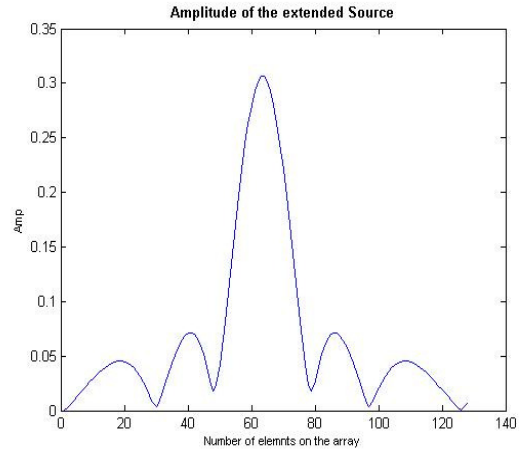
3.5

$$Phase_source = \text{Arctan}\left(\frac{Imaginary_Source(x_i)}{Real_Source(x_i)}\right)$$

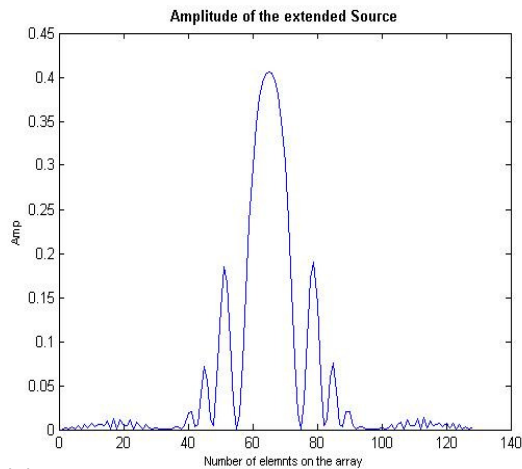
The simulation results for the point source and several extended sources are shown in (Fig.3.3). This figure shows the simulated amplitude of received ultrasound field. (a) is distribution of one point source which was located at the center of the array in x direction, $x_{i0} = \frac{64\lambda}{2} = 23.68$ mm and at the distance $y_{i0} = \frac{100\lambda}{2} = 37.00$ mm from the array. Images (b)-(d) represent extended sources that were all placed at the distance $y_{i0} = \frac{100\lambda}{2} = 37.00$ mm from the array, but contained different numbers of point sources separated by $\lambda/10=0.074$ mm. (b) is distribution from 6 point sources that were located at $x_{i0} = \frac{61\lambda}{10}$ to $\frac{67\lambda}{10}$, (c) shows field distribution of 20 point sources were placed at $x_{i0} = \frac{54\lambda}{10}$ to $\frac{74\lambda}{10}$ and finally, (d) represents field distribution of 50 point sources were put at $x_{i0} = \frac{39\lambda}{10}$ to $\frac{89\lambda}{10}$.



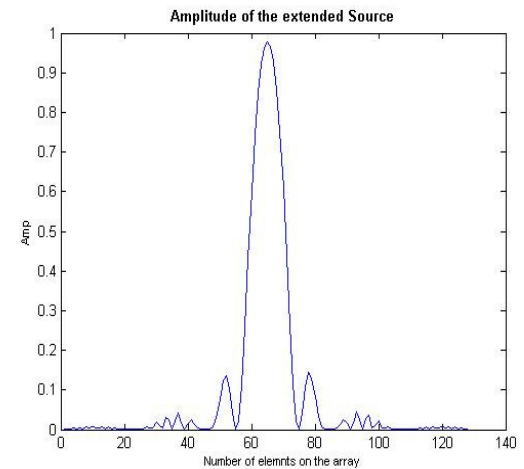
(a)



(b)



(c)



(d)

Fig.3.3. Simulated amplitude of received ultrasound field from source (a) One point source, (b)-(d) represent extended sources (b) 6 point sources (c) 20 point sources (d) 50 point sources

As mentioned earlier, extension of the image reconstruction algorithms for the case of 2D arrays could be a part of the plan for future work. For this purpose, the phase and amplitude distributions were calculated on a matrix array of 128×128 elements pitched at $\lambda/2$ using the above approach. The extended source was composed of 6 point sources. Fig.3.4 shows the intensity and phase distribution of the ultrasound field on the 2D array. In this figure (a) represents intensity distribution of 6 point sources at the $x_{i0} = \frac{61\lambda}{10}$ to $\frac{67\lambda}{10}$ and $y_{i0} = \frac{64\lambda}{2} = 23.68\text{mm}$ with distance $z_{i0} = \frac{45\lambda}{2} = 16.65\text{mm}$ from the 2D array, and (b) is phase distribution of the source on 2D array.

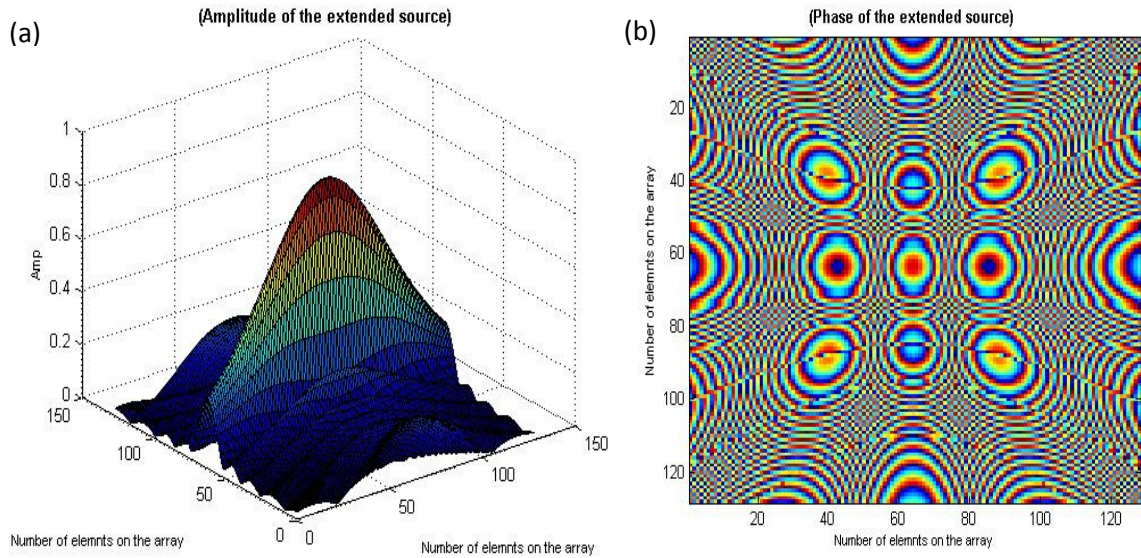


Fig.3.4. Simulated intensity and phase distribution of the ultrasound field on a 2D receiving array. (a) Intensity distribution of source. (b) Phase distribution of source on 2D array.

3.2.2. Case (b): Acoustic field in presence of scattering objects

As mentioned before, the goal of this study is to locate the position of scatterers. Therefore, in this case, a scatterer was added to the previous numerical model and it was located between extended acoustic source and the receiving linear array. This scatterer was assumed as a point target to be square with 0.37 mm wide and high. It was placed at depth $y_r = \frac{30\lambda}{2} = 11.10$ mm from the surface of the array and $x_r = \frac{50\lambda}{2} = 18.50$ mm away from the array axis corresponding to the coordinate $Reflector_1 = (50, 30)$. The size and position of scatterer could be changed, as shown in (Fig.3.5). The transmitted field by the point source through the scatterer was then recorded on the 128 elements on the array.

In this part, the beams that reached the array of receiver's elements were the superposition of straight paths from the source and broken paths from the scatterer.

Here, r_{ir} and r_{rl} are the paths from the source to scatterers and from the scatterer to the array, defined as

$$\begin{aligned} r_{ir} &= \sqrt{(x_r - x_{i0})^2 + (y_r - y_{i0})^2} \\ r_{rl} &= \sqrt{(x_l - x_r)^2 + (y_l - y_r)^2} \\ R_{il,r} &= r_{ir} + r_{rl} \end{aligned} \quad 3.6$$

where $R_{il,r}$ is the broken path from the i^{th} point source of the extended source to r^{th} point of reflector to the l^{th} receiver element on the array. Straightforward mathematical rearrangements allow the implementation of the above equation into equation 3.3, 3.4 and 3.5. For calculation of the amplitude and phase distributions on the array. Of course, such calculated values will contain direct and refracted/reflected paths from source elements and scatterers respectively.

The resulting signals for different positions of the scatterer (no source information) are shown in (Fig.3.5)

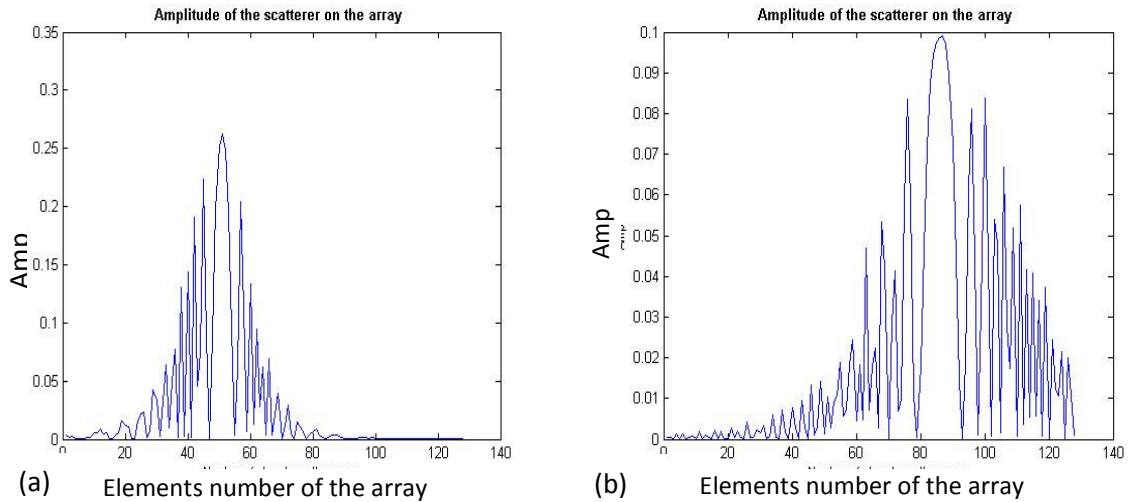


Fig.3. 5. Simulated amplitude of received acoustic field of the scatterer on the array. (a) The scatterer that located at the coordinate $r_1 = (55, 30)$. (b) the scatterer located at the coordinate $r_2 = (85, 50)$

3.2.3. Case(c): Acoustic field in presence of scattering objects and a scattering layer

The next step in simulation was accomplished by adding the scattering layer. The acoustical and geometrical properties of such a simulated layer were explained in previous sections. The scattering layer was placed between the receiving array and the reflectors in the medium (the source was located before the reflectors as shown in (Fig.3.6)). As stated before, adding the scattering layer, introduced random phase shifts to the transmitted beams. Additional attenuation due to changed traveling paths in the water and the layer was also incorporated in the model.

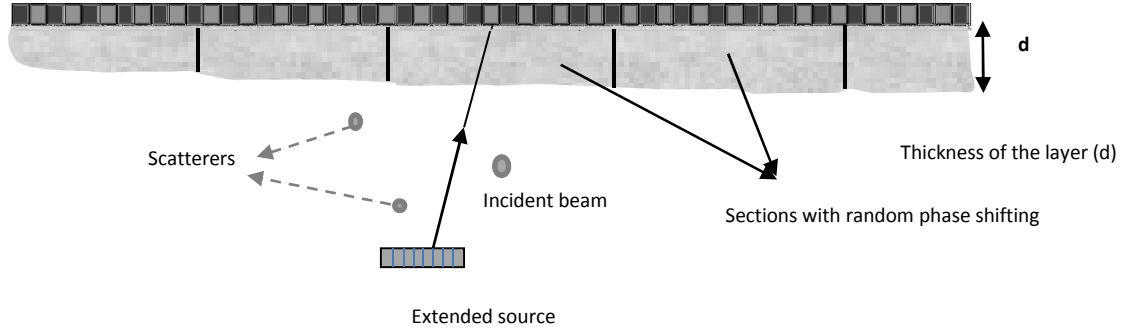


Fig.3. 6. Transmitting of ultrasound beam through scattering layer with random phase shifting technique.

The ultrasonic field pressure can be calculated in the same way as equation 3.1, except in this case an additional phase shift due to the layer was applied to the equation. After rearranging the equation 3.1 (no scattering layer) and using the random phase shifting technique the field distribution can be expressed as:

$$P_{array}(x_l) = \sum_{i=1}^S \left(\frac{P_i(x_{i0}, y_{i0})}{(r_{il,1} + r_{il,2})} \exp[j((k_1 r_{il,1} + k_2 r_{il,2}) + \varphi_i + \varphi_{layer}) - (\alpha_w r_{il,1} + \alpha_{layer} r_{il,2})] \right) \quad 3.7$$

Where S is the number of point sources in the extended source, $r_{il,1}$ and $r_{il,2}$ are the path taken in water and the scattering layer, respectively, α_{layer} is the attenuation coefficient

of the scattering layer and α_w is the attenuation coefficient of water (Table 3.1). Here, φ_i and φ_{layer} are the initial phase of the beam and phase shift through the layer, respectively.

As explained before, the scattering layer introduced some phase shift (φ_{layer}) to the exponential part of the ultrasound field pressure equation that can be defined in real and imaginary parts as follows,

$$Real_layer = e^{-\alpha_{layer}*d} \cos(k_2d)$$

3.8

$$Imaginay_layer = e^{-\alpha_{layer}*d} \sin(k_2d)$$

Where, $k_2 = \frac{c_2}{\lambda_2}$ and d is the thickness of the scattering layer, which is variable. In presence of scattering layer, before computing the amplitude and phase distribution on the array, the term 3.8 was added to the real and imaginary parts of equation 3.4 and the process was continued as before. The coordinate of the scatterer is the same as in Fig.3.5 and the results of using phase shifting technique on the scatterer with applying the equation 3.5 are presented in Fig.3.7. It can be seen that the scatterer field distribution was distorted and the amplitude of the scatterer got damped resulting from the attenuation of the scatterer layer. In addition, the maxima of both plots shifted a little bit due to the difference of sound speed in the scattering layer and water.

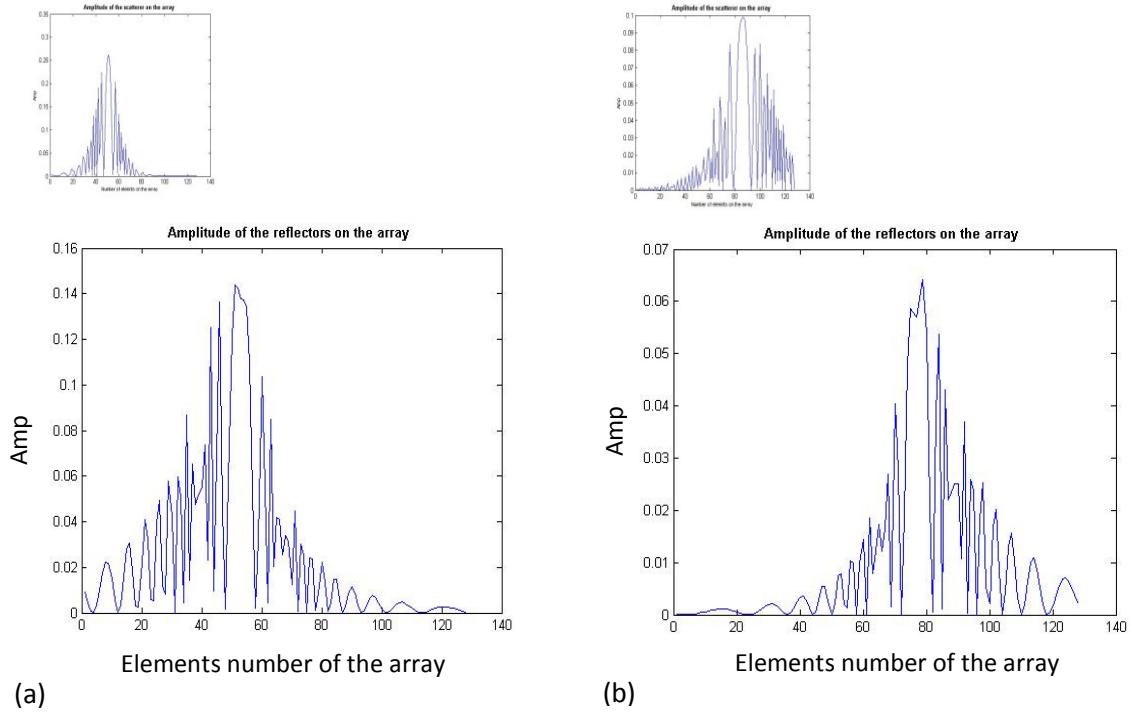


Fig.3.7. Simulated amplitude of the acoustic field in the presence of scattering object and a scattering layer. The small figures show the results without the layer. (a) Square 0.37 mm scatterer located at $r_1 = (55, 30)$. (b) Square 0.52 mm scatterer located at $r_2 = (85, 50)$

3.3 Back-propagation step: image reconstruction via Harmonic Phase Conjugation method

The next main part of the simulation is the *back propagation step* meant to reconstruct an image of the reflectors position. To conduct this part, the saved acoustic field information on the array should be used by the program to produce a back-propagating field (Fig.3.8), which, after passing through the layer will focus on the scattering objects, thus producing their image.



Fig.3. 8. Schematic figure of the back propagation mode with presence of skull layer

Following the previously explained theory and calculation of the field pattern for the above mentioned major cases, the image reconstruction process is now to be explained:

As stated earlier, the final superimposed amplitude and phase of the received beams were recorded on each element of the array. Subsequently, the phase conjugation technique as the second major part of the simulation was coded and applied to reconstruct the final image showing the location of the scatterers. The recorded signals were phase conjugated and retransmitted. In this situation it was supposed that each receiver starts to generate its own field (like a point source) in the reverse direction with its initial phase and amplitude. So the array acted as an extended source composed of 128 point sources that emitted the acoustical pressure field in opposite direction (Fig.3.8). A superposition of all transmitted signals from the array were computed and saved at grid of the simulated image plane which is the virtual plane in front of the array including the array line itself. This plane was simulated with 128×300 grids (each $\lambda/2$ in size). The prediction was that the superposition of reversed waves display major intensity peaks at the original location of the extended source or reflectors. More explanation and final results for each major case in image reconstruction are presented below:

3.3.1: Case (a) in back propagation mode

The source's field distribution on the array was calculated in subsection 3.2.1 (Case-A). In back propagation mode, reconstruction of the phase conjugated acoustic field was accomplished by rearranging the equation 3.1 for propagation in the reversed direction from array elements with initial phase and amplitudes saved after forward propagation step. The reconstructed field was recorded in the image plane containing 128 by 300 discrete points. Mathematical representation can be given by [61]:

$$P_{image}(X, Y) = \sum_{a=1}^A \frac{P_{array}(x_a, y_a)}{R_a} e^{j(-kR_a - \varphi_{0a})} e^{+\alpha_w R_a} \quad 3.9$$

Where P_{array} and φ_{0a} represent the initial amplitude and phase respectively of each element of the array (new sources in this mode) deployed in back propagation mode. They are the saved amplitude and phase of the a^{th} element of the array in the forward propagation mode. In addition, the coordinate of the a^{th} receiving element on the array is shows as (x_a, y_a) , and (X, Y) is allocated the point that the back propagated field was computed on the simulated image screen. A is the number of the elements in the array, equal to 128. R_a is the distance of each element of the array from each grid on the image screen and was calculated as follows

$$R_a = \sqrt{(X - x_a)^2 + (Y - y_a)^2} \quad 3.10$$

As in the forward propagation mode, equation 3.9 was split into the real and imaginary parts, and then the discrete form of the reconstructed field was used to obtain the final image.

$$\begin{aligned} Real_b_Source(x_l) &= \sum_{a=1}^A [(UR \cos(-k_1 R_a) - UI \sin(-k_1 R_a))] \\ Imaginary_b_Source(x_l) &= \sum_{a=1}^A [(UR \sin(-k_1 R_a) + UI \cos(-k_1 R_a))] \end{aligned} \quad 3.11$$

In equation 3.11 *Real_b_Source* and *Imaginary_b_Source* represents the real and imaginary parts of the reconstructed field, where *UR* and *UI* respectively are the summation of real part and imaginary part of the extended source field distribution, which were saved on each element of the receiver array. In fact, *UR* and *UI* are the discrete forms of the saved field distribution in forward propagation. By implementation of the above equation into equation 3.3, 3.4 and 3.5 the reconstructed field was calculated.

Following the same logic, the back propagation mode was also developed for the remaining two cases (sections 3.2.2 and 3.2.3).

Reconstruction results of the acoustic field of a point source and extended source by using the phase conjugated field distribution of the array are shown in Fig.3.9. The process began by reconstructing an image of the point source image (a) that was initially located at the coordinates (64, 100) and then continued by reconstructing of the extended sources containing different numbers of the point sources. The original distance of these extended sources from the surface of the array was $y_{i0} = 100\lambda/2 = 37.00 \text{ mm}$ and their original locations from the array axis were as follow: (b) 6 point sources : $x_{i0} = \frac{61\lambda}{10}$ to $\frac{67\lambda}{10}$ (c) 20 point sources: $x_{i0} = \frac{54\lambda}{10}$ to $\frac{74\lambda}{10}$ and (d) 50 point sources: $x_{i0} = \frac{39\lambda}{10}$ to $\frac{89\lambda}{10}$.

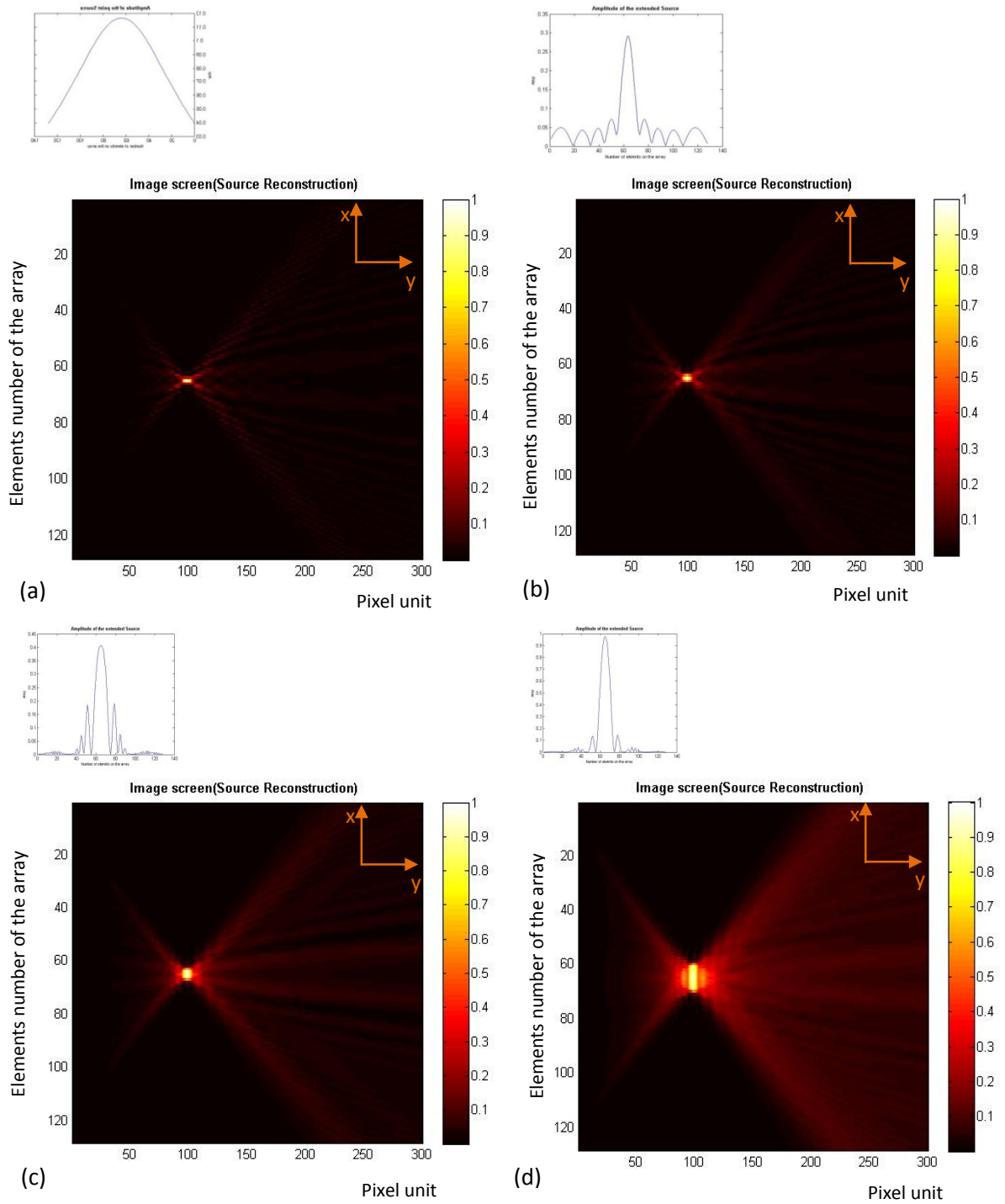


Fig.3. 9. Reconstruction of the phase conjugated field of the source and extended source using the same saved amplitude (small picture in each part). (a) Reconstruction image of 1 point source. (b),(c)and (d) represent reconstruction images of the extended source: (b) 6 point sources . (c) 20 point sources (d) 50 point sources.

There are some other results of reconstructed images of the extended source that were simulated by changing the source distance from the array. However, the extended sources (50 point sources) were still placed at the center of the array at $x_{i0} = \frac{64\lambda}{2} = 23.68 \text{ mm}$ with different distances from the array in each image. These distances were as follows: In (a) $y_{i0} = \frac{50\lambda}{2} = 18.50 \text{ mm}$, (b) $y_{i0} = \frac{100\lambda}{2} = 37.00 \text{ mm}$, (c) $y_{i0} = \frac{200\lambda}{2} = 74.00 \text{ mm}$ and (d) $y_{i0} = \frac{300\lambda}{2} = 111.00 \text{ mm}$. These results are shown in Fig.3.10.

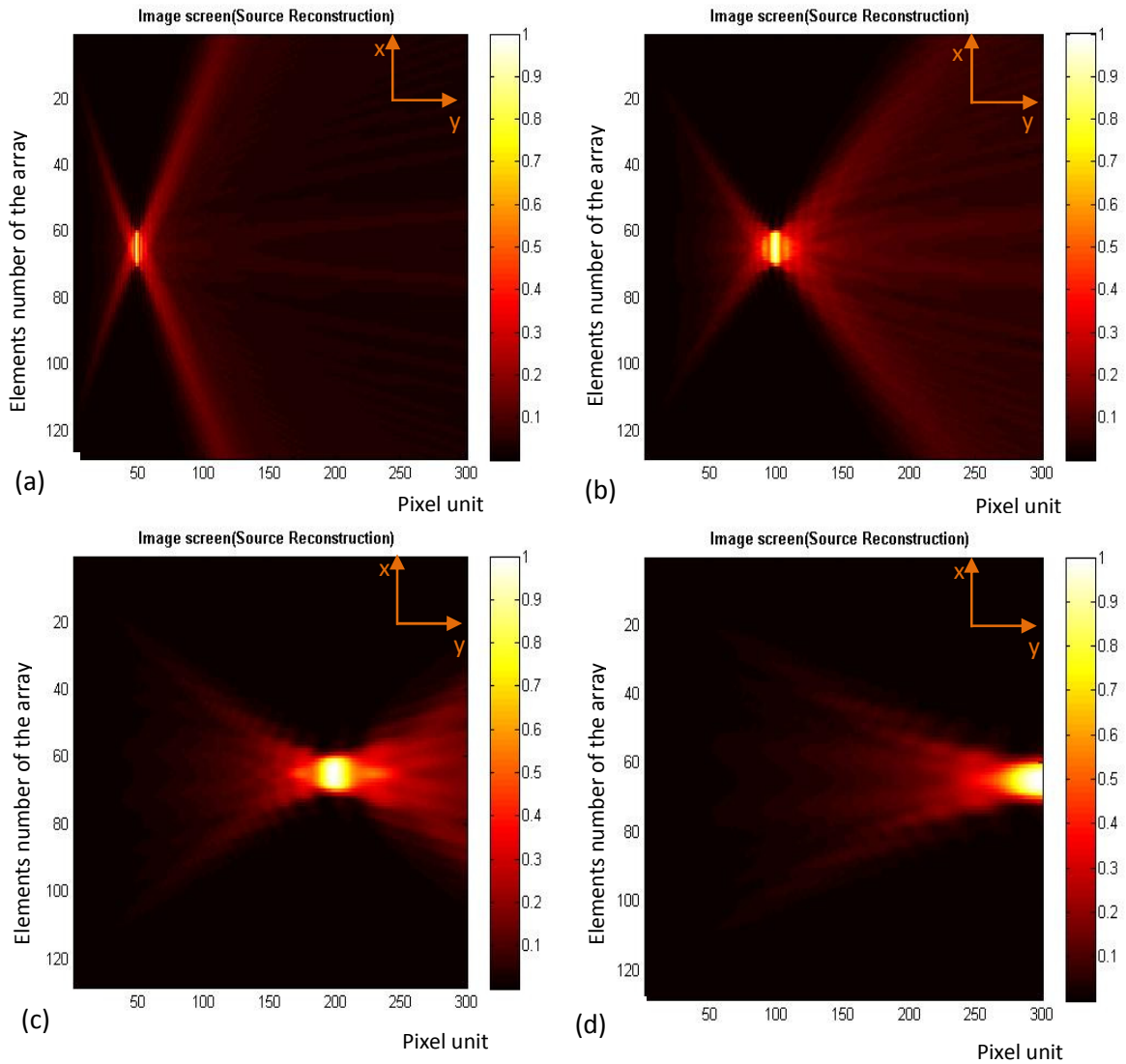


Fig.3. 10. Reconstructed image of the extended source combined 50 point sources in different distances from the array. The original distance of the source from the array was: (a) 18.50mm. (b) 37.00mm. (c) 74.00mm. (d) 111.00mm.

It can be seen in Fig.3.10 that the resolution of the images decreases when the distance increases.

Changing of the resolution can be interpreted by changing the elements' size resolution that occurred in y direction. The definition of the lateral resolution can be written as

$$dy' = \frac{\lambda y}{D} \quad 3.11$$

Where D is the length of the array and y is the distance between the array and the resolution element in the image plane. Larger dy' means decreased resolution of the final image. For fixed values of λ and D the lateral image resolution decreases proportionally to the distance from the array. According to Fig.3.10 when $y = \frac{50\lambda}{2}$ and $D = \frac{128\lambda}{2}$ then $dy' = 0.39\lambda$ and when $y = \frac{100\lambda}{2}$ with the same array length, $dy' = 0.78\lambda$.

3.3.2: Case (b) in back propagation mode

As explained before (chapter 1), reconstructing an image of the scatterer acting as an external object in the medium is the main goal of this project. In previous sections, the results of amplitude distribution of scatterer that was placed between the acoustic source and the array of receivers were presented. Fig.3.1 shows the field calculation mode process in presence of the scatterers. Recorded signals on each element of the receiving array are a superposition of all received acoustic fields (direct from the source and scattered). Therefore, to reconstruct the image of the scatterer, the source distribution on the array was eliminated from the total recorded field distribution. Since the source distribution is dominant in the final distribution, by its elimination, only the scattered field remains, and reconstructed images of the scatterers could be analysed clearly. Otherwise, by interference of the dominant source distribution and weak scatterer's distribution in back propagation mode, the scatterer's initial positions won't reveal. After this elimination, the reconstruction process continued in the same way as an extended source to reconstruct the images of scatterers.

$$Real_b_Scatterer(x_l) = \sum_{a=1}^A [(UR_s \cos(-k_1 R_a) - UI_s \sin(-k_1 R_a))] \quad 3.13$$

$$Imaginary_b_Scatterer(x_l) = \sum_{a=1}^A [(UR_s \sin(-k_1 R_a) + UI_s \cos(-k_1 R_a))]$$

The illustration for equation 3.13 is the same as equation 3.11. *Real_b_Scatterer* and *Imaginary_b_Scatterer* are the discrete form (real and imaginary, respectively) of the reconstructed field of the scatterers, and UR_s and UI_s are the real and imaginary parts of the scatterer field distribution which were saved on the array of receiver in the forward propagation mode, with the source information already removed.

The image reconstruction of the scatterers was conducted in different conditions and their simulation results are shown in Fig.3.11 - Fig.3.15. In order to show the initial location of the source, the schematic single transducer was placed in these figures. The arrangements of these results start in Fig.3.11, which represents the reconstructed images of different numbers of the scatterers of different size (Table.3.2). In this figure the results start with the reconstructed image of reflector1 in (a) at $X_1 = \frac{45\lambda}{2} = 16.87\text{mm}$ and $Y_1 = \frac{40\lambda}{2} = 14.80\text{mm}$. In image (b) reflector2 was added at $X_2 = \frac{75\lambda}{2} = 27.75\text{mm}$ and $Y_2 = \frac{40\lambda}{2} = 14.80\text{mm}$. In image (c) numbers of scatterers were extended to three. The first two scatterers were fixed at their coordinates and the third was placed at $X_3 = \frac{55\lambda}{2} = 20.62\text{mm}$ and $Y_3 = \frac{25\lambda}{2} = 9.37\text{mm}$, and finally (d) shows the reconstructed image of four scatterers that the last one was added at $X_4 = \frac{70\lambda}{2} = 25.90\text{mm}$ and $Y_4 = \frac{30\lambda}{2} = 11.10\text{mm}$.

Next results were conducted by changing the extended source distance from the array (Fig.3.12). The extended source was a combination of 50 point sources (each $\frac{\lambda}{10}$ in size). The initial locations of the scatterers were the same as part(c) in (Fig.3.11). Their coordinates were: Reflector1 = (45, 40), Reflector 2 = (75, 40), Reflector3 = (55, 25), but the source distance was gradually increased in each part of Fig.3.12. The source distance “D” was 18.50mm in (a), 37.00mm in (b), 74.00mm in (c) and 111.00mm in (d).

Following the same arrangement, the results of scatterers reconstruction imaged by changing the source's size was simulated (Fig.3.13). In the first image, the extended source was contained in 20 point sources with the length "L" equal to 1.48mm. By increasing the point source to 40, the length of the extended source reached to 2.96 mm. The next image(c) shows the 60 point source with a length of 3.70 mm, and finally the 90 point source with length of 6.66mm.

The next Image represented the image reconstruction of the scatterers in different positions (Fig.3.14). The extended source was defined as 50 point sources with $\frac{\lambda}{10}$ length of each point and it was located at coordinate (64,100). Each image consisted of the reconstructed image of three scatterers (reflectors) with different initial locations. The coordinates of the reflector1, reflector2 and reflector3 in each image were as follows, respectively:

Image (a): Reflector1 = (80,70) , Reflector2 = (20,30), Reflector3 = (50,30).

Image (b): Reflector1 = (70,30) , Reflector2 =(85,60), Reflector3 = (50,50).

Image (c): Reflector1 = (70,40) , Reflector2 = (50,60), Reflector3 = (85,45).

Image (d): Reflector1 = (40,50) , Reflector2 = (50,70), Reflector3 = (90,30).

Ultimately, tilting the source was the last condition that applied in reconstructed image simulation. The results were shown in (Fig.3.15). The coordinates of the scatterers were the same as Fig.3.12, but the coordinates of the extended source and the angle of transmission were changed in each image. The extended source's angle with respect to the array axis was $\theta = 45^\circ$ and the source's coordinates for each image were as follows:

Image (a): Sources coordinate: (30,100). Image (b): Sources coordinate: (50,150).

Image (c): Sources coordinate: (90,150). Image (d): Sources coordinate: (110,120).

- Different number of scatterers

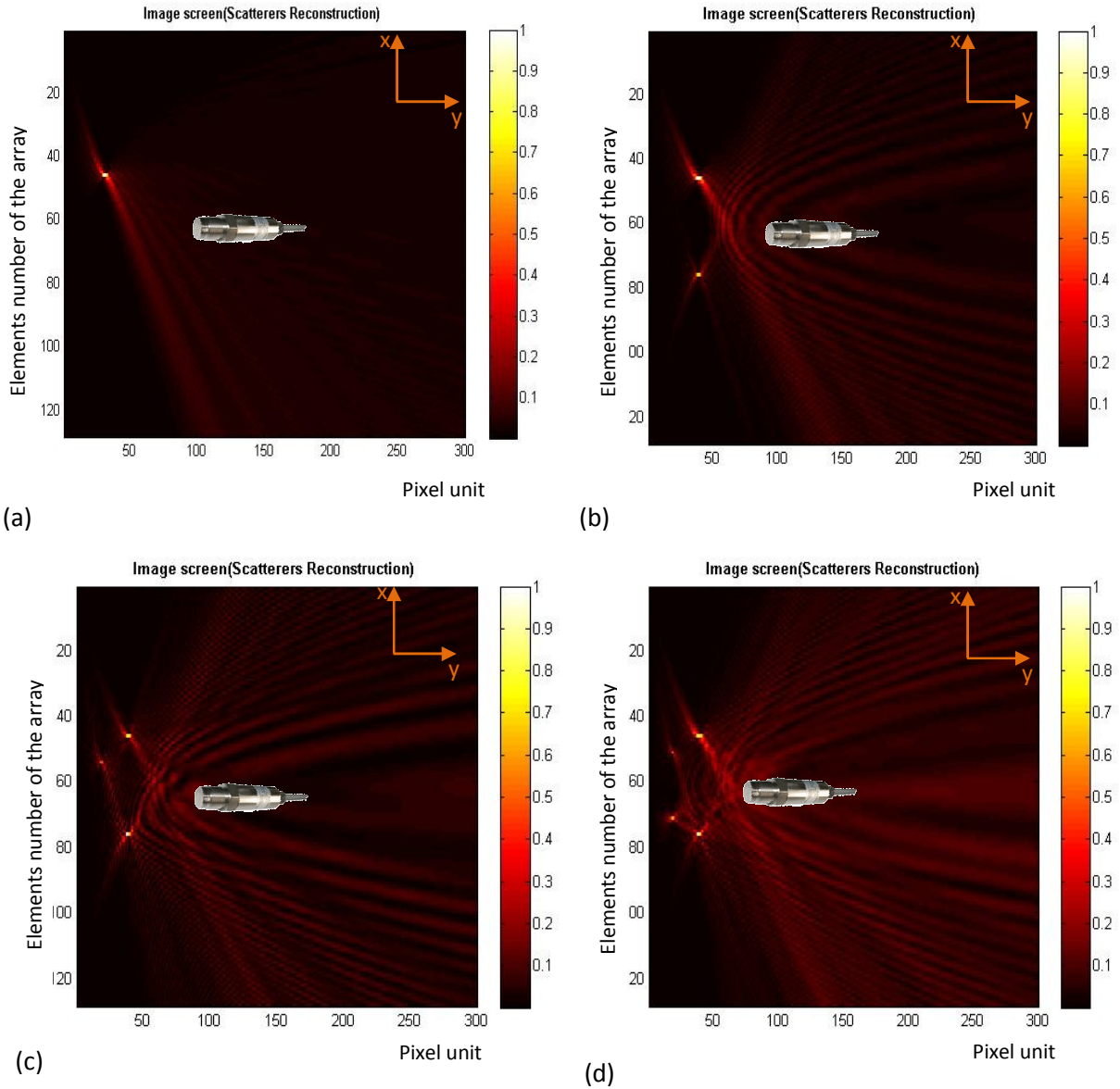


Fig.3.11. Reconstructed image of the scatterers with different position. In each image one reflector is added to the previous one. (a) Reflector1: (45,40), (b) Reflector2: (75,40), (c) Reflector3: (55,25), (d) Reflector4: (70,30).

As can be seen in this figure, in order to have accurate images, due to the interference of the reconstructed field of the scatterers and therefore magnification of interference patterns, increasing their numbers in the region of interest could be limited.

- **Changing source distance**

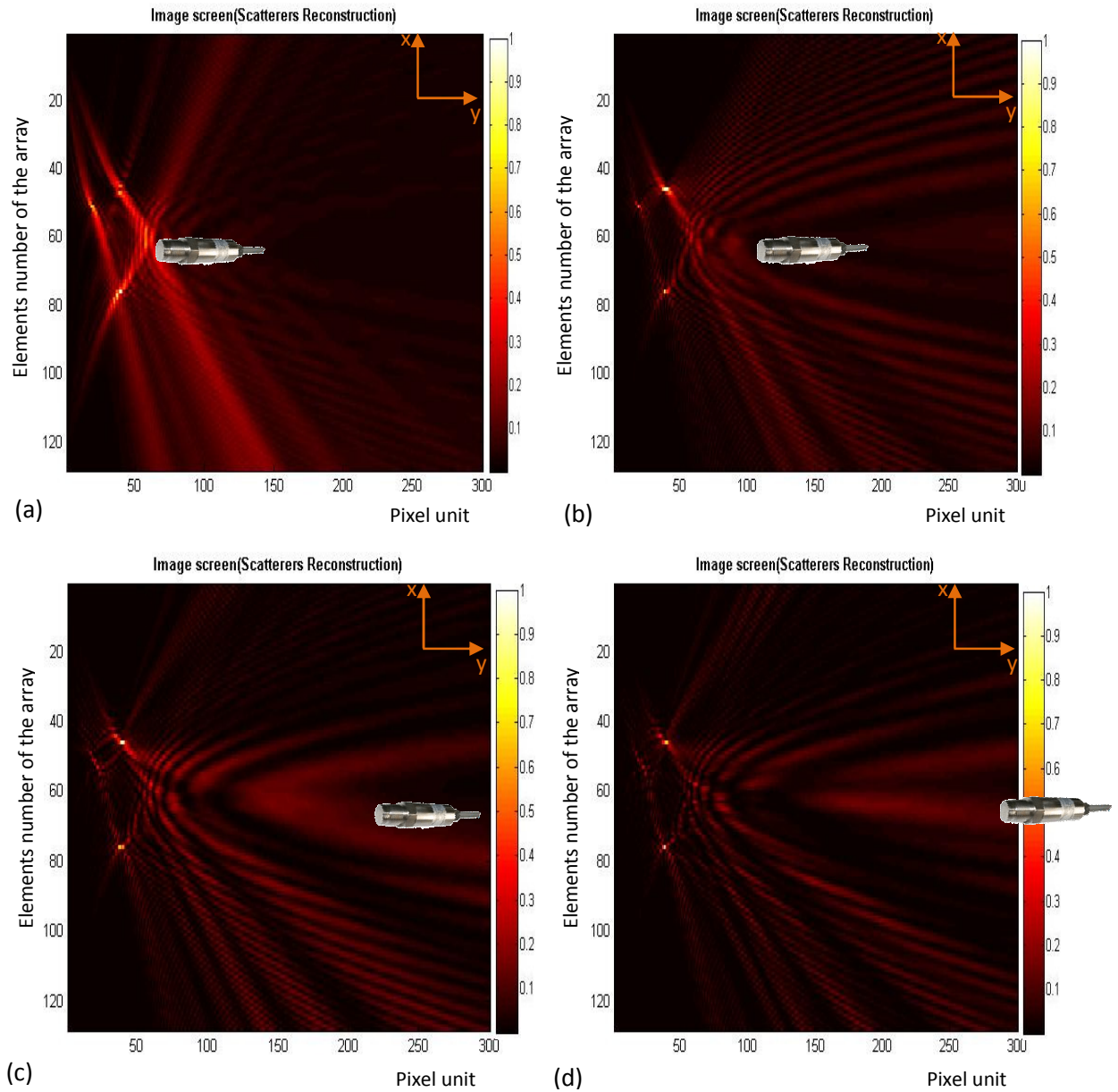


Fig.3. 12. Reconstruction images of three scatterers with regards to different distances of the source from the array. A source distance is varying as follows: (a) $D=18.50\text{mm}$, (b) $D=37.00\text{mm}$, (c) $D=74.00\text{mm}$ and (d) $D=111.00\text{mm}$.

This figure illustrates how the distance of the source from the array could affect the clarity of the reconstructed image. Close location results in strong interference pattern and far location results in low signal to noise ratio.

- Changing source's size

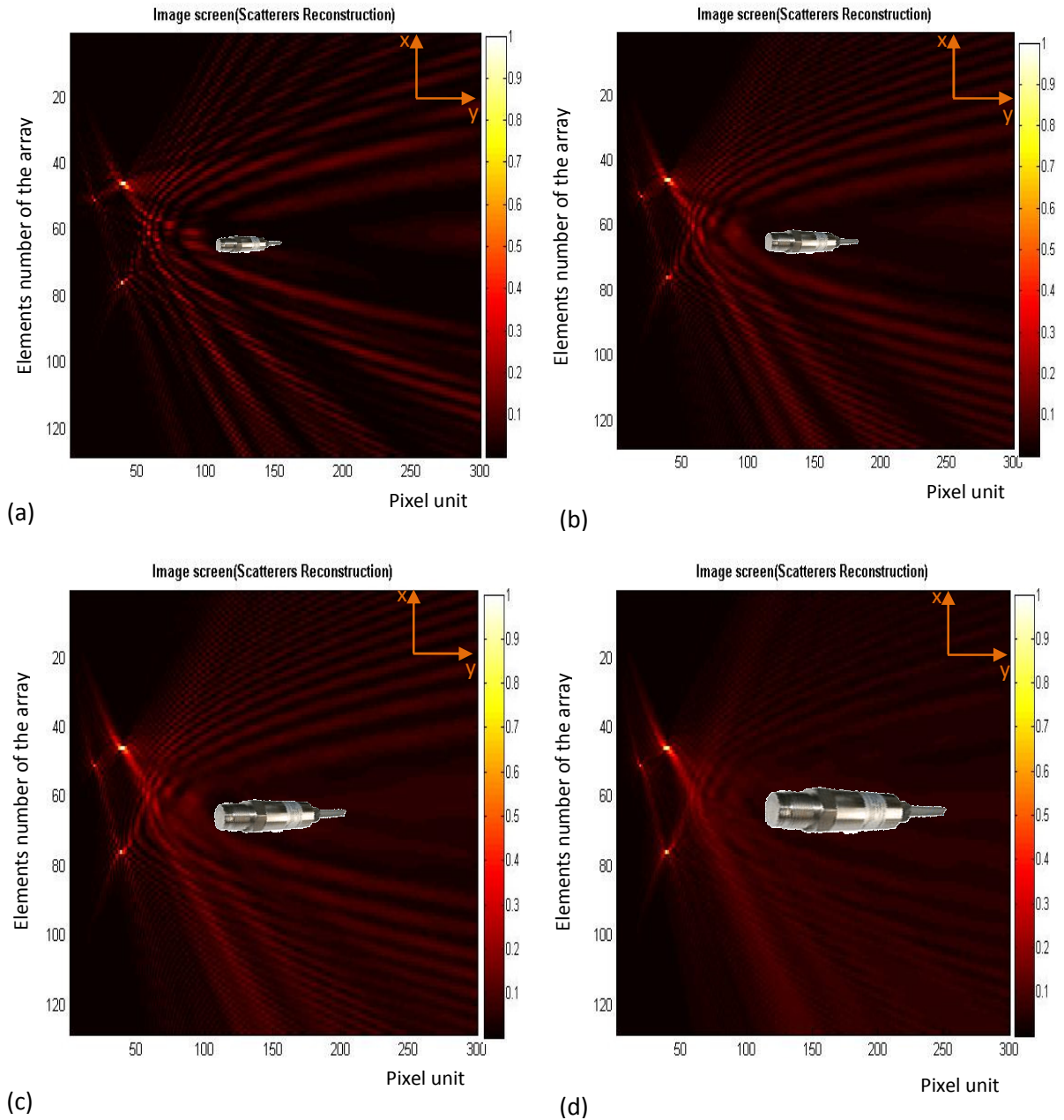


Fig.3. 13. Reconstruction images of three scatterers with the same coordinates as Fig.3.12 .These results were due to a change the size of the sources. The length of the extended source were: (a) $L=1.48mm$. (b) $L=2.96mm$. (c) $L=3.70mm$, and (d) $L=6.66mm$

These results show that by increasing the transducer diameter, a larger beam width could be achieved, and therefore a wider angle of view is possible.

- Different position of reflectors

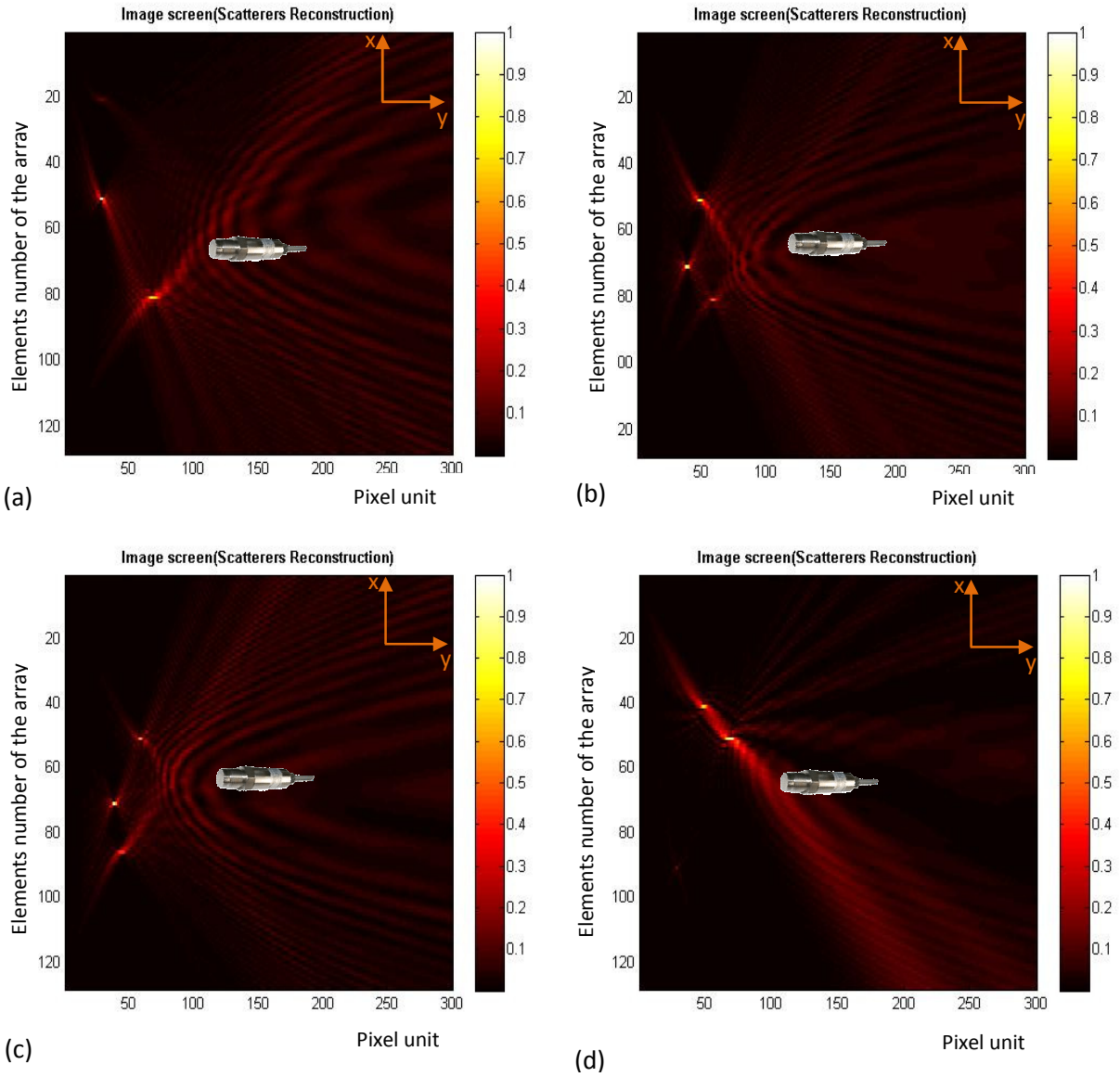


Fig.3. 14. Reconstruction images of three scatterers which were located in different positions. Their coordinates in each images were : (a) Reflector1=(80,70) ,Reflector2=(20,30), Reflector3=(50,30). (b) Reflector1=(70,30) ,Reflector2=(85,60), Reflector3=(50,50).(c) Reflector1=(70,40) ,Reflector2=(50,60), Reflector3=(85,45). (d) Reflector1=(40,50), Reflector2=(50,70) , Reflector3=(90,30).

Due to the directivity pattern of the source, the transmitted signals reach their maximum amplitude in front of the transducer. According to this figure any scatterer that was located outside of the main lobe is exposed to less ultrasound power and therefore loses

clarity in the reconstructed image.(i.e. in (a) Reflector2 and in (d) Reflector3 were not in the main lobe of transducer)

- **Tilting the source**

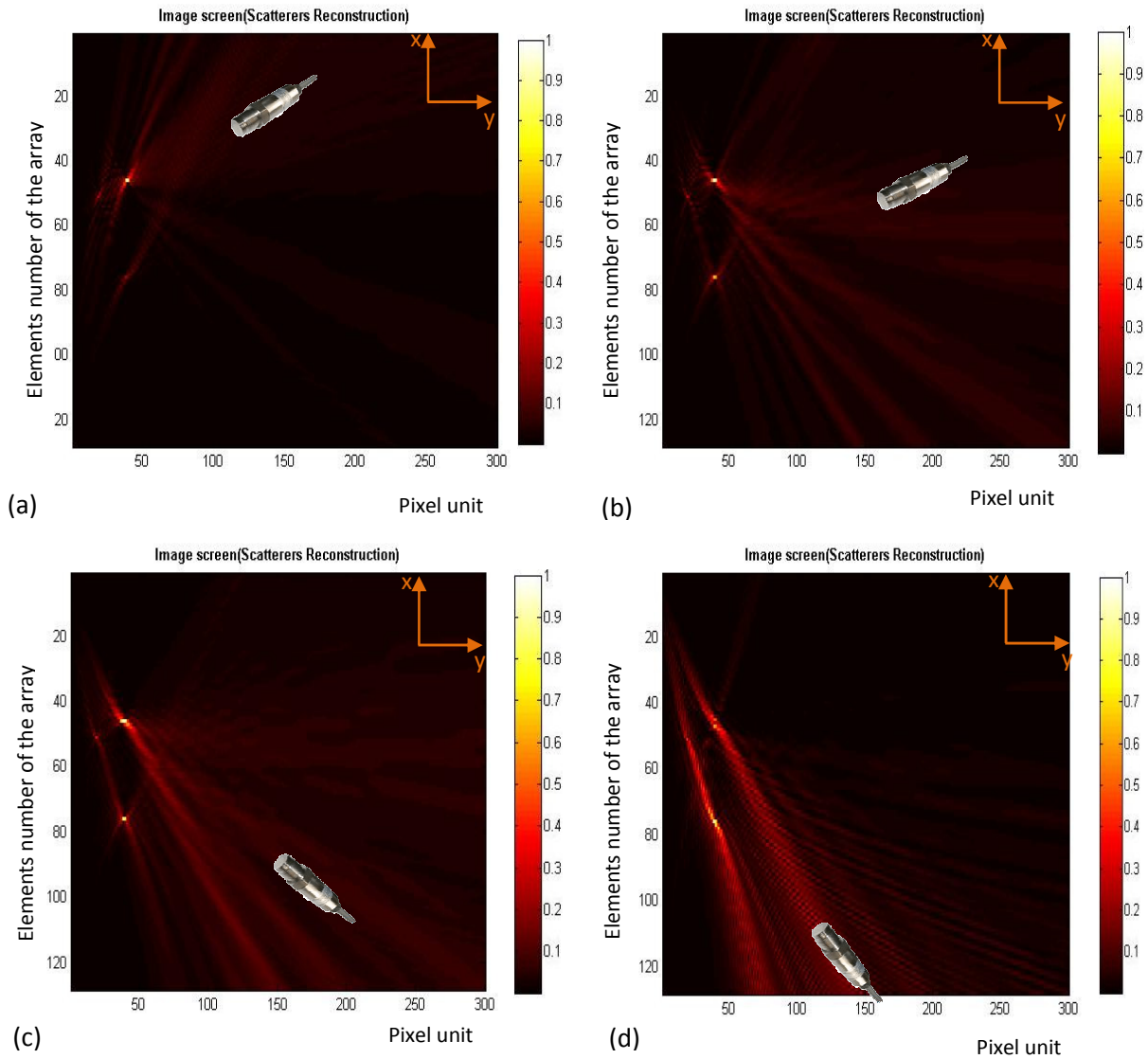


Fig.3. 15. Reconstruction images of three scatterers when source was tilted in different positions. The coordinates of the scatterers are the same as Fig.3.14. In each of these images the source coordinates are: (a) Extended Source =(30,100).(b) Extended Source =(50,150).(c) Extended Source =(90,150).(d) Extended Source =(110,120).

By tilting the source, the directivity pattern was changed and like the previous figure, the scatterers within the main lobes received more intensity.

3.3.3: Case (c) in back propagation mode

Calculating the field distribution on the array in presence of the scattering layer was illustrated in 2.3.3 (Case (c)). Reconstruction images of this field distribution were the last part of the simulation.

The phase aberrations reducing the image contrast are due to degrading of spatial resolution. Aberrators can be modeled as either being propagated through the medium or being a thin layer that disturbs the phase.

As explained in an aforementioned step, the superposition of the phase conjugated field that was saved at the array's element, was retransmitted through the medium in the presence of the scattering layer in back propagation mode. The split form of the scattering layer's phase shift, which was added to scatterer's reconstructed field (equation 3.13) can be written as

$$Real_layer_b = e^{+\alpha_{layer}*d} \cos k_2 d$$

3.14

$$Imaginay_layer_b = -e^{+\alpha_{layer}*d} \sin k_2 d$$

where d is the thickness of the layer, k_2 is the layer's wave number and α_{layer} is the attenuation factor. Adding above equations to equation 3.13 and allowing implementation of them into 3.3, 3.4 and 3.5, gave reconstructed images as before. The results are presented as follows:

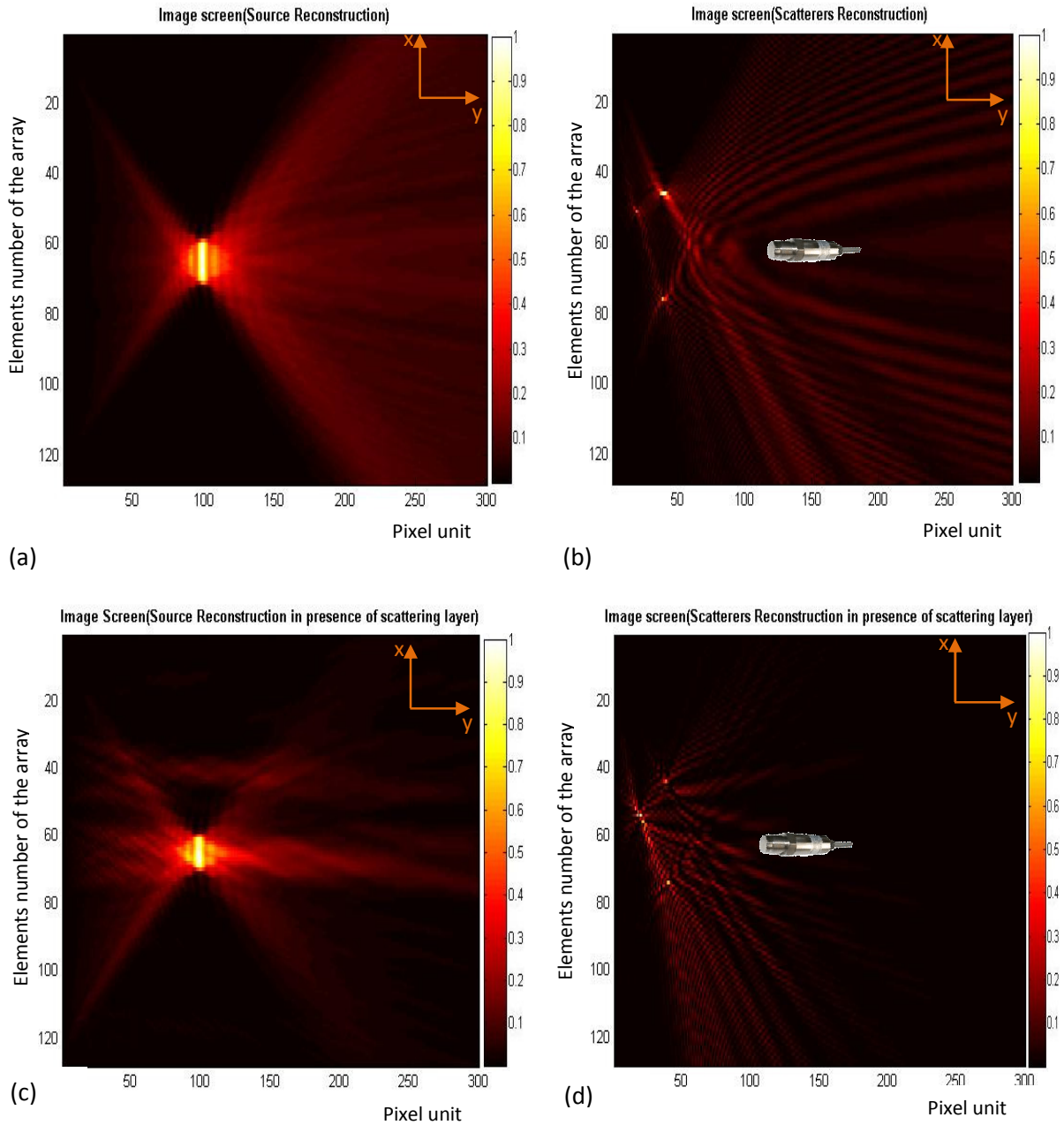


Fig.3. 16. Image reconstruction of extended source and scatterers in absence of scattering layer (a) and (b) respectively. (c) and (d) represents the results of image reconstruction of source and scatterers, respectively in presence of the scattering layer.

As the results show that by adding the scattering layer, the reconstructed images of both source and scatterers were distorted and the image intensity was decreased due to the attenuation of the layer. Also the initial positions of the scatterers were slightly shifted

toward the receiving array which was caused from higher sound speed in the scattering layer.

3.4. Conclusion

In this chapter, it was tried to simulate field distribution on the array by applying the superposition rule. Besides this, reconstructing the image of the source and the scatterers due to harmonic phase conjugation technique was conducted in different conditions.

The amount of frequency and other data used for encoding were optimized for the set up in the experiments. The implementation of the theory was found to be accurate in both field calculation mode and back propagation mode.

According to all aforementioned results, interference of the reconstructed field of the scatterers cause less accurate image, so growing scatterer number is restricted. Additionally, clarity of images also depends on the source's distance from the array of receivers.

It could be also concluded that larger transducer diameter, creating larger beam width and consequently wider angle of view is feasible.

Furthermore, based on the directivity pattern of the source, the maximum amplitude of the transmitted signal occurs in front of the transducer. Hence, scatterers that locate within this area are expose to more ultrasound intensity and have clearer reconstructed image.

A random phase shifting algorithm is proposed to determine the phase shift amounts in presence of the scattering layer. It was observed that by adding the scattering thin layer in front of the array, the reconstructed images become less accurate with less resolution, because of the attenuation of the layer and phase shifting due to its thickness.

In the next chapter, the experimental results will be discussed and the final conclusion can be achieved by comparisons between the simulation and experimental results.

Chapter 4: EXPERIMENT

To verify the simulation results reported in the previous chapter, a set of lab experiments was conducted. This was accomplished by collecting data in the form of the amplitude of the transmitted ultrasound waves incident on an array of receivers in absence of the scattering layer and in presence of this layer. Then, the collected data was fed into the simulation code to execute the image reconstruction step. In the following subsection, more information about the scattering layer phantom is presented.

4.1. Scattering layer phantom development

The phantom used in these experiments was custom developed in our group. Before discussing the experimental setup it is appropriate to explain the preparation process of this phantom, which represents the scattering layer.

The phantoms were made of unique composite material, which has acoustical properties very similar to those of the real human skull bone.

Different samples with different densities (Fig.4.1) were developed for the ultrasonic investigation. The density of each sample was measured ultrasonically at several designated points (A, B, C). Each sample has almost a constant density. The main parameters such as: speed of sound, acoustic attenuation and acoustic impedance can be estimated in relation to the density and the composition of the material.

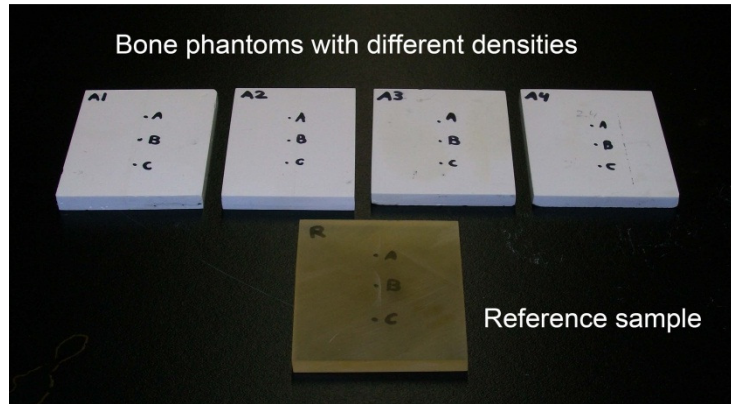


Fig.4.1. Bone phantoms with the various densities

In addition to the flat samples, a single layered phantom with one flat and one randomly curved surface (Fig.4.2) was made to serve as a scattering layer. The acoustical properties of the phantom material are summarized in Table 4.1:

Properties of material	Phantoms
Density [g/cm ³]	-
Acoustic Impedance [MRayl]	6.3
Speed of Sound - A [m/s]	3043
Speed of Sound - B [m/s]	2978
Speed of Sound - C [m/s]	3003
Speed of Sound - D [m/s]	3020
Speed of Sound – Average \pm SD [m/s]	3011 \pm 27
Total Attenuation @ 2.25 MHz – A [dB/cm]	9.4
Total Attenuation @ 2.25 MHz – B [dB/cm]	9.6
Total Attenuation @ 2.25 MHz – C [dB/cm]	10.0
Total Attenuation @ 2.25 MHz – Average \pm SD [dB/cm]	9.7 \pm 0.3

Table.4. 1. The acoustical properties of the prepared skull phantoms

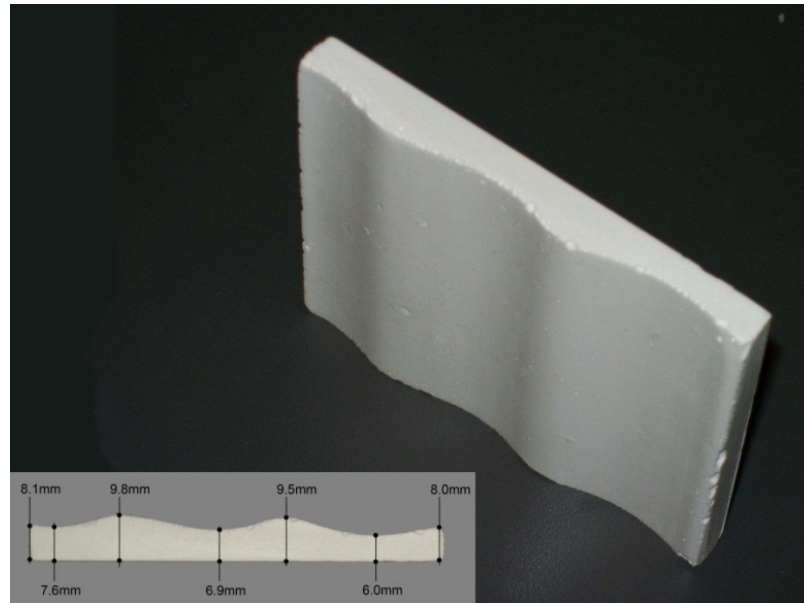


Fig.4. 2. A picture of the skull phantom and its dimensions

4.2. Experimental arrangement

The experiments for this chapter were conducted in an acrylic water tank filled with tap water. To mimic the behavior of a linear array, a small aperture receiving transducer (pinducer, Valpey Fisher) was scanned at 128 discrete points with $\frac{\lambda}{2}=0.37$ mm step size. A single 2.25 MHz, 19.05mm diameter focused transducer (Technisonic) driven at 2 MHz frequency was used to transmit the acoustic waves. Its focal spot located 38.1 mm in front of its face served as a “source” referred to in the measurements. The transmitting transducer, the phantom, and the scattering objects were held at fixed positions with thin metal holders, while the pinducer was attached to the 4-axis (IAI X-SEL) scanner.

The schematic of the experimental set-up for measuring the acoustic field distribution is shown in Fig.4.3. The PC-based data acquisition board (Instrumental Systems) was issuing the trigger pulses, which were inverted and then used to trigger the Agilent 33250A function generator. The latter was configured to emit a 2 MHz, 10V p-p, 20 cycles long tone-burst sinusoid with zero amplitude offset and zero initial phase which

was fed into the transmitting transducer. After propagating through the water containing discrete scattering objects and a subsequent scattering layer, the ultrasonic field was measured at multiple points along a straight line with a pinducer attached to the 4-axis X-SEL scanner (IAI). At each pinducer location, the received signal was pre-amplified and then fed to the data acquisition board. The digitized signals were saved in the computer memory for further processing.

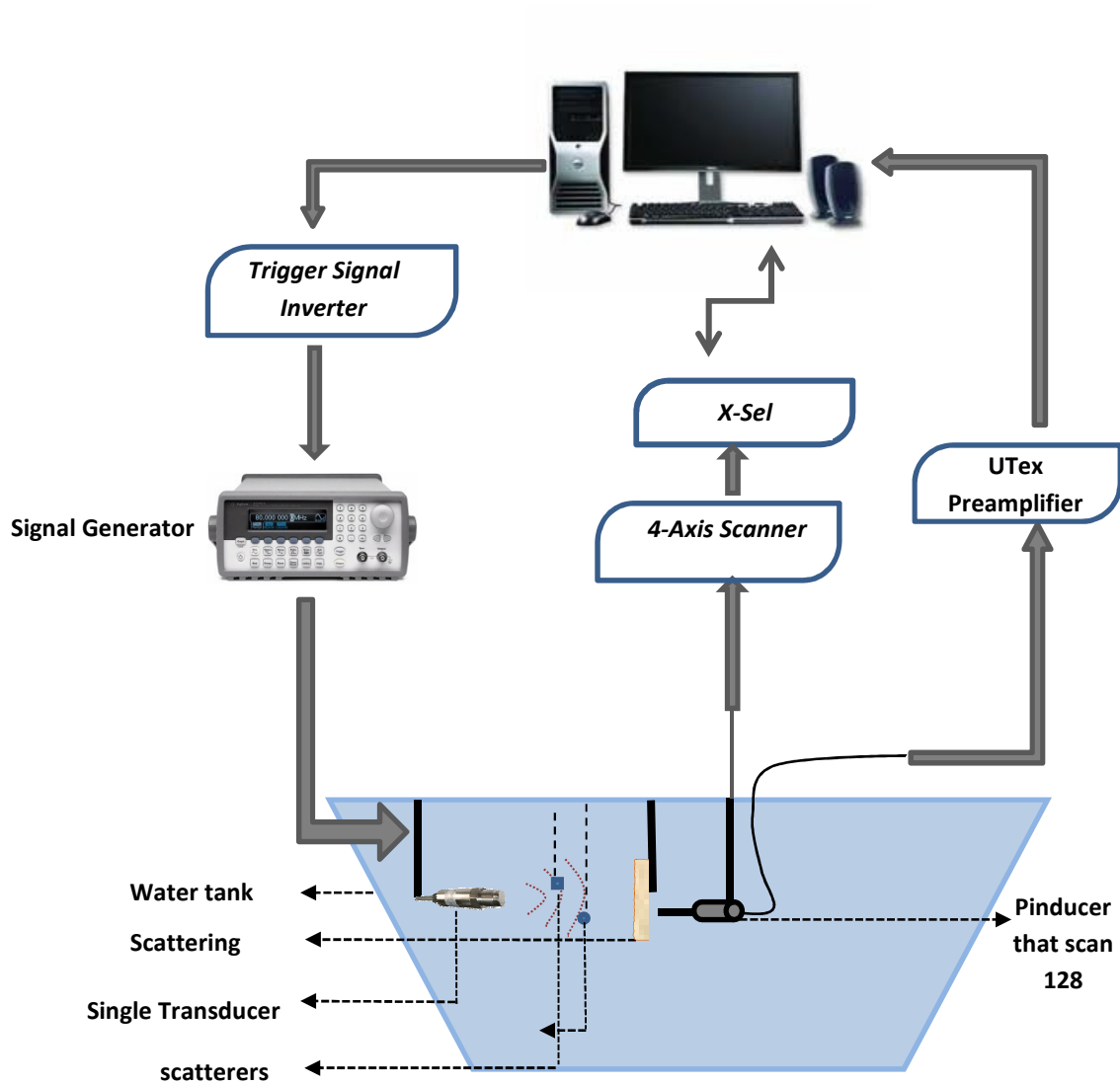


Fig.4. 3. Block-diagram of the experimental setup

The photograph of the main experimental setup is also shown in Figure 4.4.



Fig.4. 4. General experimental setup

Figure 4.5 shows the close-up view of the source-receiver arrangement as well as the positions of the scatterers and the skull phantom. For illustration purposes, the scattering objects shown in Figure 4.5 are slightly larger than those that were actually used. The size and locations of the actual scatterers used in the experiments are provided further in the text. Figure 4.6 is a picture of the water tank only.

The experimental distances from the source and the scatterers to the receiving array (pinducer scan line) are shown in Table.4.2.

	Scatterer 1	Scatterer 2	Extended source
Set up parts distances from the array	$2.90\text{cm} \pm 1\text{mm}$	$3.70\text{cm} \pm 1\text{mm}$	$13.80\text{cm} \pm 1\text{mm}$

Table.4. 2. Experimental distances from the array

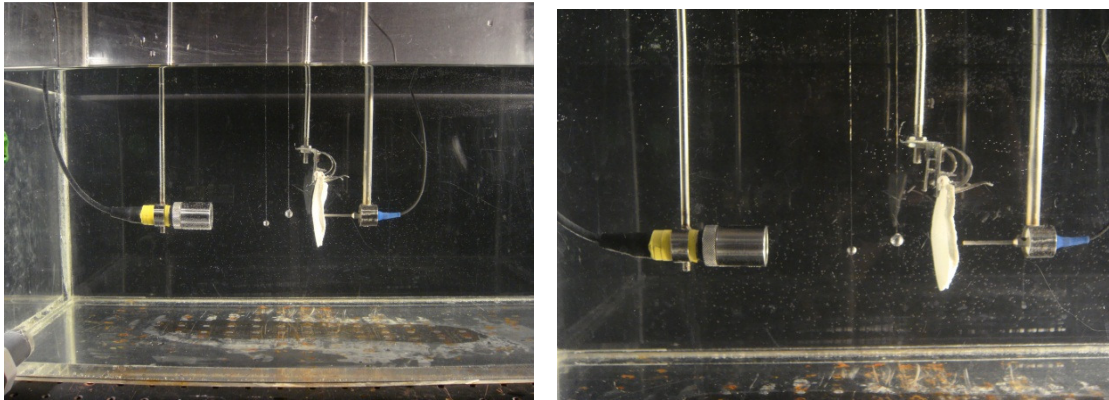


Fig.4.5. Close-up view of the source and the positions of the scatterers and the skull phantom



Fig.4.6. Picture of water tank

At the first step, the source transducer was placed 13.8cm away from the pinducer, and the field distribution was recorded at each of the 128 points along a vertical line (Figure 4.7).

At the next step, two small scatterers (0.75mm and 1.15mm in size) were introduced between the source and the scanning pinducer. These dimensions were chosen based on the assumption of “point” scatterers, i.e. those which are smaller or comparable with the 0.75 mm wavelength.

The scatterers were placed 12mm apart from each other and respectively 29.00 mm and 37.00 mm away from the pinducer scan line (array). It should be noted that in this

experiment the scatterers were always kept within the main lobe of the transducer-field diverging after the focal spot. Therefore, there was no need to consider the directivity function in calculation of field distribution on the array.

The distribution of the resulting field representing superposition of the incident and scattered fields was measured at each scanning step and saved as before. This distribution is presented in Fig.4.8.

Finally, a thin single layer of the scattering layer was added to the set up and the transmitted signal through this layer was measured by the pinducer. The measured field distribution is shown in Figure 4.9.

4.3. Results and discussion

At the forward propagation step, the experimental distributions of the incident and scattered field with and without the skull phantom layer were collected using a scanning pinducer. These data were used in the numerical back propagation mode to reconstruct the images, but as stated before, in order to reconstruct the image of the scatterers in presence and absence of the skull, the recorded incident field was subtracted from received superposition field to prevent interference of the dominant source distribution and weak scatterers distribution in back propagation mode.

As shown in Fig.4.7, the saved source field distribution that was collected during the scanning time with pinducer, was not purely symmetric as we expected, and this happened due to lack of required calibration of experimental set up. The original source was located at point 64, but the result shows the peak at point 61, which was acceptable error for our experiment.

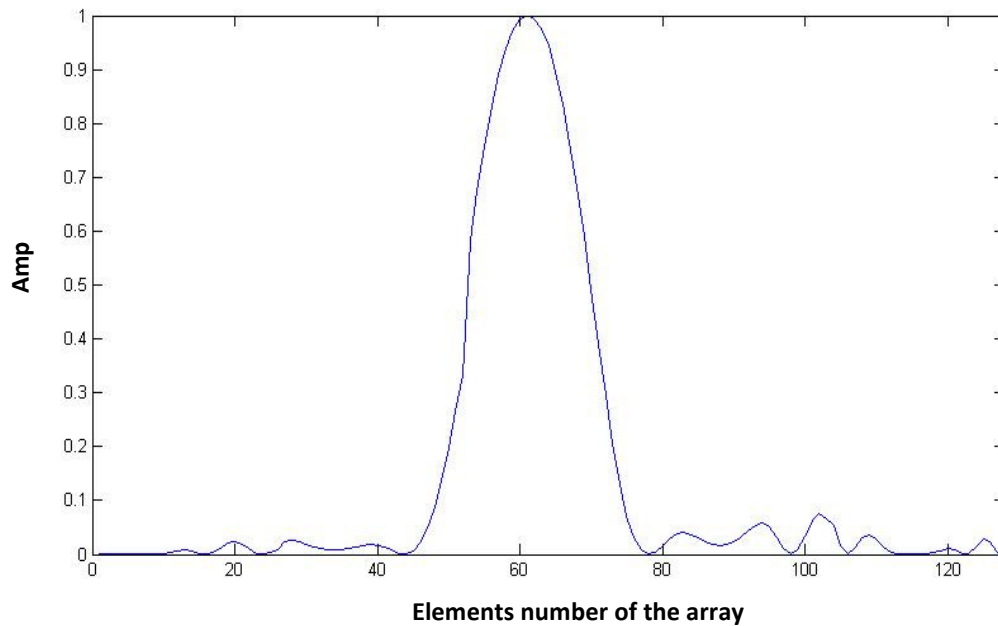


Fig.4. 7. Distribution of the incident field on the array of receivers. The plot is normalized by the maximum value of the main peak.

After collecting the incident field distribution, the scatterers were added to the set up. Again like the previous step, the single transducer was put at the designated distance and amplitude and phase distribution collected by the pinducer in each step of scanning.

The scatterers distribution results in the absence of the scattering layer is shown in Figure 4.8.

This result was normalized based on the maximum magnitude of the peak in Figure 4.7. Compared to the last figure, it is apparent that the amplitude of the main peak has declined and some distortion was generated due to the presence of the scattered field.

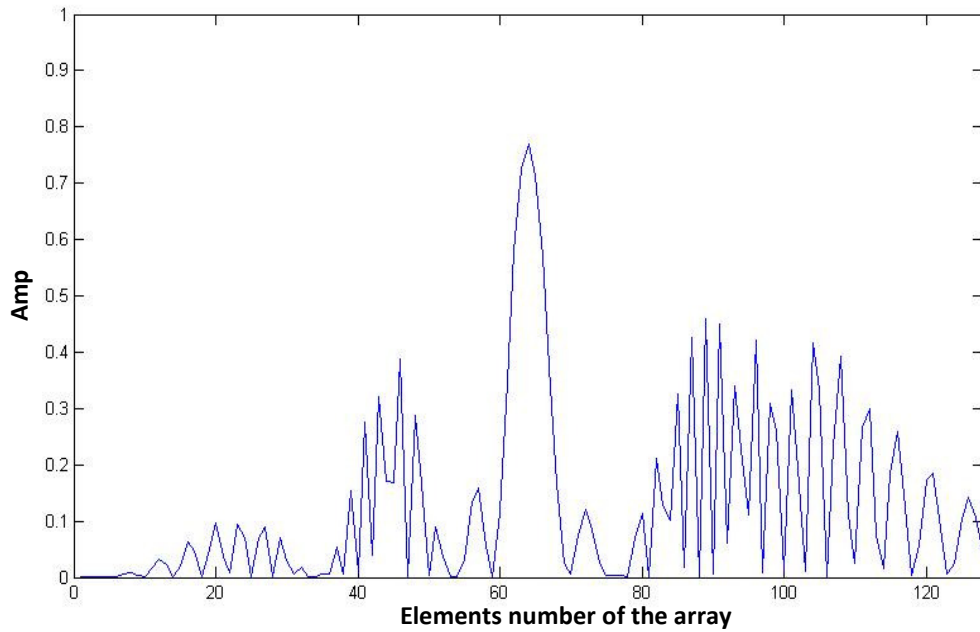


Fig.4. 8. Normalized recorded amplitude of the scatterers in absence of the scattering layer

After collecting data without scattering layer, the thin phantom of the scattering layer with a slight variation of thickness across the phantom (from 5.0 mm to 8.5 mm) was added to the other equipment parts. It should be noted that the phantom was very close to the scanning receiving pinducer. The same procedure was conducted to record the scattererd field distribution on each point with pinducer. The result of that experiment (again normalized by the maximum magnitude of the peak in Fig.4.7) is shown in Fig.4.9.

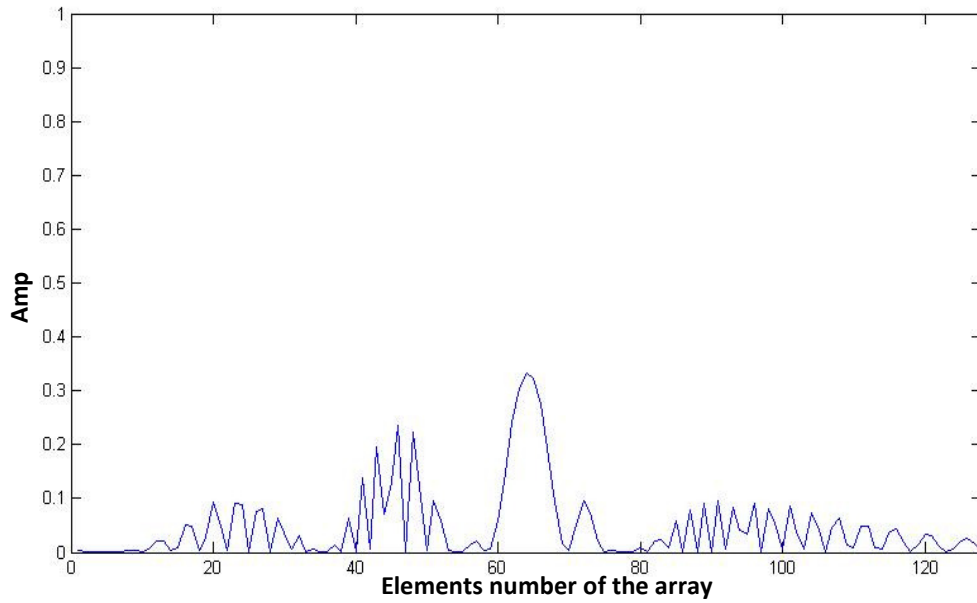


Fig.4. 9. Normalized recorded amplitude of the scatterers in Presence of the scattering layer

It can be seen that the amplitude is reduced even more due to the attenuation by the scattering layer. The thickness of the insonified portion of the layer increases slightly from left to right. So, the amplitude of the acoustic field that passes through the thickest part of the layer (right side of the figure) got attenuated more, as expected.

After collecting the field distribution data, it was fed into the simulation code to complete the image reconstruction steps for each related field distribution. It was tried to keep conditions as close as possible to those in the simulation.

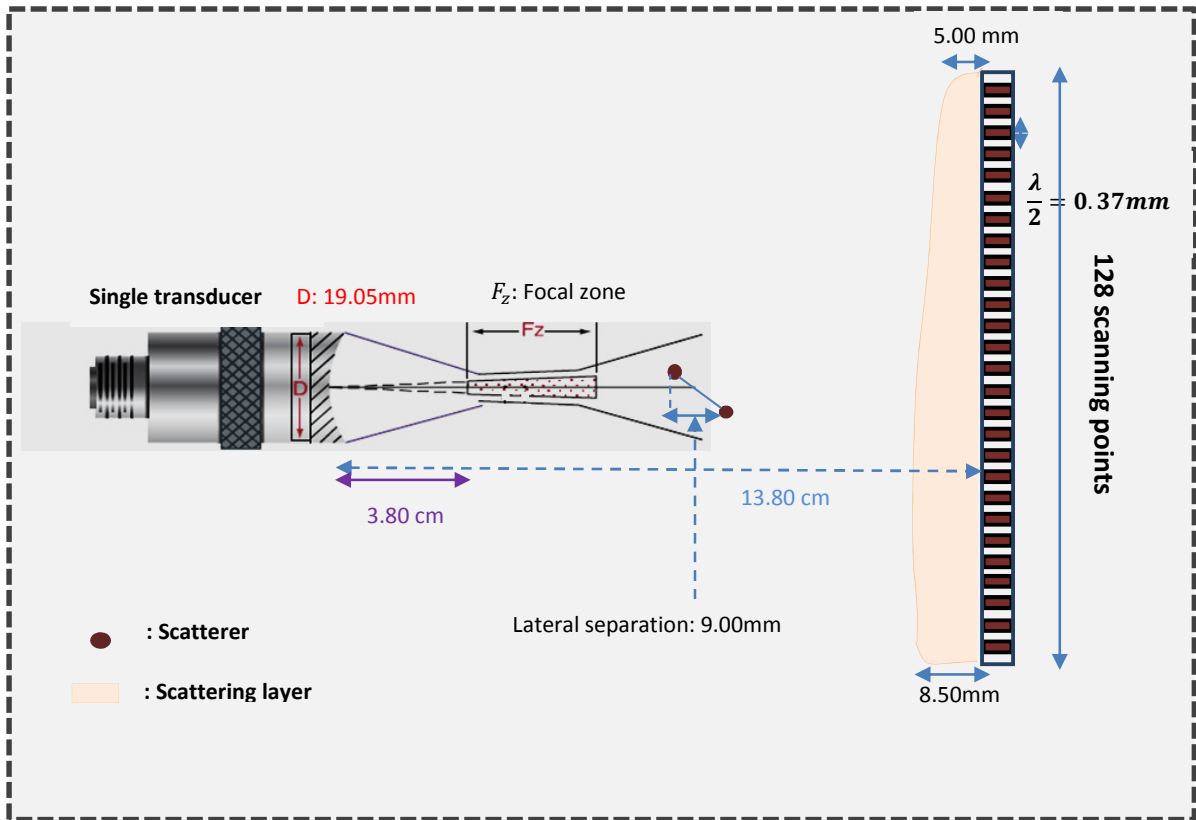


Fig.4.10. Schematic drawing of the source, scatteres, the layer, and the scanning plane with all dimensions.

Fig.4.11 - 4.13 show the reconstructed images of the source and the scatterers both in the absence and presence of the skull.

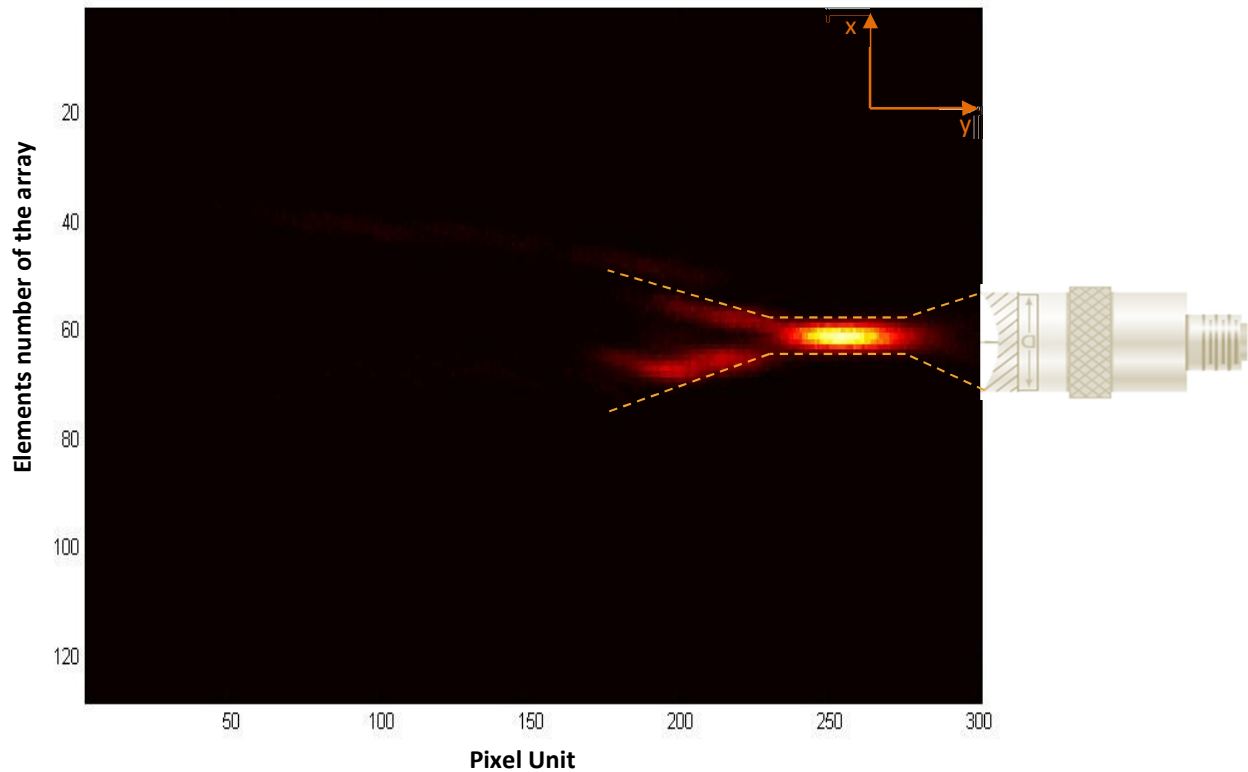


Fig.4. 11. Image reconstruction of the source in absence of the scattering layer

As stated before, the focal spot plays a role as the source instead of transducer itself, since by applying smaller source, the simulation would run faster. In addition, a source with a wider angle of view (only counting on the main lobe beam width) would give larger angle of view capability in reconstruction mode.

Fig.4.11 is presents the reconstructed image of the focal spot of the source. The original location of the source (focal spot) was 10 cm away from the scanning plane, but the maximum intensity point in the reconstructed image is slightly shifted from the true position of the focal point (9.55cm), which could be explained by the improperly calibrated set up

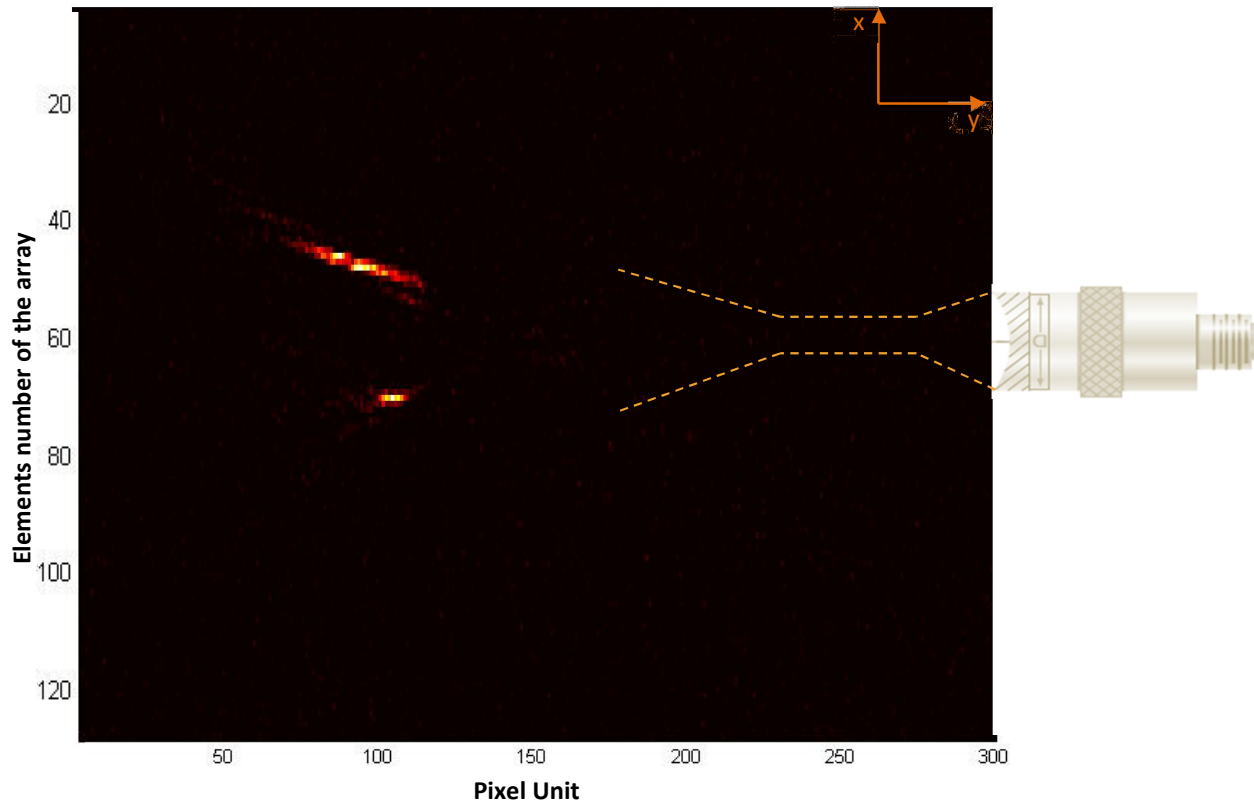


Fig.4. 12. Image reconstruction of the scatterers in absence of the scattering layer

Fig.4.12 shows the reconstructed images of two scatterers in absence of the skull. Again, the image presents the locations of the scatterers with a little shift ($\pm 1mm$) from the original place. Both scatterers had almost the same size. Due to the closer distance to receivers and being not in the middle, the reconstruction of the top scatterer seems distorted (bigger with larger shadow).

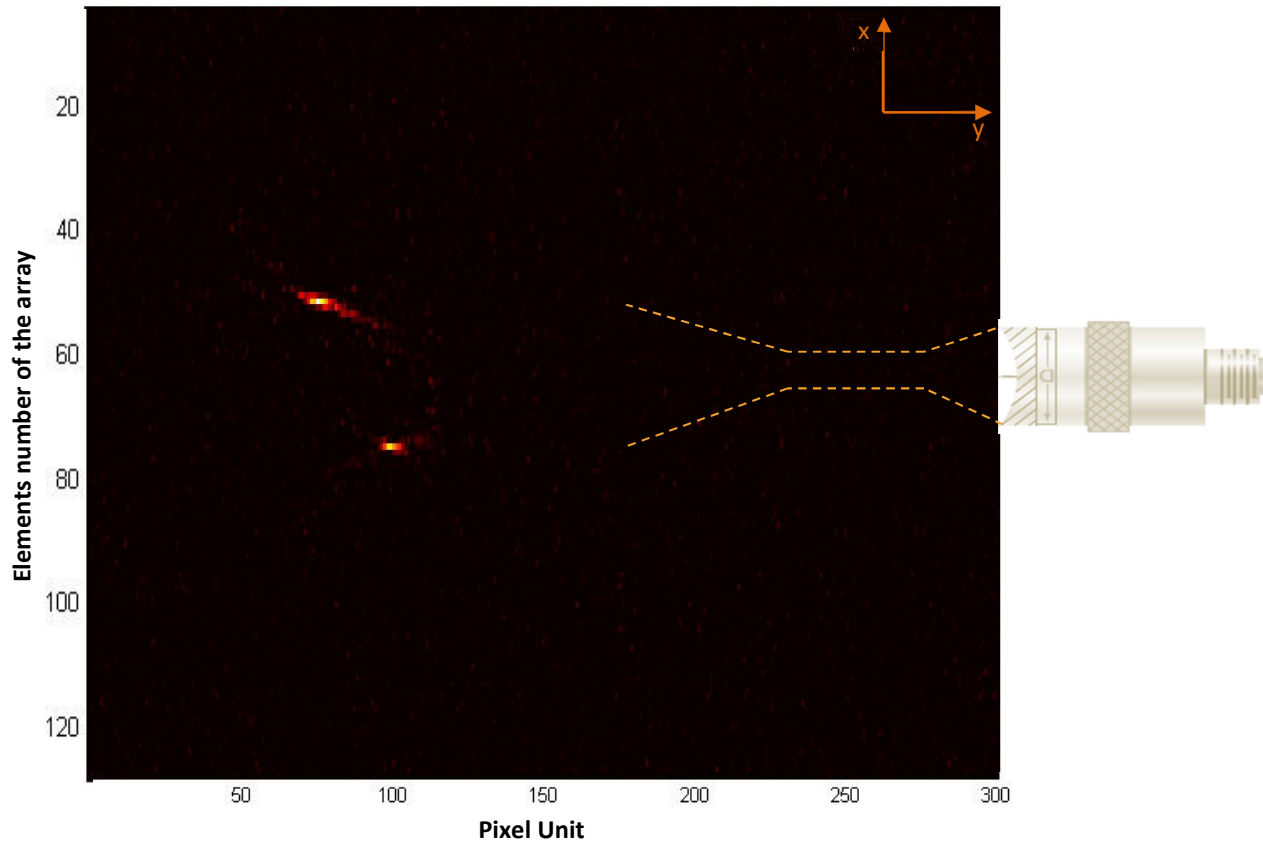


Fig.4. 13 Image reconstruction of the scatterers in presence of the scattering layer

The next result (Fig.4.13) shows the reconstructed image of the scatterer in presence of the scattering layer. Compared to the previous reconstructed image of the scatterers in absence of this layer, this image is noisier, and the reconstructed positions of both scatterers are shifted towards the receivers due to higher sound speed in the scattering layer. In addition, the image intensity is lower because of attenuation factor of the layer.

Furthermore, due to refraction at the water-scattering layer interface the scatterers appear to be shifted downward in the reconstructed image (Snell's Law).

In this chapter the phase conjugated method was successfully implemented to reconstruct images of internal objects within the brain model.

It should be noted that some concepts such as nonlinearity, shear waves and non-isotropic media were out of the scope of this study and the information will be limited to linearity and homogeneity of the brain tissue due to similar acoustical properties of the brain tissues and water. Longitudinal was the only mode that was considered and shear modes have omitted due to its high attenuation in the skull and brain.

The scattering layer in this study was assumed to be thin. The fact that with the presence of the thicker scattering layer, refraction plays an important role during collected data and it was not allow to be neglected any longer and also, the attenuation of the skull gets too strong above 2MHz, so this is our frequency limitation.

Additionally, neglecting reflection of the scatterers is acceptable due to using very small scatterers in this thesis. Besides, the variation of position distance of the scattering objects could be due to transducer alignment and calibration of the set up and therefore would be registered for the real clinical experiments. There are other sources of the systematic experimental errors created from inevitable obstacles in the surrounding area of the set up that possibly increased with acoustic field, such as thin nylon strings that held the scatterers, the base for positioning the skull and the water tank's wall.

Chapter 5: CONCLUSION AND POSSIBLE FUTURE WORK

Ultrasound diagnostic imaging is a non-invasive and relatively inexpensive examination technique that is becoming increasingly popular due to constant miniaturization of the electronics and development of new signal processing and image reconstruction algorithms.

However in terms of transcranial ultrasound imaging, the distortion of the imaging beam by the skull presents the greatest challenge in obtaining high quality images. Compared to CT and MRI, the image quality in current ultrasound transcranial imaging system is often of less diagnostic value.

In the preceding chapters, we have seen how the phase conjugated technique may be applied to ultrasound array in order to reconstruct images.

Chapter 1 presented a brief summary of the history of phase conjugated and reviewed some research up to present. Parts of this chapter explain some applications of phase conjugation approach in optics. Then, important application of ultrasound time reversal (ultrasound phase conjugated) in medical, industrial, etc. was presented. Acoustic phase conjugation (time reversal) in biomedical imaging systems, mainly transcranial imaging was considered in the rest of the chapter, but according to reviewed material, there are few articles debating the issue of image reconstruction with intact skull.

The physical and numerical basis for the algorithm and theory is presented in chapter 2.

A discussion of computational methods was presented in chapter 3. The first prediction was to calculate the amplitude and phase distribution of the scatterers on the array of receivers in different conditions for the scatterers in both the absence and presence of the scattering layer. Besides this, the collected field distribution on the array of receivers was used in back propagation mode in order to reconstruct the images of the scatterers. The reconstructed image showed high precision with one pixel error ($< 0.5\text{mm}$).

Chapter 4 presented an experimental examination of the predicted results via simulation. At this point, the field distribution was measured with a scanning pinducer in real experiments. These measured data were then inserted to the simulation to reconstruct the final images.

The experiment gave acceptable results in comparison to the predicted simulation results. Both the simulation and experiment results approximate the initial position of the scatterers in absence of the scattering layer and in presence of that.

The reconstructed image of the scatterer in absence of the layer, presented the location of the scatterers with an error ($< \pm 1mm$) compared to their original, as was illustrated in images in presence of the scattering phantom the noise is more visible, due to reflected field by the scattering layer and also the existence of shear waves in the layer which were not considered in this experiment. So only a portion of the initial field was back propagated, which leads to artifacts. It should be noted that the error can always be lowered and minimized by use of longer array and more elements with the cost of higher data processing time.

Additionally the scatterers' positions are shifted toward the phantom layer because of different sound speed in the layer, and they were attenuated due to the attenuation factor of the phantom layer.

The phase conjugated method represents a potential for improving imaging proficiency over current methods in certain conditions. For such an application, ultrasound has ability to improve the efficiency of traditional MRI or CT with respect to detection and characterization of small scatterer present in brain tissue. This method also has several advantages compared to other techniques, such as X-rays or MRI. Ultrasound procedures do not use ionizing radiation, their cost is much lower and they can be portable. The results of this study could represent a few small steps toward solving some of the challenges.

More sophisticated and realistic experiments could be studied in future. One of the future plans of the project is to substitute the phantom of the scattering layer with the ex-vivo

skull. Moreover, we used only a one dimensioned array that is not the perfect choice to collect all information. Use of planar arrays with larger cross-sections (referred to as ultrasonic mirrors) could increase the amount of useful received data and therefore more accurate results.

Appendix A

Amplitude and phase calculation in forward propagation mode and image reconstruction process in absence of the scattering layer (as an example of the whole simulation code)

```
clear all
clc
tic

freq          = 2e6;           %Hz
V1            = 1500;         %m/s
landa1       = V1/freq;
P0            = 1;
phy0         = 0;
pitch        = landa1/2;
k            = 2*pi/landa1;   %m^-1
AttenuWat    = 20.72         % (1/m) or (neper/m)
pitch2       = landa1/10;
No_elements  = 128;
I0=0;
R0=1;

Amp=zeros(No_elements,1);
Phase=zeros(No_elements,1);

ampl_re_b =zeros(No_elements,1);
ampl_im_b =zeros(No_elements,1);
P_re_Fin_b=zeros(No_elements,1);
P_im_Fin_b=zeros(No_elements,1);

ampl_mn_t=zeros(No_elements,300);
ampl_mn_scatter=zeros(No_elements,300);

% source :-----

plane=zeros(640,1500);%(128,300)

S_coordinates=[320 500];%[64 100]

p1= S_coordinates(1);
p2= S_coordinates(2);

for q=0:25
    plane(p1-q:p1+q,p2)=1;
end
```

```

[rowSource,colSource]=find(plane)

image_plane = zeros(640,1500);%(128,300)

% reflector 1: -----
reflector_CM_coordinate = [250 100]; %[50 20]

m1 = reflector_CM_coordinate(1);
m2 = reflector_CM_coordinate(2);

for i = 0:4

    image_plane(m1-i:m1+i,m2-i:m2+i) = 1;
end

%reflector 2: -----
reflector_CM_coordinate =[375 200]; %[75 40]

m1 = reflector_CM_coordinate(1);
m2 = reflector_CM_coordinate(2);

for i = 0:3
    image_plane(m1-i:m1+i,m2-i:m2+i) = 1;    %25 ta
end

%reflector 3: -----

reflector_CM_coordinate = [225 200]; %[45 40]

m1 = reflector_CM_coordinate(1);
m2 = reflector_CM_coordinate(2);

for i = 0:4
    image_plane(m1-i:m1+i,m2-i:m2+i) = 1;
end

    [row,col]=find(image_plane);
    a=length(rowSource)
    b=length(row)

for n = 1:1:No_elements
    n;
    x(n)=(n-1)*pitch;

    % x=(1:No_elements)*pitch;

```

```

ampl_re =0 ;
ampl_im =0 ;
ampl_re1 =0;
ampl_im1 =0;
P_re_Fin =0;
P_im_Fin =0;

for i = 1:length(rowSource)
    i;
    X0=rowSource(i)*pitch2;
    Y0=colSource(i)*pitch2;

    r = sqrt((x(n)- X0)^2+(0-Y0)^2);

    att = exp(-AttenuWat *r);

    pf_real = (R0*cos(k*r) - I0*sin(k*r));
    pf_imag = (I0*cos(k*r) + R0*sin(k*r));

    ampl_re = pf_real + ampl_re;
    ampl_im = pf_imag + ampl_im;

    for s = 1:length(row)

        X = row(s)*pitch2;

        Y = col(s)*pitch2;

        r = sqrt((x(n)- X0)^2+(0-Y0)^2);

        r1 = sqrt((X-X0)^2+ (Y-Y0)^2);
        r2 = sqrt((x(n)-X)^2+(Y)^2);
        R = r1+r2;

        pf_reall = (R0*cos(k*R) - I0*sin(k*R));
        pf_imag1 = (I0*cos(k*R) + R0*sin(k*R));

        ampl_re1 = pf_reall + ampl_re1;
        ampl_im1 = pf_imag1 + ampl_im1;
    end

    Re_tot =(ampl_re+ampl_re1)
    Im_tot =(ampl_im+ampl_im1);

    P_re_Fin = ( Re_tot - ampl_re)+ P_re_Fin;
    P_im_Fin = ( Im_tot - ampl_im)+ P_im_Fin;
end

r = r*1000;
Phase(n) = atan(ampl_im/ ampl_re);
Amp(n) = (att*(abs(sqrt( ampl_re^2+ampl_im^2)))*cos(Phase(n)))/r^2;

```

```

    ampl_re_b(n,1)= ampl_re;
    ampl_im_b(n,1)= ampl_im;

    R=R*1000;
    Phase_scatter(n) = atan( Im_tot/ Re_tot);

    Amp_scatter(n)
    =(att*(abs(sqrt((Re_tot)^2+(Im_tot)^2))*cos(Phase_scatter(n)))/(R))^2;

    Phase_F(n) = atan(P_im_Fin / P_re_Fin);
    Amp_F(n)=(abs(sqrt(P_re_Fin^2+P_im_Fin^2))*cos(Phase_F(n)))/(R)^2;

end

figure(1)

    subplot(4,2,1);
    plot (1:No_elements,Amp)
    title('\bf{Amplitude of the extended Source}','fontsize',10)
    xlabel('Number of elemnts on the array','fontsize',8)
    ylabel('Amp','fontsize',8)

    subplot(4,2,2);
    plot (1:No_elements,Phase)
    title('\bf{Phase of the extended Source}','fontsize',10)

    subplot(4,2,3);
    plot(1:No_elements, Amp_scatter)
    title('\bf{Amplitude of the scatterer on the array}','fontsize',10)
    xlabel('Number of elemnts on the array','fontsize',8)
    ylabel('Amp','fontsize',8)

    subplot(4,2,4);
    plot(1:No_elements,Phase_scatter)
    title('\bf{Phase of the reflectors on the array}','fontsize',10)

    subplot(4,2,5)
    plot(1:No_elements,Amp_F)
    title('\bf{final amplitude(Total(S+ref)- source) of the
    array}','fontsize',10)
    xlabel('Number of elemnts on the array','fontsize',8)
    ylabel('Amp','fontsize',8)

    subplot(4,2,6)
    plot(1:No_elements,Phase_F)
    title('\bf{Final Phase of the array}','fontsize',10)

```



```

    ampl_re1=0;
    ampl_im1=0;

    for nu=1:length(rowSource)
        X0=rowSource(nu)*pitch2;
        Y0=colSource(nu)*pitch2;
    for n=1:1:No_elements
        x=(n-1)*pitch;

        x1=x-X0;
        r=sqrt(x1^2+Y0^2);
        kr=k*r;

        pf_real=(R0*cos(kr)-I0*sin(kr));
        pf_imag=(I0*cos(kr)+R0*sin(kr));

        ampl_re_b(n,1)= pf_real;
        ampl_im_b(n,1)= pf_imag;

        for s=1:length(row)
            X= row(s)*pitch2;
            Y= col(s)*pitch2;

            r1 = sqrt((X-X0)^2+ (Y-Y0)^2);
            r2 = sqrt((x-X)^2+(Y)^2);
            R = r1+r2;
            pf_reall = (R0*cos(k*R) - I0*sin(k*R));
            pf_imagl = (I0*cos(k*R) + R0*sin(k*R));
            ampl_rel = pf_reall + ampl_rel;
            ampl_iml = pf_imagl + ampl_iml;

        end

        Re_tot=ampl_rel+pf_real;
        Im_tot=ampl_iml+pf_imagl;
        P_re_Fin_b(n,1)= Re_tot-pf_real;
        P_im_Fin_b(n,1)= Im_tot-pf_imagl;
        ampl_re1=0;
        ampl_im1=0;

    end

end

amp_back_re=0;
amp_back_im=0;
real_back_scatter=0;
imag_back_scatter=0;
amp_back=zeros(No_elements, 300);

```

```

phase_back=zeros(No_elements,300);
phase_back_scatter=zeros(No_elements,300);
amp_back_scatter=zeros(No_elements,300);

for m=1:1:300
    z=(1+m)*pitch;

for i=1:1:No_elements
    xi=(i-1)*pitch;

    for j=1:1:No_elements
        xj=(j-1)*pitch;
        R_xj=ampl_re_b(j,1);
        I_xj=ampl_im_b(j,1);

        Re_xj = P_re_Fin_b(j,1);
        Im_xj = P_im_Fin_b(j,1);

        x1=xi-xj;
        d=sqrt(x1^2+z^2);
        kd=k*d;

        amp_back_re=amp_back_re+(R_xj*cos(-kd)-I_xj*sin(-kd));
        amp_back_im=amp_back_im+(I_xj*cos(-kd)+R_xj*sin(-kd));

        real_back_scatter = real_back_scatter +(Re_xj* cos(-k*d)-
Im_xj* sin(-k*d));
        imag_back_scatter = imag_back_scatter +(Im_xj* cos(-k*d)+
Re_xj* sin(-k*d));

    end

    phase_back(i,m)=atan(amp_back_im/amp_back_re);

amp_back(i,m)=(abs(sqrt(amp_back_re^2+amp_back_im^2))*cos(phase_back(i,m)
))^2;

    phase_back_scatter(i,m)=atan((imag_back_scatter)/(real_back_scatter));
    amp_back_scatter(i,m) =((abs(sqrt((real_back_scatter)^2 +
(imag_back_scatter)^2))* cos(phase_back_scatter(i,m))))^2;

    amp_back_re=0;
    amp_back_im=0;

    real_back_scatter=0;
    imag_back_scatter=0;

end
end

```

```

    ampl_mn_t=ampl_mn_t+amp_back;
    ampl_mn_scatter=ampl_mn_scatter+ amp_back_scatter;
end

k=max(ampl_mn_t, [],1);
l=max(k);
ampl_mn_t=ampl_mn_t/l;

q=max(ampl_mn_scatter, [],1);
w=max(q);
ampl_mn_scatter= ampl_mn_scatter/w;

figure(4)
% surf(ampl_mn_t);
imagesc(ampl_mn_t);
colormap hot
title('\bf{Image screen(Source Reconstruction) }','fontsize',10)
colorbar;
% xlabel('Number of elemnts on the array','fontsize',8)
% ylabel('Amp','fontsize',8)

figure(5)
% surf( ampl_mn_scatter);
imagesc( ampl_mn_scatter);
colormap hot
title('\bf{Image screen(Scatterers Reconstruction) }','fontsize',10)
% colorbar;
% xlabel('Number of elemnts on the array','fontsize',8)
% ylabel('Amp','fontsize',8)

toc

```

References

1. Brysev, L.M. Krutyansky, V.L. Preobrazhensky. “*Wave phase conjugation of ultrasonic beams*”. P. Brysev, L. M. Krutyansky, V. L. Preobrazhensky, Phys.-Usp. 1998, v.41, (8) p.p.793-805.
2. Blomgren, Peter, George Papanicolaou, and Hongkai Zhao. “*Super-resolution in time-reversal acoustics*. “*Journal of the Acoustical Society of America* 111.1 (2002): 230.
3. Rockwell, Da. “*A review of phase-conjugate solid-state lasers.*” *IEEE Journal of Quantum Electronics* 24.6 (1988) : 1124–1140.
4. Derode, Arnaud, Arnaud Tourin, and Mathias Fink. “*Time reversal versus phase conjugation in a multiple scattering environment.*”*Ultrasonics* 40.1-8 (2002) : 275-280.
5. Fink M, Cassereau. D, Derode. A, Prada.C, Roux. Ph, Tanter. M,Thomas. L-J, Wu.F, “*Time-Reversed Acoustics.*” *Scientific American* 281.5 (1999) : 91-97
6. Chew, W C, and T M Habashy. “*Phase-Conjugate Mirror and Time-Reversal.* “ *Journal of the Optical Society of America a Optics Image Science and Vision* 2.6 (1985) : 808-809. Print.
7. Yariv, A. “*Phase conjugate optics and real-time holography.*” *Quantum Electronics IEEE Journal of* 14.9 (1978) : 650-660.
8. R.A Fisher, “*Optical phase conjugation*”, academic Press, 1985
9. Zel’dovich, B Y et al. “*Connection between the wave fronts of the reflected and exciting light in stimulated Mandel’shtam-Brillouin scattering,*“ *Sov. Phys. JETP* 15, 109113 (1972).”*SovPhys JETP* 15 (1972) : n. pag. Print.
10. Robert W. Boyd, “*Nonlinear Optics*”, ACADEMIC PRESS 2008, chapter 9
11. N.Hodgson and H.Weber, “*Optical Resonators*”, Chapter.15, Springer1997.

12. Yariv, A. "*Optical Electronics in Modern Communications*". Oxford University Press, 1997.
13. A.E. Siegman et al, "*Optical resonators using phase-conjugation mirrors,*" Chapter 13, *Optical Phase Conjugation, P.A.Fisher, Academic Press,1983.*
14. Shen, Y R. "*The principles of nonlinear optics*". Wiley-Interscience, 1984.
15. David M. Pepper, "*Applications of Optical Phase Conjugation,*" Scientific American, 254(1), Jan. 1986,— "*Nonlinear Optical Phase Conjugation,*" Optical Engineering, 21(2), March/April1982.
16. He, G. "*Optical phase conjugation: principles, techniques, and applications.*" Progress in Quantum Electronics 26.3 (2002) : 131-191
17. E.G.sauer, "*Nonlinear Optics*", John Wiley & sons,Inc,1996.
18. M Ohno, K Yamamoto, A Kokubo, K Sakai, and K Takagi J. Acoust. "*Acoustic phase conjugation by nonlinear piezoelectricity. I. Principle and basic experiments*". Soc. Am., Vol. 106, No. 3 Pt. 1, pp. 1330-1338, Sep-1999
19. K Yamamoto, M Ohno, A Kokubo, K Sakai, and K TakagiJ. Acoust. "*Acoustic phase conjugation by nonlinear piezoelectricity. II. Visualization and application to imaging systems*". Soc. Am., Vol. 106, No. 3 Pt. 1, pp. 1339-1345, Sep-1999
20. O. Ikeda. "*An image reconstruction algorithm using phase conjugation for diffraction-limited imaging in an inhomogeneous medium,*" J. Acoust.Soc. Am. 85, 1602-1606 (1989).
21. Pyl'nov Yu., Pernod P., Preobrazhensky V." "*Acoustic imaging by second harmonic of phase-conjugate wave in medium*".//Appl. Phys. Letts. 2001.-V.78- №4.- P .553-555.
22. Jackson, Darrell R. "*Phase conjugation in underwater acoustics.*" *Journal of the Acoustical Society of America* 89.1 (1991) : 171.

23. Kuperman, W A et al. “*Phase conjugation in the ocean: Experimental demonstration of an acoustic time-reversal mirror.*” *Journal of the Acoustical Society of America* 103.1 (1998) : 25.
24. Brysev, A, R Klopotov, and L Krutyansky. “*A quality of parametric wave phase conjugation of ultrasound.*” *Ultrasonics* 40.1-8 (2002) : 329-332. Print.
25. Hodgkiss, W S et al. “*A long-range and variable focus phase-conjugation experiment in shallow water.*” *Journal of the Acoustical Society of America* 105.3 (1999) : 1597.
26. Fink, M. “*Time reversal of ultrasonic fields. I. Basic principles.*”*IEEE Transactions on Ultrasonics, Ferroelectrics and Frequency Control* 39.5 (1992) : 555-566.
27. Derode, Arnaud, Arnaud Tourin, and Mathias Fink. “*Time reversal versus phase conjugation in a multiple scattering environment.*”*Ultrasonics* 40.1-8 (2002) : 275-280.
28. De Rosny, J, and M Fink. “*Overcoming the diffraction limit in wave physics using a time-reversal mirror and a novel acoustic sink.*” *Physical Review Letters* 89.12 (2002) : 124301.
29. Fink, M, Prada, C, Wu, F, and Cassereau, D. “*Self-focusing in inhomogeneous media with time reversal acoustic mirrors.*” *IEEE Ultrasonics Symposium 1989 Proceedings* (1989) : 681–686.
30. Prada, C, Wu, F, and Fink, M “*The iterative time reversal mirror: A solution to self-focusing in the pulse echo mode.*” *Journal of the Acoustical Society of America* 90.2 (1991) : 1119.
31. Wu, F, J L Thomas, and M Fink. “*Time reversal of ultrasonic fields. II. Experimental results.*”*IEEE Transactions on Ultrasonics, Ferroelectrics and Frequency Control* 39.5 (1992) : 567-578.
32. Fink, Mathias, Gabriel Montaldo, and Mickael Tanter. “*Time-reversal acoustics in biomedical engineering.*” *Annual Review of Biomedical Engineering* 5.c (2003) : 465-497.
33. Gruber, Fred K, Edwin A Marengo, and Anthony J Devaney. “*Time-reversal imaging with multiple signal classification considering multiple scattering between the targets.*” *Journal of the Acoustical Society of America* 115.6 (2004) : 3042.

34. Kerbrat, E et al. “*Imaging in the presence of grain noise using the decomposition of the time reversal operator.*” *Journal of the Acoustical Society of America* 113.3 (2003) : 1230-1240.
35. Griffa, M et al. “*Investigation of the robustness of time reversal acoustics in solid media through the reconstruction of temporally symmetric sources.*” *Journal of Physics D: Applied Physics* 41.8 (2008) : 085,415.
36. Cassereau, D, and M Fink. “*Time-reversal of ultrasonic fields.III. Theory of the closed time-reversal cavity.*”*IEEE Transactions on Ultrasonics, Ferroelectrics and Frequency Control* 39.5 (1992) : 579-92.
37. Habib Ammari,” *Mathematical modeling in Biomedical Imaging I: Electrical and Ultrasound Topographies, Anomaly Detection, And Brain Imaging*” Springer 2009, Chapter 2
38. Robert, Jean-Luc et al. “*Time reversal operator decomposition with focused transmission and robustness to speckle noise: Application to microcalcification detection.*” *Journal of the Acoustical Society of America* 119.6 (2006) : 3848.
39. Tanter, M, J L Thomas, and M Fink. “*Focusing and steering through absorbing and aberrating layers: application to ultrasonic propagation through the skull.*” *Journal of the Acoustical Society of America* 103.5 Pt 1 (1998) : 2403-2410. Print.
40. Fink, Mathias. “*Time-Reversed Acoustics.*” *Scientific American* 281.5 (1999): 91-97.
41. Lewis, George K et al. “*Time-reversal techniques in ultrasound-assisted convection-enhanced drug delivery to the brain: Technology development and in vivo evaluation.*” *Journal of the Acoustical Society of America* 128.4 (2010) : 2335. Print.
42. White, Phillip Jason. “*Transcranial focused ultrasound surgery.*” *Topics in magnetic resonance imaging TMRI* 17.3 (2006) : 165-172
43. Sun, J, and K Hynynen. “*The potential of transskull ultrasound therapy and surgery using the maximum available skull surface area.*” *Journal of the Acoustical Society of America* 105.4 (1999) : 2519-2527.

44. White, P J, G T Clement, and K Hynynen. “*Longitudinal and shear mode ultrasound propagation in human skull bone.*” *Ultrasound in medicine biology* 32.7 (2006) : 1085-96.
45. Clement, Gt, and K Hynynen. “*Field characterization of therapeutic ultrasound phased arrays through forward and backward planar projection.*” *Journal of the Acoustical Society of America* 108.1 (2000)
46. Sun, J, and K Hynynen. “*Focusing of therapeutic ultrasound through a human skull: a numerical study.*” *Journal of the Acoustical Society of America* 104.3 Pt 1 (1998) : 1705-1715
47. White, DN et al. “*Effect of the skull in degrading the display of echoencephalographic B and C scans.*” *Journal of the Acoustical Society of America* 44.5 (1968) : 1339-1345. Print.
48. Clement, Greg T. “*Spectral image reconstruction for transcranial ultrasound measurement.*” *Physics in Medicine and Biology* 50.23 (2005) : 5557-72.
49. Vignon, F et al. “*Adaptive focusing for transcranial ultrasound imaging using dual arrays.*” *Journal of the Acoustical Society of America* 120.5 Pt 1 (2006) : 2737-2745.
50. O'Donnell, M, and S W Flax. “*Phase-aberration correction using signals from point reflectors and diffuse scatterers: measurements.*” *IEEE Transactions on Ultrasonics, Ferroelectrics and Frequency Control* 35.6 (1988) : 768-774
51. Zhao, D, and G E Trahey. “*Comparisons of image quality factors for phase aberration correction with diffuse and point targets: theory and experiments.*” *IEEE Transactions on Ultrasonics, Ferroelectrics and Frequency Control* 38.2 (1991) : 125-132
52. White, D N, G R Curry, and R J Stevenson. “*The acoustic characteristics of the skull.*” *Ultrasound in medicine biology* 4.3 (1978) : 225-252. Print.
53. Zheng, Yongping, R G Maev, and I Y Solodov. “*Nonlinear acoustic applications for material characterization: A review.*” *Canadian Journal of Physics* 77.12 (1999) : 927-967.

54. J.David,N. Cheek, "*Fundamentals and applications of Ultrasonic Waves*,"(CRC Press LLC, 2002),PP.1-8
55. Richard S. C. Cobbold, "*Foundations of Biomedical Ultrasound*," (Oxford university Press,2007), PP. 62-66
56. Eugene Hecht, "*Optics* " Fourth edition., Addison-Wesley, Reading, 2002. PP.443-514
57. A. Luis, "*Complementary Huygens principle for geometrical and nongeometrical optics*"
Eur. J. Phys. 28, 231-240 (2007).
58. F. Alton Everest & Ken C. Pohlmann, "*Master Handbook of Acoustics*" Fifth edition, (MacGrawHill companies, 2009), chapter 7
59. Richard S. C. Cobbold, "*Foundations of Biomedical Ultrasound*," (Oxford university Press,2007), PP. 96-108
60. Michel Bruneau & Catherine Potel," *material and Acoustics Handbook*", (ISTE Ltd and John Wiley & Sons,Inc, 2009), chapter 2, PP:29-31
61. Richard S. C. Cobbold, "*Foundations of Biomedical Ultrasound*," (Oxford university Press, 2007), PP. 29-34 & 69-72

Vita Auctoris

Raheleh Mirzania was born in 1981 in Shiraz, Iran. She obtained Bachelor of Science in physics at the Shahid Bahonar University of Kerman in 2005. One year after graduation, she immigrated to Canada, and is currently a candidate for the degree of Master of Science in Physics at the University of Windsor.